

Characterization and Prediction of Water Droplet Size in Oil-Water Flow

A thesis presented to
the faculty of
the Russ College of Engineering and Technology of Ohio University

In partial fulfillment
of the requirements for the degree
Master of Science

Juncheng Yao

August 2016

© 2016 Juncheng Yao. All Rights Reserved.

This thesis titled
Characterization and Prediction of Water Droplet Size in Oil-Water Flow

by

JUNCHENG YAO

has been approved for
the Department of Mechanical Engineering
and the Russ College of Engineering and Technology by

Marc Singer

Assistant Professor of Chemical and Biomolecular Engineering

Dennis Irwin

Dean, Russ College of Engineering and Technology

Abstract

YAO, JUNCHENG, M.S., August 2016, Mechanical Engineering

Characterization and Prediction of Water Droplet Size in Oil-Water Flow

Director of Thesis: Marc Singer

Corrosion is a significant issue affecting oil-water transportation pipelines and causing failures. It occurs when the water present in the produced fluids (a mixture of gas and liquid hydrocarbons) comes into contact and reacts with the pipe surface. Preventing direct contact between water and steel surface is key in mitigating corrosion. This can be achieved by ensuring that water is dispersed as droplets in the oil flow. This situation, called dispersed water-in-oil flow, is attained when the specific operating conditions are met. Being able to predict when dispersed water-in-oil flow occurs holds consequently a significant importance in any asset integrity plan. Liquid flow rates and water cut play obviously a crucial role but, more specifically, the prediction of water droplet size and distribution is essential in determining when dispersed water-in-oil flow is stable. This present study focuses on experimental measurements of maximum droplet size and droplet size distribution in water-in-oil dispersion for a wide range of flow conditions. The experimental data are compared with the current prediction models and the effects of turbulent level and water cut on maximum droplet size and droplet size distribution is also studied. Gaps in the current understanding are identified and improvements of the predictions models are then proposed.

Dedication

To my family and friends.

Acknowledgments

The author wants to acknowledge Institute of Corrosion and Multiphase Technology for their and Ohio University for their support. The valuable help from my advisor Dr. Marc Singer, my project leader Dr. Luciano Paolinelli, laboratory engineers and technicians at the Institute of Corrosion and Multiphase Technology is also greatly appreciated.

Table of Contents

	Page
Abstract.....	3
Dedication.....	4
Acknowledgments.....	5
List of Tables	10
List of Figures.....	11
Chapter 1: Introduction.....	21
1.1 Flow patterns.....	22
1.2 Importance of studying droplet size.....	24
1.2.1 Maximum droplet size	24
1.2.2 Droplet size distribution.....	25
Chapter 2 Literature Review.....	27
2.1 Water wetting model for oil-water flow	27
2.1.1 Comparing maximum droplet size and critical droplet size	28
2.1.2 Comparing local water concentration with inversion point.....	29
2.2 Modeling droplet sizes.....	34
2.2.1 Maximum droplet size prediction	37
2.2.1.1 Maximum droplet size model for dilute dispersion (Hinze Model)	37
2.2.1.2 Maximum droplet size model for dense dispersion (Brauner Model)	40
2.2.2 Droplet size distribution prediction	43
2.2.2.1 Rosin-Rammler equation	44

	7
2.2.2.2 Log-normal function	45
2.3 Droplet breakup rate and coalescence rate	46
2.3.1 Droplet breakup rate prediction	46
2.3.2 Droplet coalescence rate prediction	48
2.3.2.1 Collision rate	49
2.3.2.2 Coalescence efficiency	50
2.4 Turbulent dissipation calculation	53
2.4.1 Standard pipe flow	54
2.4.2 Pipe flow with mixing valve	54
2.4.3 Couette flow	55
2.5 Review of experimental data found in the literature	57
Chapter 3 Motivation and Project Objectives	59
3.1 Research gaps	59
3.2 Objectives	59
3.3 Hypotheses	60
3.4 Scope of work	60
Chapter 4 Experiment Setup	64
4.1 Fluids selected for the study	64
4.2 Large scale flow loop	64
4.2.1 Operating procedure	66
4.2.2 Oil and water pumps characteristics	68
4.2.3 Flow loop test sections	68

	8
4.2.3.1 Test section for standard pipe flow conditions	69
4.2.3.2 Test section for pipe flow with mixing valve conditions.....	70
4.4 Doughnut cell.....	73
4.5 Analytical methods	75
4.5.1 Droplet size measurement.....	75
4.5.1.1 High speed camera pictures	75
4.5.1.2 PVM pictures	77
4.5.2 Water cut measurement.....	78
4.5.3 Water-oil interfacial tension measurement	79
Chapter 5 Test Matrix	82
Chapter 6 Experimental Results and Discussion	84
6.1 Maximum droplet size results.....	84
6.1.1 Summary of results obtained in a standard pipe with mixing valve	85
6.1.1.1 Effect of turbulent dissipation rates	85
6.1.1.2 Effect of water cut.....	89
6.1.2 Summary of results obtained in the doughnut cell.....	93
6.1.2.1 Effect of turbulent dissipation rates	94
6.1.2.2 Effect of water cut.....	98
6.1.3 Summary of results obtained in the standard pipe	101
6.1.3.1 Effect of turbulent dissipation rate.....	101
6.1.3.2 Effect of water cut.....	107
6.1.4 Model improvement – Development of the ICMT model	110

6.1.4.1 Comparison between experimental data and ICMT model predictions..	112
6.1.4.2 Comparison between literature data and ICMT model predictions	120
6.1.4.3 Effect coalescence on maximum droplet size.....	123
6.2 Droplet size distribution results	129
6.2.1 Summary of results obtained in the standard pipe with mixing vale	131
6.2.2 Summary of results obtained with the Doughnut cell.....	135
6.2.3 Summary of results obtained with the standard pipe	138
6.2.4 Analysis of the Rosin-Rammler distribution parameters.....	140
6.2.5 Local water concentration calculation using Rosin-Rammler equation	151
Chapter 7 Conclusions and Recommendations.....	154
7.1 Maximum droplet size	155
7.2 Droplet size distribution conclusion	155
7.3 Recommendation	156
References:.....	158
Appendix I: Turbulent Modulation.....	161
Appendix II: Rosin-Rammler Parameters Data	165
Appendix III: Error Analysis	167
Appendix IV: Cumulative Frequency Droplet Size Distribution	176

List of Tables

	Page
Table 1. Comparison of Simmons data with Hinze model and Brauner model [5],[18].	42
Table 2. Literature experiments of maximum droplet size and droplet size distribution in turbulent flow.....	58
Table 3. Dimensions of the globe valve provided by the manufacturer.	72
Table 4. Test matrix for standard pipe flow.	82
Table 5. Test matrix for pipe flow with mixing valve.	82
Table 6. Test matrix for small scale doughnut cell test.....	83
Table 7. Experimental Rosin-Rammler distribution parameters.	165
Table 8. Companion between measured and Rosin-Rammler predicted maximum droplet size-Standard horizontal pipe configuration.	170
Table 9. Measurement error of turbulent dissipation rate and water cut.	171

List of Figures

	Page
Figure 1. Flow patterns of horizontal oil-water flow [7].	22
Figure 2. Couette flow between two circular walls [51].	56
Figure 3. Experimental flow loop (a) 3D drawing (b) Schematic.	65
Figure 4. (a) Oil tank (b) Water tank.	67
Figure 5. Oil/water Separator.	67
Figure 6. Mixing point of oil and water line (T-section) [30].	68
Figure 7. Transparent PVC pipe test section.	70
Figure 8. Test section including globe valve and sampling ports (Courtesy of Al Schubert).	71
Figure 9. (a) Globe valve at experimental facilities; (b) Schematic of the globe valve.	71
Figure 10. The prototype design of doughnut cell apparatus (Courtesy of Al Schubert).	74
Figure 11. Details of the PVM mounting in doughnut cell.	75
Figure 12. Sample picture of droplet in standard pipe flow	76
Figure 13. Sample picture of droplets.	77
Figure 14. Digital image processing	78
Figure 15. Karl Fischer instrument for measuring water content of liquid mixtures.	79
Figure 16. Tensiometer for measuring interfacial tension (Courtesy of K. E. Kee).	80
Figure 17. Measured maximum droplet size in relation to the energy dissipation rate at 5% average water cut - Standard pipe with mixing valve configuration.	86

Figure 18. Comparison between measured maximum droplet size and the Hinze/Brauner model predictions in relation to the energy dissipation rate at 5% average water cut. Standard pipe with mixing valve configuration.....	87
Figure 19. Measured maximum droplet size in relation to the energy dissipation rate at 10% average water cut - Standard pipe with mixing valve configuration.....	88
Figure 20. Comparison between measured maximum droplet size and the Hinze/Brauner model predictions in relation to the energy dissipation rate at 10% average water cut - Standard pipe with mixing valve configuration.....	89
Figure 21. Measured maximum droplet size in relation to the water cut at 122 and 220 <i>Wattkg</i> average turbulent dissipation rate - Standard pipe with mixing valve configuration.....	90
Figure 22. Comparison between the measured maximum droplet size and the Hinze/Brauner model predictions in relation to the water cut at average turbulent dissipation rate 122 <i>Wattkg</i> - Standard pipe with mixing valve configuration.....	91
Figure 23. Comparison between the measured maximum droplet size and the Hinze/Brauner model predictions in relation to the water cut at average turbulent dissipation rate 220 <i>Wattkg</i> - Standard pipe with mixing valve configuration.....	92
Figure 24. Comparison between measured horizontal loop with valve maximum droplet size and Hinze/Brauner model predictions - Standard pipe with mixing valve configuration.....	93
Figure 25. Measured maximum droplet size in relation to the energy dissipation rate at 5% average water cut - Doughnut cell configuration.....	95

Figure 26. Comparison between the measured maximum droplet size and the Hinze/Brauner model predictions in relation to the energy dissipation rate at 5% average water cut - Doughnut cell configuration.	96
Figure 27. Measured maximum droplet size in relation to the energy dissipation rate at 10% average water cut - Doughnut cell configuration.	97
Figure 28. Comparison between the measured maximum droplet size and the Hinze/Brauner model predictions in relation to the energy dissipation rate at 10% average water cut - Doughnut cell configuration.	98
Figure 29. Comparison between the measured maximum droplet size and the Hinze/Brauner model predictions in relation to the water cut at 2 <i>Wattkg</i> turbulent dissipation rate - Doughnut cell configuration.....	99
Figure 30. Comparison between the measured doughnut cell maximum droplet size and the Hinze/Brauner model predictions in relation to the water cut at 4 <i>Wattkg</i> turbulent dissipation rate - Doughnut cell configuration.....	99
Figure 31. Comparison between the measured maximum droplet size and the Hinze/Brauner model predictions in relation to the water cut at 7 <i>Wattkg</i> turbulent dissipation rate - Doughnut cell configuration.....	100
Figure 32. Comparison between the doughnut cell maximum droplet size data and Hinze/Brauner model predictions - Doughnut cell configuration.....	101
Figure 33. Measured maximum droplet size in relation to the energy dissipation rate at 1% average water cut – Horizontal standard pipe configuration.	102

Figure 34. Comparison between the measured maximum droplet size and the Hinze/Brauner model predictions in relation to the energy dissipation rate at 1% average water cut – Horizontal standard pipe configuration..... 103

Figure 35. Measured maximum droplet size in relation to the energy dissipation rate at 5% average water cut in vertical standard pipe flow – Vertical standard pipe configuration..... 104

Figure 36. Comparison between the measured maximum droplet size and the Hinze/Brauner model predictions in relation to the energy dissipation rate at 5% average water cut -- Vertical standard pipe configuration..... 105

Figure 37. Measured maximum droplet size in relation to the energy dissipation rate at 10% average water cut in vertical standard pipe flow-- Vertical standard pipe configuration..... 106

Figure 38. Comparison between the measured maximum droplet size and the Hinze/Brauner model predictions in relation to the energy dissipation rate at 10% average water cut-- Vertical standard pipe configuration..... 107

Figure 39. Comparison between the measured standard loop maximum droplet size and the Hinze/Brauner model predictions in relation to the water cut at 0.66 *Wattkg* average turbulent dissipation rates - Standard pipe configuration. 108

Figure 40. Comparison between the measured maximum droplet size and the Hinze/Brauner model predictions in relation to the water cut at 1.1 *Wattkg* average turbulent dissipation rates - Standard pipe configuration. 109

Figure 41. Comparison between the standard loop measured maximum droplet size and Hinze/Brauner model predictions.	110
Figure 42. Comparison between the measured maximum droplet size and the ICMT model predictions in relation to the water cut at average turbulent dissipation rate 122 <i>Wattkg</i> – Standard pipe with mixing valve configuration.	112
Figure 43. Comparison between the measured maximum droplet size and the ICMT model predictions in relation to the water cut at average turbulent dissipation rate 220 <i>Wattkg</i> – Standard pipe with mixing valve configuration.	113
Figure 44. Comparison between the measured maximum droplet size and ICMT model predictions – Standard pipe with mixing valve configuration.	114
Figure 45. Comparison between the measured maximum droplet size and the ICMT model predictions in relation to the water cut at 2 <i>Wattkg</i> turbulent dissipation rate – Doughnut cell configuration	115
Figure 46. Comparison between the measured maximum droplet size and the ICMT model predictions in relation to the water cut at 4 <i>Wattkg</i> turbulent dissipation rate – Doughnut cell configuration	115
Figure 47. Comparison between the measured maximum droplet size and the ICMT model predictions in relation to the water cut at 7 <i>Wattkg</i> turbulent dissipation rate – Doughnut cell configuration	116
Figure 48. Comparison between the doughnut cell maximum droplet size data and ICMT model predictions.	117

Figure 49. Comparison between the measured maximum droplet size and the ICMT model predictions in relation to the water cut at 1.1 <i>Wattkg</i> average turbulent dissipation rates – Standard pipe configuration	118
Figure 50. Comparison between the measured maximum droplet size and the ICMT model predictions in relation to the water cut at 0.66 <i>Wattkg</i> average turbulent dissipation rates - – Standard pipe configuration.....	119
Figure 51. Comparison between the standard pipe measured maximum droplet size and ICMT model predictions.....	120
Figure 52. Comparison of Hinze/Brauner model predictions with literature experimental maximum droplet size.....	121
Figure 53. Comparison of ICMT model predictions with literature experimental maximum droplet size.....	122
Figure 54. Comparing Hinze/Brauner model prediction errors with the ratio of breakup rate to coalescence rate in uniform dilute dispersion.....	125
Figure 55. Comparing Hinze/Brauner model prediction errors with the ratio of breakup rate to coalescence rate in uniform dense dispersion.....	126
Figure 56. Comparing Hinze/Brauner model prediction errors with the ratio of breakup rate to coalescence rate in non-uniform dilute dispersion.	126
Figure 57. Comparing ICMT model prediction errors with the ratio of breakup rate to coalescence rate in uniform dilute dispersion.....	127
Figure 58. Comparing ICMT model prediction errors with the ratio of breakup rate to coalescence rate in uniform dense dispersion.....	128

Figure 59. Comparing ICMT model prediction errors with the ratio of breakup rate to coalescence rate in non-uniform dilute dispersion.....	128
Figure 60. Example of a droplet size distribution obtained at 2.2% water cut and 205Watt/kg turbulent dissipation rate.....	130
Figure 61. Example of parameter $n(-)$ determination.....	131
Figure 62. Effect of energy dissipation rate on the measured droplet size distribution at 5% average water cut – Standard horizontal pipe with mixing valve configuration.	132
Figure 63. Effect of the energy dissipation rate on the measured droplet size distribution at 10% average water cut – Standard horizontal pipe with mixing valve configuration.	133
Figure 64. Effect of the water cut on the measured droplet size distribution at 122 <i>Wattkg</i> turbulent dissipation rate – Standard horizontal pipe with mixing valve configuration.	134
Figure 65. Effect of the water cut on the measured droplet size distribution at 220 <i>Wattkg</i> turbulent dissipation rate – Standard horizontal pipe with mixing valve configuration.	135
Figure 66. Effect of energy dissipation rate on the measured droplet size distribution at 5% average water cut – Doughnut cell configuration.....	136
Figure 67. Effect of the energy dissipation rate on the measured droplet size distribution at 10% average water cut – Doughnut cell configuration.....	136
Figure 68. Effect of the water cut on the measured droplet size distribution at 2 <i>Wattkg</i> turbulent dissipation rate – Doughnut cell configuration.	137

Figure 69. Effect of the water cut on the measured droplet size distribution at 6 *Wattkg* turbulent dissipation rate – Doughnut cell configuration. 137

Figure 70. Effect of energy dissipation rate on the measured droplet size distribution at 1% average water cut – Horizontal standard pipe flow configuration..... 138

Figure 71. Effect of the water cut on the measured droplet size distribution at 0.6 *Wattkg* turbulent dissipation rate - Horizontal standard pipe flow configuration. 139

Figure 72. Effect of the water cut on the measured droplet size at 1.1 *Wattkg* turbulent dissipation rate - Horizontal standard pipe flow. 139

Figure 73. Effect of turbulent dissipation rate on the Rosin-Rammler parameter *n*. 141

Figure 74. Effect of water cut on the Rosin-Rammler parameter *n*. 141

Figure 75. Effect of turbulent dissipation rate on the Rosin-Rammler parameter *d*₆₃(μm).
..... 142

Figure 76. Effect of water cut on the Rosin-Rammler parameter *d*₆₃(μm). 143

Figure 77. Effect of turbulent dissipation rate on the Rosin-Rammler parameter ratio *d*_{max}/*d*₆₃- measured *d*_{max}. 144

Figure 78. Effect of water cut on the Rosin-Rammler parameter ratio *d*_{max}/*d*₆₃- measured *d*_{max}. 145

Figure 79. Effect of turbulent dissipation rate on the Rosin-Rammler parameter ratio *d*_{max}/*d*₆₃- predicted *d*_{max}. 146

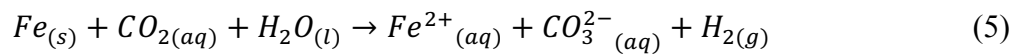
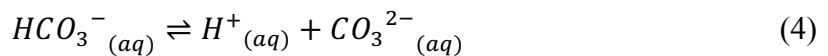
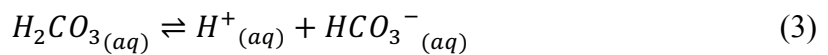
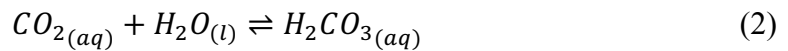
Figure 80. Effect of water cut on the Rosin-Rammler parameter ratio *d*_{max}/*d*₆₃- predicted *d*_{max}. 146

Figure 81. Effect of ratio of breakup rate to coalescence rate on the Rosin-Rammler parameter n	147
Figure 82. Effect of ratio of breakup rate to coalescence rate on the Rosin-Rammler parameter $d_{63}(\mu\text{m})$	148
Figure 83. Effect of ratio of breakup rate to coalescence rate on the Rosin-Rammler parameter ratio d_{max}/d_{63} -measured d_{max}	149
Figure 84. Effect of ratio of breakup rate to coalescence rate on the Rosin-Rammler parameter d_{max}/d_{63} -predicted d_{max}	150
Figure 85. Effect of Rosin-Rammler parameter $n(-)$ on local water concentration prediction.	153
Figure 86. Effect of droplet size ratio (d_{max}/d_{63}) on local water concentration prediction.	153
Figure 87. Measured maximum droplet size in relation to the water cut at 122 $Wattkg$ average turbulent dissipation rate - Standard pipe with valve configuration.....	168
Figure 88. PVM droplet pictures	169
Figure 89. High speed camera droplet pictures	169
Figure 90. Effect of energy dissipation rate on the measured droplet size distribution at 5% average water cut – Standard horizontal pipe with mixing valve configuration.	176
Figure 91. Effect of the energy dissipation rate on the measured droplet size distribution at 10% average water cut – Standard horizontal pipe with mixing valve configuration.	177

Figure 92. Effect of the water cut on the measured droplet size distribution at 122 <i>Wattkg</i> turbulent dissipation rate – Standard horizontal pipe with mixing valve configuration.	178
Figure 93. Effect of the water cut on the measured droplet size distribution at 220 <i>Wattkg</i> turbulent dissipation rate – Standard horizontal pipe with mixing valve configuration.	179
Figure 94. Effect of energy dissipation rate on the measured droplet size distribution at 5% average water cut – Doughnut cell configuration.	180
Figure 95. Effect of the energy dissipation rate on the measured droplet size distribution at 10% average water cut – Doughnut cell configuration.	180
Figure 96. Effect of the water cut on the measured droplet size distribution at 2 <i>Wattkg</i> turbulent dissipation rate – Doughnut cell configuration.	181
Figure 97. Effect of the water cut on the measured droplet size distribution at 6 <i>Wattkg</i> turbulent dissipation rate – Doughnut cell configuration.	181
Figure 98. Effect of energy dissipation rate on the measured droplet size distribution at 1% average water cut – Horizontal standard pipe flow configuration.	182
Figure 99. Effect of the water cut on the measured droplet size distribution at 0.6 <i>Wattkg</i> turbulent dissipation rate - Horizontal standard pipe flow configuration.	183
Figure 100. Effect of the water cut on the measured droplet size at 1.1 <i>Wattkg</i> turbulent dissipation rate - Horizontal standard pipe flow.	183

Chapter 1: Introduction

Oil transportation is one of the most important processes in the oil and gas industry. Oil lines typically carry a multiphase mixture of oil and water, two physically immiscible liquids. Pipeline corrosion is the one of the most critical issues causing pipeline failure. Corrosion takes place when water separates from the oil and contacts with the pipe internal surfaces, a phenomenon called “water wetting”. Water usually contains corrosive species such as organic acids and dissolved gases, which can react rapidly with the pipe internal surface [1]. Sweet corrosion is an common example of corrosion caused by the presence of dissolved gas ($CO_{2(aq)}$) [2]. The presence of $CO_{2(aq)}$ induces the formation of carbonic acid and an increased concentration of hydronium ions in the aqueous solution, as shown in Reactions 1, 2, 3, 4 [3]. The aqueous solution can react with the carbon steel pipe surface ($Fe_{(s)}$) and cause iron dissolution. The overall corrosion reaction in sweet environment is shown in Reaction 5. However, this process can be summarized into one cathodic (Reaction 6) and one main anodic (Reaction 7) reaction.





Accordingly, understanding when “water wetting” occurs is the first step in determining if corrosion is likely to happen. However, it gives no indication about the severity of the corrosion attack as this aspect is covered by chemical and electrochemical phenomena not investigated in this study.

1.1 Flow patterns

Water-in-oil flow patterns are helpful to describe “water wetting” [4]. The Trallero’s flow patterns: stratification, non-uniform dispersion and uniform dispersion, are used by researchers to represent water-in-oil flow patterns in a pipe cross section view [4],[5],[6]. As is shown in Figure 1, stratification means that the water phase separates from the oil phase, accumulates at the bottom of the pipe and wets the steel surface causing corrosion issues. This is due to the fact that water is typically denser than most liquid hydrocarbons. In contrast, non-uniform and uniform dispersion mean that the water phase is entirely entrained as droplets in the oil phase, the contact area between water and pipe internal surface is unstable, and little to no corrosion occurs [1].

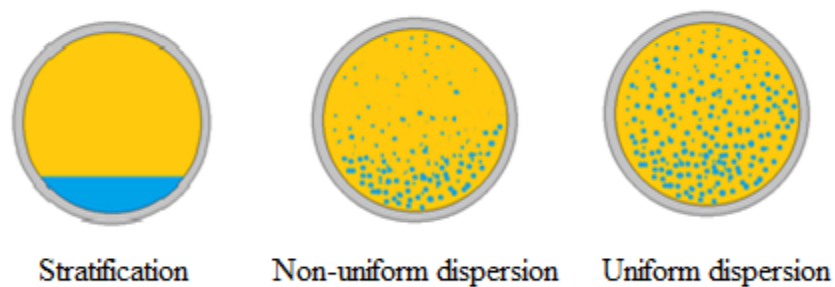


Figure 1. Flow patterns of horizontal oil-water flow [7].

Water-in-oil dispersion is usually formed in turbulent flow [1], [5], [8]–[12]. Non-uniform dispersion is usually formed at low turbulence level, where the water droplets are not uniformly distributed across the pipe cross section and are accumulating towards the bottom part of the pipe [1]. Uniform dispersion is commonly found at high turbulence level, where the water droplets are uniformly distributed in the pipe [1], [13]. Upstream environments (transportation of produced fluids from the well to the processing facilities) often operate at lower turbulent levels compared to downstream environments (refineries) where flow rates are typically much higher. For example, downstream operations such as desalinization processes require injection of water directly into the oil in order to remove salts (NaCl, MgCl₂, etc.). High turbulence level is typically thought in this process and obtained through the use of mixing devices (valves) [14]. As mentioned earlier, water-in-oil dispersion situation is preferred since it can prevent corrosion from occurring.

The transition from one flow pattern to another and the stability of a specific flow pattern directly depend on pipeline operating parameters such as water volume fraction, superficial oil and water velocities, fluid properties, pipe inclination, and pipe diameter.

There are two general requirements to achieve and maintain stable water-in-oil dispersion:

- The water volume fraction (water cut) must be lower than a critical value, called the inversion point
- The turbulence level must be high enough to ensure that water droplets remain entrained in the continuous oil phase

If the water cut is above a critical value, called the inversion point, the water-in-oil dispersion switches naturally to oil-in-water dispersion and water wetting occurs [15]. The consequence is that the water dispersion cannot remain suspended at any level of turbulence [16]. However, water wetting can still happen even if the water cut is below the inversion point. The turbulence level needs sufficiently high to maintain the dispersion of droplets [17]. Otherwise, droplets will eventually fall down and form a stratified layer on the pipe bottom surface. The predictions of these critical operating parameters for water-in-oil dispersion are calculated using the maximum droplet size and droplet size distribution, as reported in multiple studies [7], [16], [17].

1.2 Importance of studying droplet size

The maximum size and the size distribution of the dispersed water droplets are essential in determining if the operating conditions can lead to stable water-in-oil dispersed flow.

1.2.1 Maximum droplet size

Studying the *maximum dispersed water droplet size* is needed to determine whether the turbulence level is high enough to maintain stable dispersion. The turbulent flow leads to turbulent stress acting on the surface of water droplets and causes droplets breakup into smaller ones [18]. The maximum droplet size is defined as the largest size a droplet can achieve in the turbulent flow [18]. Droplets that are larger than the maximum droplet size can be broken up into smaller droplets due to turbulence [19]. Smaller droplets can then coalesce to become large droplets. Droplet breakup occurs when the turbulent stress is larger than the droplet internal surface stress holding the droplet shape.

The turbulent stress also drives the droplet movement. Droplet naturally fall towards the pipe bottom due to gravity, but the turbulent stress acts by homogenizing the mixture and by moving the droplet upward [20].

As mentioned earlier, keeping the droplets in suspension is the key in avoiding water wetting. This occurs when the turbulence level is high enough so that droplets remain too small to be effectively attracted to the bottom of the pipe due to gravity. The higher the turbulence level is, the smaller the maximum viable droplet size is and the less likely oil-water stratification can occur [18]. In addition, a high turbulence level can provide enough turbulent stress to lift even the largest droplets and prevent them from falling to the bottom [20]. This is the key criterion for determining stable water-in-oil dispersion: “the maximum size a droplet can have without breaking up must be smaller or equal to the size of the largest droplet that can be entrained in the flow without falling at the bottom of the pipe due to gravity (also called *critical droplet size*)”.

If the droplets fall to form a stratified flow, the solution would be to increase the turbulence level until the dispersion is suspended.

1.2.2 Droplet size distribution

In case of uniform dispersion, the local water concentration is uniform across the pipe cross section. The water cut is calculated as the ratio of water superficial velocity and mixture (oil + water) superficial velocity.

In case of non-uniform dispersion, the water cut is not uniform along the vertical direction in the pipe cross section. In other words, the local water concentration (value of water droplet concentration at certain locations in the pipe) close to the bottom of the

pipe can be higher than in the bulk fluid [15]. Stable dispersion requires that the local water concentration, even close to the bottom of the pipe, must be lower than the inversion point. The calculation of the local water concentration requires the determination of droplet size distribution across the pipe cross section [21]. In addition, the droplet size distribution provides specific information about the whole droplet population in non-uniform dispersion.

Chapter 2 Literature Review

Accurate experimental data assessing the effect of flow conditions and physiochemical characteristics of fluids are needed to determine the maximum droplet size and the droplet size distribution. Since it is difficult to perform experiments covering every single condition, prediction tools following either an empirical or a mechanistic approach have been proposed by many researchers [5], [7]–[9], [11], [18], [22]–[28]. An empirical methodology directly uses statistical regression of experimental data to predict droplet sizes [22], [25]–[27]. It generates mathematical equations which are only loosely based on mechanisms. A common challenge faced by empirical models is that their domain of validity cannot be easily extended without new data [7]. A mechanistic method is often preferred when there is an interest in developing an approach based on the understanding of mechanisms and of the effect of physiochemical properties. This approach is taken by a number of authors [5], [7]–[11], [13], [15], [18], [22]–[24], [28], [29] and has been chosen for this work as well. The sections below present the most advanced and accepted approaches, some mechanistic and some empirical, to determine water wetting and droplet sizes in oil/water dispersed flow.

2.1 Water wetting model for oil-water flow

The purpose of modeling water wetting is to determine the flow pattern transition between dispersed water-in-oil flow (no water wetting) and stratified water-in-oil flow (water wetting) [30]. The flow pattern transition determination requires two comparisons:

- Maximum droplet size versus critical droplet size
- Local water concentration versus inversion point

2.1.1 Comparing maximum droplet size and critical droplet size

Every droplet in dispersion has the tendency to fall towards the bottom of the pipe due to the effect of gravity. The oil phase provides turbulent stress which act on droplets surface with the effect of lifting them upward and maintaining the dispersion. If the size of a given droplet is larger than a critical value $d_{critical}(\mu\text{m})$, the droplet becomes too heavy to be lifted and falls to the bottom of the pipe. If the right conditions are met, droplets accumulating closed to the pipe wall can coalesce and form a stratified water layer causing water wetting. On the contrary, if the size of a given droplet is smaller or equal to the critical droplet size, the turbulent flow will lift the droplet and maintain it in suspension [20]. Associated with the concept of maximum droplet size $d_{max}(\mu\text{m})$ (largest size a droplet can be achieved in the turbulent flow), this approach gives a practical criterion for determining the onset of water wetting. It is discussed in more details below.

If $d_{critical} \geq d_{max}$ is confirmed, full dispersion is maintained.

If $d_{critical} < d_{max}$ is confirmed, dispersion is not maintained and water wetting occurs.

The critical droplet size $d_{critical}(\mu\text{m})$ is calculated based on the balance of gravitational force $F_g(N)$ and turbulent force $F_T(N)$ applied on droplet [20]:

$$F_T = F_g \quad (1)$$

$$F_T = \frac{1}{2} \rho_c \frac{\pi d_{critical}^2}{4} C_D v'_{rms}{}^2 \quad (2)$$

$$F_g = \frac{\pi d_{critical}^3}{6} \Delta \rho g \quad (3)$$

where, $\Delta\rho(\text{kg/m}^3)$ is density difference between oil phase and water phase, $\rho_c(\text{kg/m}^3)$ is density of the continuous oil phase, C_D is the droplet drag coefficient, v'_{rms} (m/s) is the root mean square velocity fluctuation which can be estimated in function of the friction velocity [20]:

$$v'_{rms}{}^2 = u^{*2} = \frac{1}{2}\rho_c f u_m^2 \quad (4)$$

The droplet drag coefficient C_D of water droplets with unmovable oil-water interfaces is calculated using the Stokes equation for Droplet Reynolds number $Re_d \leq 1$:

$$C_D = \frac{24}{Re_d} \quad (5)$$

and using Schiller and Naumann's equation for Droplet Reynolds number $1 < Re_d < 1000$ [31]:

$$C_D = \frac{24}{Re_d} (1 + 0.15Re_d^{0.687}) \quad (6)$$

Finally, the $d_{critical}(\mu\text{m})$ can be calculated:

$$d_{critical} = \frac{3\rho_c C_D v'_{rms}{}^2}{4\Delta\rho g} \quad (7)$$

The next step is to determine the maximum droplet size. This step is actually a central aspect of this study and is shown in details in Chapter 2.2.1. It is consequently bypassed in this introductory section.

2.1.2 Comparing local water concentration with inversion point

The local water concentration must be lower than inversion point in order to avoid water/oil stratification [21]. If the maximum local water concentration reaches the

inversion point, the water-in-oil dispersion switches naturally to oil-in-water dispersion, and water wetting occurs [28].

The maximum local water concentration is usually found at the bottom of the pipe (C_{bottom}) in horizontal flow and should be kept below the inversion point (C_{inv}) in order to avoid water/oil stratification and water wetting.

$$C_{\text{local}} \leq C_{\text{inv}} \quad (8)$$

where, the inversion point is calculated with the following equation [16]:

$$C_{\text{inv}} = 0.5 - 0.1088 \log_{10} \left(\frac{\mu_c}{\mu_d} \right) \quad (9)$$

Here, μ_c ($Pa \cdot s$) and μ_d ($Pa \cdot s$) are the viscosities of continuous oil phase and dispersed water phase.

The calculation of the local water concentration $C_{\text{local}}(-)$ at any height of the horizontal pipe along the radial-vertical direction is performed using a diffusion model [21]. This diffusion model is developed from the equation of continuity for a component of a mixture in Cartesian coordinates, ignoring chemical reactions [32]:

$$\frac{\partial C}{\partial t} = - \left(\frac{\partial U_x C}{\partial x} + \frac{\partial U_y C}{\partial y} + \frac{\partial U_z C}{\partial z} \right) + \varepsilon \left(\frac{\partial^2 C}{\partial x^2} + \frac{\partial^2 C}{\partial y^2} + \frac{\partial^2 C}{\partial z^2} \right) \quad (10)$$

where, $\frac{\partial C}{\partial t}$ is the rate of change in fluid volumetric concentration or volume fraction $C(-)$,

$-\left(\frac{\partial}{\partial x} U_x C + \frac{\partial}{\partial y} U_y C + \frac{\partial}{\partial z} U_z C \right)$ is the rate of change in $C(-)$ by convection, U_x , U_y , U_z

(m/s) are fluid velocities, $\varepsilon \left(\frac{\partial^2 C}{\partial x^2} + \frac{\partial^2 C}{\partial y^2} + \frac{\partial^2 C}{\partial z^2} \right)$ is the rate of change in $C(-)$ by diffusion,

and ε (m^2/s) is the fluid diffusivity.

The calculation of the local water concentration considers changes in volumetric concentration in only one-dimension (y coordinate only). For steady state conditions, the fluid concentration $C(-)$ remains constant as time $t(s)$ changes, so $\frac{\partial C}{\partial t} = 0$ [21]. The continuity equation can be simplified as:

$$0 = -\frac{\partial C U_y}{\partial y} + \varepsilon \frac{\partial^2 C}{\partial y^2} \quad (11)$$

Applying this conservation equation to a family of water droplets of diameter $d_j(-)$ and considering corresponding volumetric concentration $C_j(-)$ at location $y(m)$ in water-in-oil flow, the following equation is obtained:

$$0 = -\frac{\partial \sum_j C_j U_j}{\partial y} + \varepsilon_j \frac{\partial^2 \sum_j C_j}{\partial y^2}, \quad j = 1,2,3, \dots n \quad (12)$$

where, $\varepsilon_j(m^2/s)$ is the diffusivity for the water droplet, the droplet velocity $U_j(m/s)$ is calculated as:

$$U_j = v_y - w_j \quad (13)$$

here, $v_y(m/s)$ is the continuous phase oil velocity in the vertical direction y , $w_j(m/s)$ is the droplet settling velocity. Assuming that the water droplet diffusivity $\varepsilon_j(m^2/s)$ for different droplet size is constant ($\varepsilon_j = \varepsilon$), and that there is zero net droplet flux in the y direction, this equation can be further simplified as:

$$0 = -\sum_j C_j (v_y - w_j) + \varepsilon \frac{\partial \sum_j C_j}{\partial y}, \quad j = 1,2,3, \dots n \quad (14)$$

Similarly, the simplified equation for continuous oil phase is also obtained as:

$$0 = - \left[1 - \sum_i C_i \right] v_y + \varepsilon_l \frac{\partial}{\partial y} \left[1 - \sum_i C_i \right], \quad i = 1, 2, 3, \dots, n \quad (15)$$

Where, C_i is the local volume fraction of water droplets, and the oil diffusivity is $\varepsilon_l (m^2/s)$ [21]. Reorganizing the above equations, it yields:

$$0 = -C_j \left(\frac{\varepsilon_l \sum_i w_i C_i}{\varepsilon + (\varepsilon_l - \varepsilon) \sum_i C_i} - w_j \right) + \varepsilon_j \frac{\partial C_j}{\partial y} \quad (16)$$

The continuous phase oil velocity in the vertical direction can be calculated as:

$$v_y = \frac{\varepsilon_l \sum_i w_i C_i}{\varepsilon + (\varepsilon_l - \varepsilon) \sum_i C_i} \quad (17)$$

Assuming the oil diffusivity is similar to the water droplet diffusivity $\varepsilon_l = \varepsilon$, the expression of $v_y (m/s)$ further simplifies to:

$$v_y = \sum_{i=1}^n C_i w_i \quad (18)$$

Equation 14 can be rearranged as following developments:

$$0 = - \sum_j C_j \left(\sum_i C_i w_i - w_j \right) + \varepsilon \frac{\partial \sum_j C_j}{\partial y} \quad (19)$$

$$0 = - \sum_j C_j \sum_i C_i w_i + \sum_j C_j w_j + \varepsilon \frac{\partial \sum_j C_j}{\partial y} \quad (20)$$

$$\sum_i C_i w_i = \sum_j C_j w_j \quad (21)$$

$$0 = \sum_j C_j w_j (1 - \sum_j C_j) + \varepsilon \frac{\partial \sum_j C_j}{\partial y} \quad (22)$$

Considering $\sum_i C_i (-)$ is the total volumetric concentration by summing all the droplets volume fractions at location $y(m)$:

$$\sum_{j=1}^n C_j(y) = C(y), \quad j = 1, 2, 3, \dots, n \quad (23)$$

Then, Equation 22 is applied to a uniform droplet size dispersion, assuming all the dispersed water droplets size are equal to the median droplet size $d_j = d_{median}$. Here, the median droplet size $d_{median} = d_{50}$ is the diameter at which 50% of the sample volume is comprised of smaller droplets [21]. The droplet settling velocity $w_j(m/s)$ corresponding to the size $d_j(m)$ is simplified as $w_j = w$ [21]. Equation 22 is finally simplified as:

$$0 = C(y)w(1 - C(y)) + \varepsilon \frac{\partial C(y)}{\partial y} \quad (24)$$

Where, the local water concentration is $C(y) = C_{local}$, the settling velocity is $w = U_s$ for the median droplet size d_{50} (μm) [21]. The final calculation of the local water concentration is:

$$(1 - C_{local})C_{local}U_s + \varepsilon \frac{\partial C_{local}}{\partial y} = 0 \quad (25)$$

where, the droplet settling velocity $U_s(m/s)$ of droplets corresponding to the median droplet size $d_{50}(m)$ is calculated as follows[21]:

$$U_s = \sqrt{\frac{4}{3} \frac{d_{50}(\rho_d - \rho_c)g}{\rho_c C_D}} \quad (26)$$

where, $\rho_c(kg/m^3)$ is the continuous oil phase density, $\rho_d(kg/m^3)$ is the dispersed water phase density, C_D is the droplet drag coefficient which is which is calculated using Equation 6. The $d_{50}(m)$ is calculated using Rosin-Rammler equation which is discussed in Chapter 2.2.2.1. The droplet diffusivity $\varepsilon(m^2/s)$ is calculated as follows:

$$\varepsilon = \zeta u^* \frac{D}{2} \quad (27)$$

where, $D(m)$ is the pipe diameter, $\zeta(-)$ is the dimensionless turbulent eddy diffusivity which is a dimensionless constant: $\zeta = 0.25$ [21]. According to Karabelas' experimental data, this value can also vary with the droplet Reynolds number $Re_p(-)$ [21]:

$$\zeta = 0.0935 Re_p^{0.154} \quad (28)$$

The friction velocity $u^*(m/s)$ is:

$$u^* = \sqrt{\frac{\rho_m f}{2\rho_c}} U_m \quad (29)$$

where, $\rho_m(kg/m^3)$ is the mixture density of the water-oil phase, $U_m(m/s)$ is the mixture flow velocity, $f(-)$ is a friction factor: $f = \frac{0.046}{Re^{0.2}}$.

Accurate droplet size distribution model predictions are needed to determine the median droplet size d_{50} (μm) which is turn fed in the Karabelas' local water concentration model. The determination of droplet size distribution is also a crucial aspect of this study and is shown in details in Chapter 2.2.2.

2.2 Modeling droplet sizes

Droplet breakup and coalescence are responsible for the determination of droplet sizes in turbulent water-in-oil dispersion [33]. Droplet breakup can be represented by the splitting of one droplet into two or more. Droplet coalescence occurs when two droplets interact with each other and form one single larger droplet. Although these two processes occur simultaneously in turbulent flow, the rates of droplet coalescence and breakup are not always comparable and one phenomenon can overcome the other one depending on

the application. For example, in the transportation of crude oil flow, it is commonly accepted that water droplet breakup is the dominant mechanism determining the droplet size and that the effect of coalescence can be neglected. This is due to the natural presence of solids and surface active compounds in water/crude oil system which inhibit droplet coalescence [34]–[36]. On the other hand, water droplet coalescence cannot be neglected in multiphase natural gas lines when the liquid phase is made of light condensate and water and is free of surfactants. In this case, the droplet sizes are affected by both droplet breakup and coalescence mechanisms [13].

As mentioned in Chapter 1.2.1, droplet breakup is controlled by the balance between the external stress created by the bulk flow which tends to break droplets and the opposing surface tension which tends to keep droplets together [18]. This mechanism of droplet breakup is the most commonly accepted approach for prediction of maximum droplet size (diameter of the largest droplet that can exist in turbulent flow) [13]. The maximum droplet size decreases when the interfacial tension decreases, and/or when the turbulence level increases [18]. Another useful parameter that can be extracted from this modeling approach is the droplet breakup rate (volume of broken droplet per unit of time) [37]. The droplet breakup rate decreases when the droplet size decreases and/or the turbulent level increases. The maximum droplet size and the droplet breakup rate calculations are discussed in Chapter 2.2.1 and in Chapter 2.3.1, respectively.

Droplet coalescence is a more complex phenomenon compared to droplet breakup [38]. As for droplet breakup, coalescence is strongly affected by the external turbulent stress caused by the bulk flow but it also depends on droplet-droplet dynamic interaction

[33]. The external turbulent stress applied on the droplet surface induces droplets' dynamic oscillation. The relative velocity between crowded droplets is the main driver of droplet-droplet interaction [33]. Considering that a thin oil film is the only fluid separating two droplets, the process of coalescence is actually very similar to the film thinning mechanism [39]. As the droplets get closer, the oil film thickness decreases and eventually reaches a critical thickness [39]. At this critical point, the oil film ruptures and the two water droplets overcome their surface stresses to coalesce into one single droplet [40]. Most studies have focused on the calculation of coalescence rate (the volume of coalesced droplet per unit time) [40]. Details of the calculation of droplet i.e. coalescence rate are discussed in Chapter 2.3.2. The collision rate increases when turbulence level and/or coalescing droplets sizes increase [33].

It is worth noticing that all the current maximum droplet size prediction models rely only on the mechanisms of droplet breakup [13]. These models assume, for better or worse, that the droplet coalescence rate is extremely low relative to droplet breakup rate and can be neglected [13].

Finally, most droplet size distribution models are empirically generated from a set of experimental data and no mechanistic approach has been used so far. Empirical correlations derived from the Rosin-Rammler equation and the log-normal function are commonly used to predict droplet size distribution [8], [41].

The modeling approaches developed for the calculation of maximum droplet size and droplet size distribution are described in more detailed below.

2.2.1 Maximum droplet size prediction

Many research studies have been conducted on the determination of maximum droplet size in turbulent dispersion of two immiscible fluid [5], [8]–[11], [17], [18], [22], [24], [29]. The most fundamental models were developed by Hinze [18] and Brauner [17]. These models are based on the mechanism of droplet breakup while the effect of droplet coalescence is completely neglected.

2.2.1.1 Maximum droplet size model for dilute dispersion (Hinze Model)

Hinze was the first to develop a comprehensive mechanistic explanation focused on the balances of forces acting on droplets dispersed in a continuous phase. This work, still fundamental today, generated criteria defining the transition between dispersed and stratified flow. Hinze model predicts the maximum droplet size in dilute water-in-oil dispersion, where the water cut is less than 5% [18]. As mentioned before, the maximum droplet size d_{max} (μm) is defined as the largest size a droplet can achieved in the turbulent flow. Since the low volume fraction of the dispersed phase leads to a negligible chance of coalescence, the maximum droplet size depends entirely on the breakup motion [18]. Water droplets larger than d_{max} (μm) break naturally under the effect of turbulent stress and viscous shear stress [18],[42]. Turbulent stress is the dynamic stress of the turbulent motion, which impacts droplets and can break them. Viscous shear stress is the friction stress acting on the droplet surface due to the gradient of velocity at the interface which pulls the droplet apart and break it [42]. However, the viscous shear action is negligible in turbulent flow except very closed to the solid surface, such as the pipe

surface [18]. Violent turbulent motion is needed to generate and maintain the dispersion and the turbulent stress dominates the breakup motion.

The droplet shape is stable when the turbulent stress and the water droplet surface stress are balanced. As mentioned earlier, the turbulent stress τ (N/m²), applied by the continuous oil phase, tends to break the water droplet. However, the water droplet surface stress $\frac{\sigma}{d_{max}}$ (N/m²) prevents the droplet from breakage, where σ (N/m) is the interfacial tension between the droplet surface and the oil phase. The ratio of the turbulent and surface stresses is represented as the dimensionless Weber number $We_{crit} = \frac{\tau d_{max}}{\sigma}$ [28]. Based on the stress balance concept, $\tau = We_{crit} \frac{\sigma}{d_{max}}$, Hinze developed a model for the prediction of maximum droplet size in water-in-oil flow [18]:

$$\frac{1}{2} \rho_c \overline{u'^2} = C \frac{4\sigma}{d_{max}} \quad (30)$$

In Equation 30, C is the fitted constant. The Laplace surface stress of a droplet, $\frac{4\sigma}{d_{max}}$ (N/m²) represents the surface stress of the water droplet. In Equation 30, $\frac{1}{2} \rho_c \overline{u'^2}$ (N/m²) represents the turbulent stress of the continuous oil phase applied to the surface of the water droplet. The density of the oil phase is ρ_c (kg/m³). The mean value of the squares of velocity fluctuations, created by turbulent eddies, over a length scale value similar to d_{max} (μm) is $\overline{u'^2}$ (m²/s²) [18]. The length scale value d_{max} (μm) is in the range of $l_k < d_{max} < 0.1D$, where, D (cm) is the pipe diameter, l_k is the Kolmogoroff length scale which is the smallest valid length scale in turbulence. Where, $l_k = \left(\frac{\mu_c^3}{\bar{\epsilon} \rho_c}\right)^{1/4}$, μ_c (Pa · s) is the viscosity of continuous oil phase, $\bar{\epsilon}$ (Watt/kg) is the turbulent dissipation rate.

A water droplet can only be affected by velocity fluctuations u' (m/s) created by eddies which length scale is similar to the droplet diameter. If the eddy length scale is too large in this region, it will only move the droplet instead of breaking it. If the eddy length scale is too small, it will neither move nor break the droplet. Hinze [18] correlated $\overline{u'^2}$ (m^2/s^2) with length scale d_{max} (μm) by using the Kolmogorov energy distribution law [43]:

$$\overline{u'^2} = 2(\bar{\epsilon}d_{max})^{2/3} \quad (31)$$

where, $\bar{\epsilon}$ is the turbulent dissipation rate (kw/kg) which can be expressed in terms of superficial velocity of the continuous oil phase U_c (m/s) in pipe flow [7]:

$$\bar{\epsilon} = 2 \frac{fU_c^3}{D} \frac{\rho_m}{\rho_c(1-\epsilon)} = \frac{\Delta P U_c}{\Delta L \rho_c(1-\epsilon)} \quad (32)$$

Here, the friction factor f in pipe flow is calculated by Blasius equation: $f = \frac{0.046}{Re^{0.2}}$, Re is the Reynolds number of the flow, D (m) is the pipe internal diameter, ρ_m (kg/m^3) is water-in-oil mixture density, $\rho_m = \rho_d \epsilon + \rho_c(1-\epsilon)$, ρ_c (kg/m^3) is continuous phase (oil) density, ρ_d (kg/m^3) is dispersed phase (water) density, and ϵ (–) is the water cut.

The turbulent dissipation rate in pipeline can also be calculated in terms of pressure loss, ΔP (pa) over a distance of ΔL (m). The specific calculation of turbulent dissipation rate, as it relates to the experimental setups selected for this study, is discussed in Chapter 2.4.

Hinze improved his maximum droplet size model (Equation 30) with calibration with experimental data [18],[22]:

$$d_{max} = 0.725 \left(\frac{\sigma}{\rho_c} \right)^{3/5} \bar{\epsilon}^{-2/5} \quad (33)$$

The fitted constant C was found as 0.725 with a standard deviation of 0.315. In all experimental data, the water cut of the dispersed water phase ranged from 0.009 to 0.048 which is representative of dilute dispersions. Consequently, this modeling approach for prediction of maximum droplet size is not meant to be valid for conditions outside its range of validity (i.e. dilute dispersion).

It is worth mentioning that Hinze model states that maximum droplet sizes are inversely proportional to the turbulent dissipation rate at a power of $-2/5$: $d_{max} \propto f(\sigma, \rho_c) \bar{\epsilon}^{-2/5}$ [18].

2.2.1.2 Maximum droplet size model for dense dispersion (Brauner Model)

Brauner proposed a model for dense dispersion, where the water cut of dispersed phase is higher than 5% but lower than the inversion point [44]. Brauner used Hinze's dilute dispersion model as a starting point and developed a new criterion to predict the maximum water droplet size in dense dispersion [17], [18]. Brauner mentioned that water droplets in dense dispersion have larger chances of impacting each other and coalesce into larger droplets due to the increased water cut [17]. However, the effect the coalescence was still not included in this model. Rather, the effect of water cut is introduced.

Brauner introduced a balance between the rate of surface energy production and the rate of turbulent energy supply [17], shown in Equation 34:

$$\frac{1}{2} \rho_c \overline{u'^2} Q_c = C_H \frac{6\sigma}{d_{max}} Q_d \quad (34)$$

The continuous oil phase, with a flow rate of Q_c (m^3/s), supplies the turbulent energy rate $\frac{1}{2} \rho_c \overline{u'^2} Q_c$ (J/s) to the disperse water phase. The water droplets phase, with a flow

rate of Q_d (m^3/s), supplies the surface energy production rate $\frac{6\sigma}{d_{max}}Q_d$ (J/s) that hold the droplets in stable shape without breakage [17]. The turbulent energy decreases as the oil volume fraction decreases. The average external turbulent energy rate in the continuous oil phase is equated to the rate of surface energy production using a fitting constant $C_H(-)$ introduced to describe how much turbulent energy in continuous oil phase is applied to disperse the water phase. Brauner derived a final expression of the maximum droplet size as a function of the *in-situ* water cut $\varepsilon_d(-)$ [17]:

$$d_{max} = \left(\frac{C_H 6\sigma}{\rho_c} \frac{\varepsilon_d}{(1 - \varepsilon_d)} \right)^{3/5} \bar{e}^{-2/5} \quad (35)$$

$$\varepsilon_d = \frac{U_d}{U_d + U_c} \quad (36)$$

where, U_d (m/s) is the superficial velocity of dispersed water phase and U_c (m/s) is the superficial velocity of continuous oil phase, C_H is defined as 1.

Simmons [5] compared measured maximum water drop sizes in dilute and dense dispersion with predictions from Hinze model, Equation 33, and Brauner model, Equation 35, while varying the water cut and oil phase superficial velocity, as shown in Table 1 [17], [18].

Table 1. Comparison of Simmons data with Hinze model and Brauner model [5],[18].

Water cut (%)	Oil Superficial velocity (m/s)	Measured d_{max} (μm)	Hinze model prediction d_{max} (μm)	Brauner model prediction d_{max} (μm)	Hinze model Percentage error (%)	Brauner model Percentage error (%)
1.2	2.39	639	604	175	5	73
1.5	1.84	599	815	267	36	55
1.9	1.49	613	1018	388	66	37
3.3	0.84	1354	1861	1010	37	25
6.2	2.39	1577	549	441	65	72
9.6	1.49	1636	925	925	43	43
11.7	2.39	1567	530	599	66	61
15.9	0.84	1794	1636	2199	9	22
16.9	2.39	1538	490	698	68	54
17.5	1.49	1508	826	1202	45	20
20.4	2.39	1528	451	757	71	50
24.7	1.49	1419	757	1330	47	6
27.5	0.84	1775	1399	2615	21	47
29.2	1.49	1488	717	1379	52	7
36.8	0.84	1824	1192	2694	35	47
42.3	0.84	1706	1073	2684	37	57

Both Hinze's model [18] and Brauner's model [17] predict the correct trend: the maximum droplet size decreases as the turbulent dissipation rate increases. However, Brauner's model [17] does not perform any more accurately than Hinze's model in dilute or dense dispersion [18]. The error values seem to be randomly distributed without any clear relationship with flow conditions (U_c , ε_d). It should also be mentioned that the data themselves could lack accuracy so the whole discrepancy cannot be entirely blamed on the model.

Anyhow, the existing prediction models mentioned above are generated by analyzing experimental data. These data cover only a limited range, and the models' validity is consequently limited too. Consequently, more experimental data and analysis

are needed to improve the current models and validate them over a wider range of flow conditions and fluid properties.

2.2.2 Droplet size distribution prediction

Determining the droplet size distribution is an essential step in calculating the local water concentration of an oil/water mixture. If the dispersion is homogeneous, the water cut is constant across the entire pipe cross section. However, in case of lower level of turbulent mixing, a gradient in water cut can be created due to the difference in fluid density. Water droplets can accumulate at the bottom part of the pipe and lead to a local higher water concentration which can in some case even surpass the inversion point.

The Rosin-Rammler equation and the Log-normal function are commonly used to predict droplet size distribution. These correlations are empirical, as they do not represent any physical phenomenon. They both required a set of experimental data, specific to the oil-water system considered, in order to determine constants used in the correlations.

Droplet population balance equation (PBE) is another well-known approach for prediction of droplet size distribution. One of the challenges encountered with the formulation of PBE lies within the determination of accurate droplet breakup and coalescence rates. As mentioned earlier, these functions are complex and strongly dependent on experimentally determined constants which can vary dramatically from one oil-water system to another [13]. Although several models for the prediction of coalescence and breakup rates have been proposed, more independent experimental observations of breakup and coalescence processes are still needed to improve the prediction accuracy and comprehensiveness [37], [40]. Instead of using the PBE

approach, the simpler, yet more practical, Rosin-Rammler equation is selected in this study.

2.2.2.1 Rosin-Rammler equation

Karabelas was the first to introduce the Rosin-Rammler equation as a way to predict the cumulative droplets size distribution across a pipe section [8], [41]. This model is shown as:

$$V = 1 - \exp \left[- \left(\frac{d}{d^*} \right)^n \right] \quad (37)$$

In Equation 37, the cumulative volume fraction $V(-)$ is correlated to the droplet diameter $d(\mu\text{m})$. Here, $V(-)$ is the volume fraction of water droplets that have a diameter larger than d (μm). This model uses parameters labelled d^* (μm) and n which are empirically generated from a set of experimental data. The parameter d^* (μm) is the droplet diameter corresponding to the cumulative volume fraction $V = 0.632$ and is often identified as d_{63} (μm) [8]. The parameter n is the slope of the distribution in log-log plot [8]. Karabelas replaced d_{63} (μm) with d_{95} , which is close to d_{max} [8], and revised the equation as follows:

$$V = 1 - \exp \left[-2.996 \left(\frac{d}{d_{95}} \right)^n \right] \quad (38)$$

The droplet size d_{95} (μm) is calculated using the maximum droplet size prediction model. The average slope $n = 2.62$ is empirically generated from Karabelas' experimental data [8]. Angeli also fitted her experiment data and found an average slope $n = 2.53$ which is fairly close to Karabelas' results [9].

2.2.2.2 Log-normal function

Another distribution function that Karabelas [8] introduced is the log-normal function, shown as Equation 39. The cumulative fraction $f(d)$ is the fraction of water droplets that have diameters (μm) smaller than d :

$$f(d) = 1 - \frac{1}{2}[1 - \text{erf}(\delta z)] \quad (39)$$

in Equation 39, the parameters are described below:

$$z = \ln \left[\frac{ad}{d_{max} - d} \right] \quad (40)$$

$$a = \frac{d_{max} - d_{50}}{d_{50}} \quad (41)$$

$$\delta = \frac{0.394}{\log_{10} \left| \frac{v_{90}}{v_{50}} \right|} \quad (42)$$

where, $v_i = d_i/(d_{max} - d_i)$, parameters, d_{10} , d_{50} , d_{90} , and maximum droplet diameter d_{max} are empirically generated from Karabelas' experimental data [8]. Here, d_{50} (μm) is the droplet diameter at which 50% of the entire water volume is comprised of smaller droplets. Similarly, d_{10} (μm) is the droplet diameter corresponding to a cumulative fraction of 10%, and d_{90} (μm) is the droplet diameter corresponding to a cumulative fraction of 90%.

To predict the cumulative droplet size distribution, Karabelas used both the Rosin-Rammler and the log-normal equations [8]. However, Angeli found that the Rosin-Rammler equation is less complex to implement than the log-normal equation [9]. The log-normal equation requires the determination of three experimental parameters d_{10} ,

d_{50} , d_{90} , whereas the Rosin-Rammler equation only needs two experimental parameters d^* and n [9]. In addition, Angeli reported that the results of Rosin-Rammler equation displayed a better fit with experimental data points compared to the log-normal equation [9]. Consequently, the Rosin-Rammler equation is used in this study.

Although the Rosin-Rammler function represents a simpler and more practical choice, it is still an empirical correlation which domain of validity cannot be extended beyond the experimental data points with which it was formulated. In order to improve the accuracy and the domain of validity of the predictions, flow characteristics and fluid physiochemical properties must be considered.

2.3 Droplet breakup rate and coalescence rate

Hinze and Brauner maximum droplet size models are based on the mechanism of droplet breakup and neglect the effect of coalescence. However, coalescence can play, in some cases, an essential role in maximum droplet size prediction [17]. Coualoglou and Tavlarides proposed that droplets would simultaneously undergo breakup and coalescence [13]. Consequently, the steady state droplet size should eventually be affected by the balance of breakup rate and coalescence rate [13]. Ideally, breakup rates could be compared with coalescence rates to obtain relative effects on droplet size predictions.

2.3.1 Droplet breakup rate prediction

Prediction models have been proposed to quantify the droplet breakup rate in turbulent droplet dispersion [13]. The rate of droplet breakup is typically defined with the variable $g(d_b)(\text{m}^3/\text{s})$ which describes the cumulative volume of droplets being split into

two or more droplets over a certain period time, or breakup time $t_b(s)$. Here, the droplet diameter is defined as $d_b(m)$ and its volume is $v_b(m^3)$. For the purpose of calculating a breakup rate relevant for a water-in-oil dispersion, it is assumed that $d_b = d_{max}$, where d_{max} is the largest droplet size present in dispersion. Breakup efficiency $\eta_b(-)$ is a fraction of the entire droplet distribution which can successfully complete the breakup processes [13]:

$$g(d_b) = \left(\frac{v_b}{t_b}\right) \eta_b \quad (43)$$

The droplet breakup time $t_b(s)$ is proportional to the droplet size and inversely proportional to the turbulent dissipation rate [13]:

$$t_b = C_2 d_b^{2/3} \bar{\epsilon}^{-1/3} \quad (44)$$

where, C_2 is a dimensionless constant. It is important to notice that the diameter of the breaking droplet d_b (m) is in the range of $l_k < d_b < 0.1D$, where l_k is the Kolmogoroff length scale which is the smallest length scale in turbulence, and D is the pipe diameter.

The breakup efficiency $\eta_b(-)$ is proportional to the fraction of turbulent eddies which have sufficient turbulent kinetic energy $E_t(kg.m^2/s^2)$ to overcome the droplet surface energy $E_s(kg.m^2/s^2)$ and break the droplets [13]:

$$\eta_b = \exp\left(-\frac{E_s}{E_t}\right) \quad (45)$$

The droplet surface energy $E_s(kg.m^2/s^2)$ is proportional to the liquid-liquid interfacial tension $\sigma(N/m)$ and the breaking droplet size $d_b(m)$ [13]:

$$E_s = C_3 \sigma d_b^2 \quad (46)$$

where, C_3 is a dimensionless constant. The eddies kinetic energy $E_t(kgm^2/s^2)$ is proportional to the mean square root of eddy velocity fluctuation $\overline{u'^2}$ (m/s) [33]. The eddies sizes are set identical with the breaking droplet size d_b (m) [33].

$$E_t = C_4 \rho_c d_b^3 \overline{u'^2} \quad (47)$$

$$\overline{u'^2} = C_5 \bar{e}^{2/3} d_b^{2/3} \quad (48)$$

The final expression of the breakup rate $g(d_b)$ (m³/s) becomes [13], [45]:

$$g(d_b) = K_1 d_b^{-2/3} \bar{e}^{1/3} \exp\left(-\frac{K_2 \sigma}{\rho_c d_b^{5/3} \bar{e}^{2/3}}\right) v_b \quad (49)$$

where, $K_1(-)$ and $K_2(-)$ are empirical constants [45]. Based on their experimental data, Coualoglou and Tavlarides found that $K_1 = 0.00487$ and $K_2 = 0.0552$ [13].

2.3.2 Droplet coalescence rate prediction

The specific calculation of coalescence rate is strongly dependent on empirical constants which can vary dramatically from one oil-water system to another. However, it is still worth to roughly quantify the coalescence rate (at least relative to the breakup rate) and determine the coalescence effect on droplet size predictions.

The droplet coalescence is quantified with the coalescence rate Γ (m³/s) [33]. It describes the rate at which two droplets can successfully merge into one. The following physical model has been proposed to describe the mechanisms of coalescence motion. The coalescence rate $\Gamma(d_1, d_2)$ (m³/s) of two droplets d_1 (m) and d_2 (m) is the product of collision rate $H(d_1, d_2)$ (m³/s) and coalescence efficiency $\lambda(d_1, d_2)(-)$, as shown in Equation 50 [33]:

$$\Gamma(d_1, d_2) = H(d_1, d_2) \lambda(d_1, d_2) \quad (50)$$

Here, the droplet sizes are chosen as $d_1 = d_{max}$ and $d_2 = SMD$, SMD is the sauter mean diameter of the droplets in dispersion. The specific calculations of the collision rate and the coalescence efficiency are discussed below.

2.3.2.1 Collision rate

The first term of coalescence rate expression represents the collision rate $H(d_1, d_2)$ (m^3/s) which is the volume of colliding droplets per unit time.

The collision rate, assuming that droplets are not elastic, is the multiplication of the droplet collision area $A_{12}(m^2)$ and droplets relative velocity $u_{rel}(m/s)$ [33].

$$H(d_1, d_2) = A_{12}u_{rel} \quad (51)$$

$$A_{12} = \frac{\pi}{4}(d_1 + d_2)^2 \quad (52)$$

The relative velocity of two colliding droplets $u_{rel}(m/s)$ is proportional to the mean square root of two eddies velocities u_{t1} and $u_{t2}(m/s)$ [33]. The eddies sizes are set to be identical to the droplets sizes $d_1, d_2(m)$, or in this case d_{max} and Sauter mean diameter (SMD)[33]. It is also assumed that large eddies do not cause droplet relative motion and that small eddies do not have sufficient energy to move droplets[33]. The droplet size d (m) is in the range of $l_k < d_{max} < 0.1D$, where, l_k is the Kolmogoroff length scale which is the smallest length scale in turbulence, D is the pipe diameter.

$$u_{rel} = (u_{t1}^2 + u_{t2}^2)^{1/2} \quad (53)$$

$$u_t = C_6(d\bar{\epsilon})^{2/3} \quad (54)$$

The eddy velocity $u_t(m/s)$ is calculated using the turbulent dissipation rate $\bar{\epsilon}$ ($Watt/Kg$), C_6 is a constant. The final equation for the collision rate is shown as [13]:

$$H(d_1, d_2) = C_7 \frac{\pi}{4} (d_1 + d_2)^2 (d_1^{2/3} + d_2^{2/3})^{1/2} \bar{\epsilon}^{1/3} \quad (55)$$

where, C_7 is a constant, $C_7 = 2.17 \times 10^{-4}$ [46]. This model is only used for droplet collision prediction in turbulent dispersed flow and quantifies the collision rate of two droplets in the dispersion.

2.3.2.2 Coalescence efficiency

The second term of the coalescence rate expression is the coalescence efficiency $\lambda(d_1, d_2)(-)$ which is the fraction of droplet collisions leading to droplet coalescence [33]. Two main approaches have been proposed to calculate coalescence efficiency: the energy model and the film drainage model.

2.3.2.2.1 The energy model

The energy model is based on direct observation of droplet coalescence in dispersion and assumes that the coalescence process is instantaneous [47]. This model also assumes that the coalescence efficiency is proportional to collision energy and inversely proportional to interfacial energy [33]. The collision energy is the external turbulent energy applied on droplets which promotes coalescence. The interfacial energy is the droplet surface energy which tends to resist coalescence. The energy model assumes that interfacial energy is proportional to the fluids interfacial tension and that the collision energy is proportional to the volume of droplets and the turbulent dissipation rate [33]. The equation of coalescence efficiency $\lambda(d_1, d_2)(-)$ is [48]:

$$\lambda(d_1, d_2) = \exp \left(-C_8 \frac{E_\sigma}{E_{kin}} \right) \quad (56)$$

$$E_\sigma = \sigma (V_1^{2/3} + V_2^{2/3}) \quad (57)$$

$$E_{kin} = \rho_d \bar{e}^{2/3} (V_1^{11/9} + V_2^{11/9}) \quad (58)$$

where, $E_\sigma(kgm^2/s^2)$ is the droplet interfacial energy, $E_{kin}(kgm^2/s^2)$ is the collision energy, and C_8 is a constant, V_1 and $V_2(m^3)$ are the volumes of two colliding droplets, and $\rho_d(kg/m^3)$ is the density of dispersed water phase. The $\sigma(N/m)$ is the interfacial tension between continues phase and dispersed phase.

2.3.2.2.2 Film drainage model

The film drainage model assumes that coalescence is not an instantaneous process and considers the time needed for the thin film of liquid between two droplets to drain. This model depends on two time scales, drainage time and contact time [33]. The drainage time is the time needed to drain the oil film which is trapped between two droplets [33]. The contact time is the time two droplets spend to interact with each other during the whole coalescence process. Coalescence occurs when the trapped film ruptures. In other words, coalescence will happen if the contact time is larger than the film drainage time [33]. The equation of coalescence efficiency $\lambda(d_1, d_2)(-)$ becomes [13]:

$$\lambda(d_1, d_2) = \exp \left(-C_9 \frac{t_{drainage}}{t_{contact}} \right) \quad (59)$$

The drainage time $t_{drainage}(s)$ calculation assumes that water droplets are deformable with partially mobile interface [38]. The interface mobility represents the behavior of internal recirculation currents within each droplet at the film draining interface [33]. In the case of water droplets coalescing in a continuous oil phase, the recirculation current is opposite to the oil drainage current direction at the interface [33].

$$t_{drainage} = \frac{\pi \mu_d F^{1/2}}{2(2\pi\sigma)^{3/2}} \left(\frac{d_1 d_2}{d_1 + d_2} \right)^{3/2} \left(\frac{1}{h_f} - \frac{1}{h_i} \right) \quad (60)$$

where, $\mu_d(Pa \cdot sec)$ is the dynamic viscosity of dispersed water phase, $\sigma (N/s^{-1})$ is the interfacial tension, $h_i(m)$ is the initial film thickness, and $h_f(m)$ is the critical film thickness where the film rapture and droplet coalesce. Film thicknesses h_i, h_f are obtained from experimental measurements. The compressing force $F(N)$ is an interaction force which drives the draining process during droplets collision [49]. This force is assumed proportional to the turbulent dissipation rate [13]:

$$F \sim \rho_c \bar{\epsilon}^{2/3} (d_1 + d_2)^{2/3} \left(\frac{d_1 d_2}{d_1 + d_2} \right)^2 \quad (61)$$

where, $\rho_c(kg/m^3)$ is the density of continuous oil phase. The contact time $t_{contact} (s)$ is defined as the time interval between the start of film formation and the onset of droplets separation [50]. When droplets move closer and compress the oil film, the droplet surface energy increases preventing coalescence [50]. At the same time, the droplet kinetic energy is also decreasing which tends to promote coalescence [50]. The balance between these two energies is used to express the contact time equation [50]:

$$t_{contact} = \frac{\pi}{4} \left(\frac{\rho_c C_{VM} d_{eq}^3}{3\sigma} \right)^{1/2} \quad (62)$$

where, C_{VM} is the virtual mass coefficient which is found between 0.5 and 0.8 [33].

Film drainage model requires the calculations of time scales which are based on the nature of the coalescence processes. These time scales calculations require specific experimental observations of film thicknesses which can vary dramatically from one oil-water system to another. The energy model simplifies the coalescence processes by assuming film drainage is an immediate process. The energy model can be calculated using flow properties which can be more easily obtained. It represents a simpler and more

practical choice and is used in this study. However, it is important to mention that the determination of coalescence rate through either of the two modes does require prior knowledge of droplet size distribution since the parameter SMD is needed as an input.

2.4 Turbulent dissipation calculation

The turbulent dissipation rate $\bar{\epsilon}$ (kw/kg) is an essential parameter which is involved in the calculation of the turbulent eddies' velocity fluctuations and other key variables. The energy dissipation rate is defined as the rate per unit mass at which the turbulent kinetic energy is absorbed by breaking down the eddies into smaller ones until it is converted into thermal energy by viscous forces. The basic equation is shown below [18]:

$$\bar{\epsilon} = \frac{F_f U}{m} \quad (63)$$

where, $F_f(N)$ is the flow friction force, $U(m/s)$ is the flow velocity, and $m(kg)$ is the fluid mass which flow for certain distance. More practical equations have been developed depending on the flowing conditions (pipe flow, flow through a valve, etc). This is of particular importance in this study since experimental data have been taken in straight pipe flow, flow through a mixing valve and coquette type flow. The different calculation methodologies proposed for each type of flow are presented in the following sections.

In addition, it has been reported that the presence of dispersed water droplets can also influence the behavior of the continuous phase and affect parameters characteristics of turbulent flow, such as the turbulent dissipation rate [58]. This phenomenon is referred as turbulent modulation and is often not included in droplet size or dissipation rate prediction models due to its inherent complexity. An effort is made to characterize the

parameters known to influence turbulent modulation and define operating conditions when its effect on turbulent flow characteristics is significant. In the conditions selected for this study, it was found that turbulent modulation should lead to a lower turbulent dissipation rate than calculated here. However, there is no comprehensive model which can accurately quantify this effect which is consequently omitted in this work. The methodology developed to evaluate the effect of turbulent modulation is shown in Appendix I.

2.4.1 Standard pipe flow

This section considers fluid flow, driven by a positive displacement pump, through a “standard pipe” configuration. The calculation of the turbulent dissipation rate is [7]:

$$\bar{\epsilon} = 2 \frac{f U_c^3}{D} \frac{\rho_m}{\rho_c (1 - \epsilon)} \quad (64)$$

here, the friction factor f in pipe flow is calculated with the Blasius equation: $f = \frac{0.046}{Re^{0.2}}$, Re is the Reynolds number of the flow, $D(m)$ is the pipe internal diameter, ρ_m (kg/m^3) is the water-in-oil mixture density, ρ_c (kg/m^3) is the continuous phase (oil) density, and ϵ (–) is the water cut.

2.4.2 Pipe flow with mixing valve

This section also considers fluid flow, driven by a positive displacement pump, through a “standard pipe” configuration. However, the fluid passes through a mixing valve which purpose is to create a homogeneous dispersion. The friction factor cannot be

defined as easily as for straight pipe flow and, instead, the pressure drop is directly used for the determination of the dissipation rate [7]:

$$\bar{\epsilon} = \frac{\Delta P U_c}{\Delta L \rho_c (1 - \epsilon)} \quad (65)$$

here, the turbulent dissipation rate in pipeline with a mixing valve is calculated in terms of pressure drop, ΔP (pa) over a distance of ΔL (m) between the inlet and outlet of the valve. This expression requires actual experimental measurements of pressure drop across the mixing valve.

2.4.3 Couette flow

This section presents the methodology to determine turbulent energy dissipation rate in Couette type flow. The reason for covering this aspect is that some experimental data are taken in a shear driven flow setup called the doughnut cell. Details of this setup are presented in in Chapter 4.4.

As mentioned earlier, Couette flow is a shear driven flow, typically represented by fluid flow between two parallel plates, one of which is moving relative to the other. In the particular case of the “doughnut cell” and as it is shown in Figure 2, this Couette flow is created between a rotating top circular wall, and a static bottom circular wall.

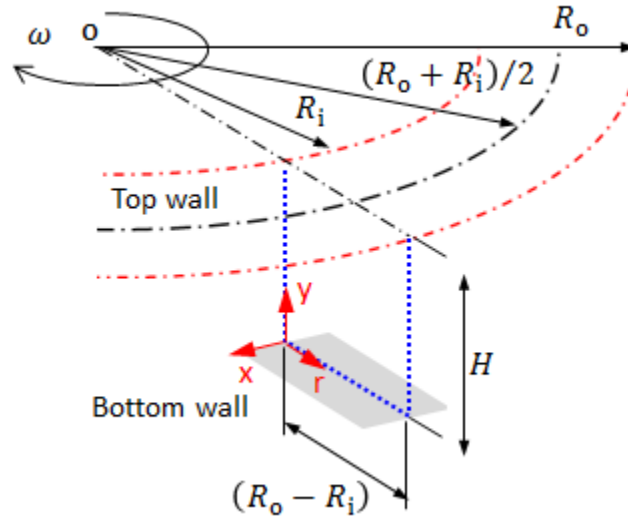


Figure 2. Couette flow between two circular walls [51].

The energy dissipation rate is calculated as:

$$\bar{\epsilon} = \frac{\frac{2}{3}\pi\omega(R_o^3 - R_i^3)\tau_{wt}}{V_c\rho_c} \quad (66)$$

where, $\omega(rad/s)$ is the top wall rotation speed, $R_o(m)$ is the outer diameter of the driving plate, $R_i(m)$ is the inner diameter of the driving plate, $\tau_{wt}(N/m^3)$ is the wall shear stress at the top plate, $V_c(m^3)$ is the volume of the continuous phase, and $\rho_c(kg/m^3)$ is the density of the continuous phase.

$$V_c = \pi(R_o^2 - R_i^2)H(1 - \epsilon) \quad (67)$$

where, $H(m)$ is the distance between top and bottom plates, $\epsilon(-)$ is the water cut.

$$\tau_{wt} = \frac{1}{2}\rho_m f_t U_t^2 \quad (68)$$

where, $\rho_m(kg/m^3)$ is the mixture density, and $U_t(m/s)$ is the mean velocity of the top wall.

$$U_t = \omega \frac{(R_o + R_i)}{2} \quad (69)$$

where, $f_t(-)$ is the friction factor at the top wall, $f_t = 1.0597 Re^{-0.491}$, when $Re \lesssim 15000$, and $f_t = 0.011$, when $Re > 15000$ [52].

2.5 Review of experimental data found in the literature

As explained earlier, a wide range of experimental data is needed to improve the current models and validate them over a wider range of flow conditions. It is consequently essential to collect all the available experimental data in literature in order to develop the best possible foundation for the improvement and validation of the droplet size distribution model. Table 2 presents a summary of literature study which contains a full description of both maximum droplet size and droplet size distribution. Table 2 also displays corresponding pipe flow operating conditions, fluid properties, and references to the original authors of the reported experiments. These data will be used later in Chapter 6 when the model predictions are compared with experimental values.

Table 2. Literature experiments of maximum droplet size and droplet size distribution in turbulent flow.

Authors	Liquid-liquid systems	Pipe diameter (m)	Dispersed phase volume fraction (%)	Turbulent dissipation rate (W/kg)
Karabelas [8]	Water in Kerosene, $\rho_d/\rho_c = 1.25$, $\mu_d/\mu_c = 0.56$, $\sigma = 32.4$ mN/m	0.05	0.2	0.4 to 8.2
Kubie and Gardner [11]	Water in alcohol, $\rho_d/\rho_c = 1.2$, $\mu_d/\mu_c = 0.21$, $\sigma = 4.9$ mN/m Water in acetate, $\rho_d/\rho_c = 1.13$, $\mu_d/\mu_c = 1.43$, $\sigma = 14.5$ mN/m	0.017	0.5 to 2.5	0.8 to 23.4
Hanzevack and Demetriou [10]	Water in Kerosene, $\rho_d/\rho_c = 1.28$, $\mu_d/\mu_c = 0.671$, $\sigma = 32$ mN/m	0.076	0.9 to 4	0.1 to 1.4
Angeli and Hewitt [9]	Water in light oil, $\rho_d/\rho_c = 1.25$, $\mu_d/\mu_c = 0.63$, $\sigma = 17$ mN/m	0.0243	3.4 to 5	0.9 to 3.1
Simmons and Azzopardi [5]	Potassium carbonate solution-in-kerosene, $\rho_d/\rho_c = 1.49$, $\mu_d/\mu_c = 0.97$, $\sigma = 10$ mN/m	0.063	1.2 to 20	0.4 to 5.5
Vielma et al [12]	Water in Tulco Tech 80→ oil, $\rho_d/\rho_c = 1.17$, $\mu_d/\mu_c = 0.071$, $\sigma = 16.4$ mN/m	0.05	1.4 to 8	1.9 to 2.2
Kee [30]	Brine in LVT 200→ oil, $\rho_d/\rho_c = 1.22$, $\mu_d/\mu_c = 0.37$, $\sigma = 40$ mN/m	0.1	1 to 18	0.02 to 0.12

Chapter 3 Motivation and Project Objectives

3.1 Research gaps

The validation of maximum water droplet size and droplet size distribution prediction models over a wide range of conditions is essential to ensure their accuracy, especially in view of the development water wetting predictions. Although a lot of progress has been made in the understanding and modeling of droplet sizes, the following gaps have been identified in the literature:

1. The experimental data available from the literature only cover a limited range of flow conditions and fluid properties.
2. The assumptions made to develop current prediction models of maximum droplet size lead to some level of discrepancies when compared to experimental data and need to be reassessed.
3. The current prediction models of droplet size distribution are empirically generated from experimental data. A mechanistic method is preferred in order to easily extend the range of validity.

3.2 Objectives

The primary objectives of this work are listed below:

1. Collect experimental data of maximum droplet size and droplet size distribution in water-in-oil dispersion for a wide range of flow conditions and fluid properties.
2. Compare experimental data with the current model predictions.
3. Identify gaps in understanding and propose ways forward for the improvement of prediction models.

3.3 Hypotheses

Three main hypotheses are formulated:

1. A single comprehensive model covering maximum droplet size predictions for both dilute and dense dispersion can be developed and validated over a wide range of flow conditions and fluid properties.
2. The assumption that droplet coalescence can be neglected is not valid in all cases and can explain discrepancies between maximum droplet size predictions and experimental measurements.
3. A mechanistic approach can be adopted to predict droplet size distributions based on flow conditions and fluid properties.

This work initially focuses on the collection of experimental data of water droplet sizes in dispersed flow in a wide range of flow conditions. Then, the data is compared to droplet size model predictions in order to identify gaps in the current understanding of the mechanisms and propose a way forward.

3.4 Scope of work

The goal of this section is to present a brief overview of the different types of experimental setups utilized in this research work, of the operational parameters that are varied and of the range of conditions tested.

The experimental work is conducted in three types of laboratory setups: the large scale loop, the large scale loop with mixing device, and a small apparatus.

A large scale loop, 40 m long and 10 cm in diameter, is utilized to generate water-in-oil dispersion in “real world” pipeline flow conditions. Accurate water volume

fractions and flow velocities are controlled using the water and oil pumps. However, running the large scale loop requires large volumes of oil (2650 liters). To decrease the cost of the experiments, a small apparatus “the doughnut cell” is introduced. Only 4 liters of oil are needed in the doughnut cell.

Model oil Isopar V (clear paraffinic saturated hydrocarbon) and DI water (deionized water) are used in the experiments. The interfacial tension between oil and water ranges from 50 dyne/cm (0.05 N/m , Isopar V + water) to 5 dyne/cm (0.005 N/m , Isopar V + water + surfactant). All experiments are operated at room temperature and 1 bar pressure. Two types of droplet size measurement devices are used in this work, a high speed camera and a particle vision microscopy (PVM). The high speed camera is a SONY® NEX 5N camera with $1/4000 \text{ sec}$ shutter speed. This camera is used for standard pipe flow droplet observation at up to 2 m/s flow velocity. High speed camera capture the pictures of water droplet size ranges from 0.2 mm to 10 mm [1]. A more advanced droplet measurement instrument, the PVM with $1/100000 \text{ sec}$ shutter speed, is also used to measure small droplets sizes. The PVM is an improved version of endoscope which is designed with Charge-Coupled Device (CCD) camera and internal laser illumination source to capture high quality droplet pictures [53]. However, the PVM has also limitations since it is enable to measure droplet size larger than $1000 \mu\text{m}$. Consequently, efforts are made to create experimental conditions than decrease the maximum droplet size to the range of PVM measurements ($10\text{-}1000 \mu\text{m}$). The maximum size of droplets can be decreased by increasing the turbulent dissipation rate [18]. Installing a globe valve in the flow loop, upstream of the test section, allows the flow to

achieve a higher pressure loss so that the turbulent dissipation rate range is increased from 0.3-1.1 *Watt/kg* (standard pipe flow) to 122-430 *Watt/kg* (pipe flow with valve) [54].

The PVM is also used for the observation of droplet size in the doughnut cell. However, the doughnut cell flow generates a similar turbulent dissipation range (0.3-7.7 *Watt/kg*) as standard pipe flow where the droplet size is over the PVM measuring limit. The turbulent dissipation rate cannot be enhanced mechanically in the doughnut cell. Since the droplet size is also proportional to the oil-water interfacial tension [18], a surfactant can be added to the water phase to decrease the oil-water interfacial tension from 50 *dyne/cm* (0.05 *N/m*, Isopar V + water) to 5 *dyne/cm* (0.005 *N/m*, Isopar V + water + surfactant) so that maximum droplet sizes in the doughnut cell are always under 1000 μm .

In summary, the constant parameters are:

- Water density: 1005 *kg/m³*
- Oil density: 808 *kg/m³*
- Temperature: 25 °C
- Pressure : 1 bar

The varying parameters for standard pipe flow are:

- Water volume fraction: 1% to 20%
- Water-Oil interfacial tension: 50 *mN/m*
- Turbulent dissipation rate: 0.3 to 1.1 *Watt/kg*

The varying parameters for standard pipe with mixing valve are:

- Water volume fraction: 1% to 15%
- Water-Oil interfacial tension: 50 mN/m
- Turbulent dissipation rate: 122 to 430 $Watt/kg$

The varying parameters for Doughnut cell flow are:

- Water volume fraction: 1% to 20%
- Water-Oil interfacial tension: 5 mN/m
- Turbulent dissipation rate: 0.3 to 7.7 $Watt/kg$

The detailed experimental setup will be discussed in Chapter 4.

Chapter 4 Experiment Setup

This section presents the large and small scale systems that are used to generate water/oil dispersed flow. Droplet size measurement techniques are also discussed.

4.1 Fluids selected for the study

Two immiscible fluids, hydrocarbon and water, are used in this experiments.

- I. The oil phase is comprised of Isopar V[®], a clear paraffinic saturated hydrocarbon model oil manufactured by ExxonMobil Chemical[®] (Density = 808 kg/m^3 at C , oil kinematic viscosity: $13.3 \text{ mm}^2/\text{s}$). This oil provides clear visibility of the entrained water droplets for cameras at low illumination environments.
- II. The water phase is deionized water with 1 wt% sodium chloride representing the aqueous brine produced from an oil well.

4.2 Large scale flow loop

The Institute of Corrosion and Multiphase Technology, Ohio University, houses a large scale low loop with an internal diameter of 10 cm and a length of 40 m, which was used for this study. Figure 3 shows the schematic of this experimental flow loop. It is described in details in the following sections.

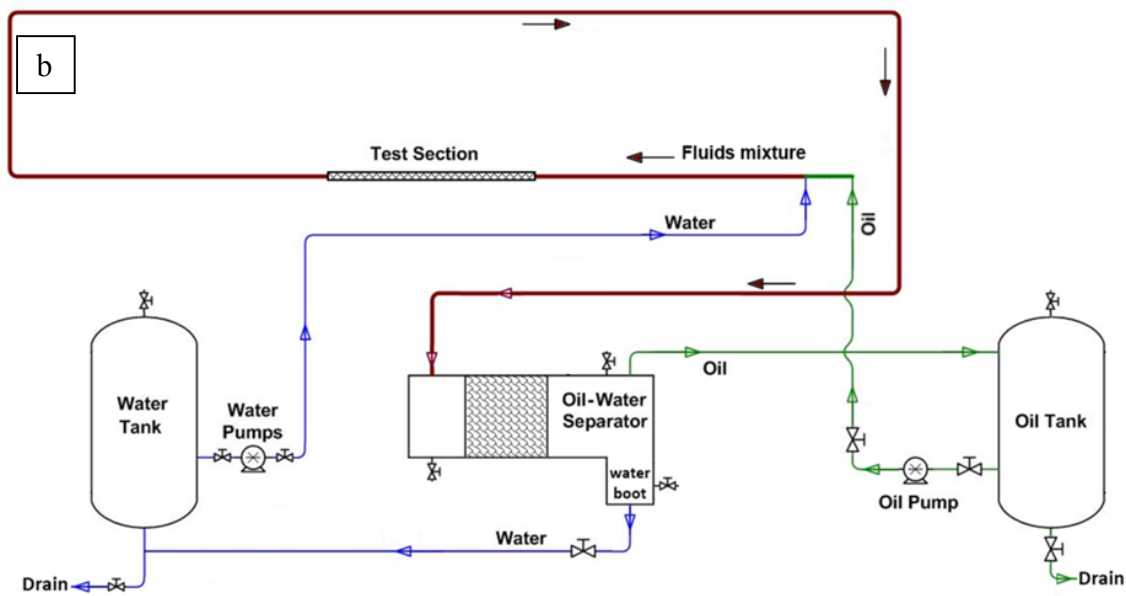
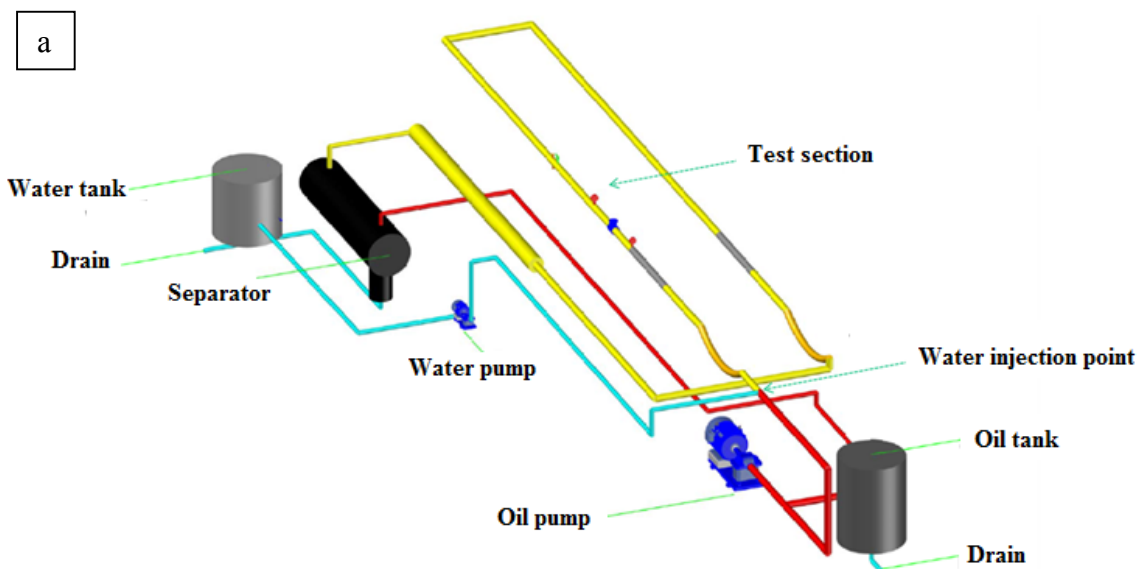


Figure 3. Experimental flow loop (a) 3D drawing (b) Schematic.

4.2.1 Operating procedure

Oil and water are separately pumped from an oil tank and a water tank into the flow loop using positive displacement pumps. These pumps can deliver constant flow rates and consequently ensure constant water cuts at the same time. Both water and oil tanks (Figure 4) have fluid capacities of 1,135 liters. The separator (Figure 5) has a capacity of 1,500 liter. The capacity of the whole system including the separator, tanks, and pipes is 2,650 liters of oil and 1,500 liters of water. The water and oil phases are pumped into the T-section (Figure 6), which mixes them together, before entering the main flow line. The oil-water mixture flows through the pipe loop. After one cycle, the mixture flows to the separator, which separates the water and oil phases. The now separated water flows back to the water tank through the water line. The separated oil flow travels back to the oil tank through oil line for the next cycle. The oil/water separator includes two parts: a coalescer and several enhanced coalescing plates. This coalescer performs a first rough separation of the oil/water mixture. The long gravity-assisted coalescing section with coalescing plates allows complete separation of the two immiscible phases.



Figure 4. (a) Oil tank (b) Water tank.

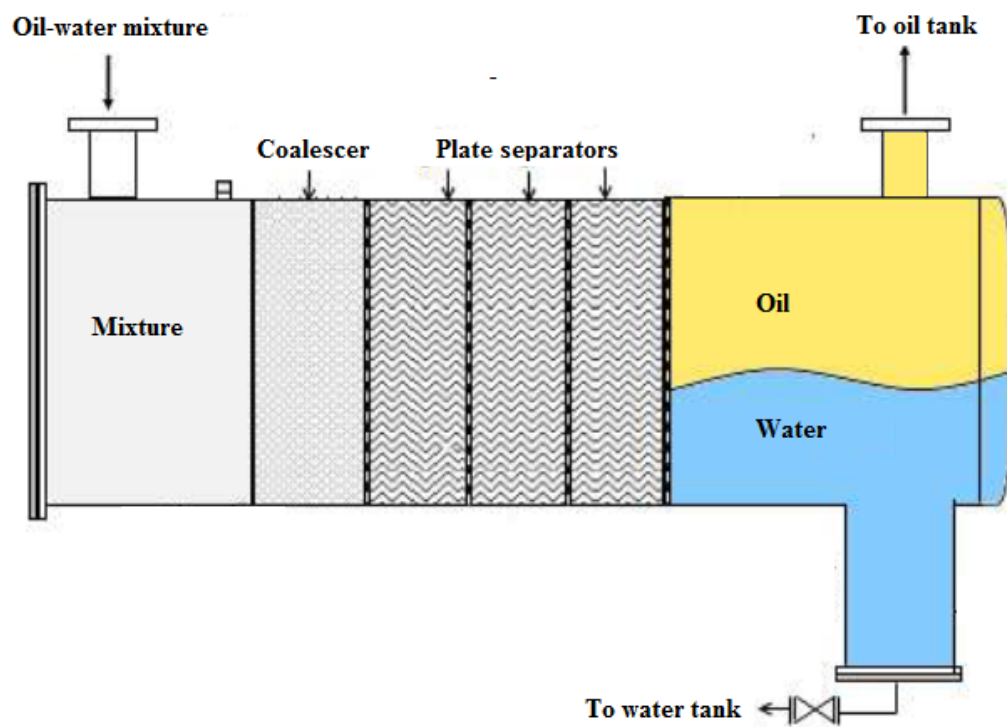


Figure 5. Oil/water Separator.

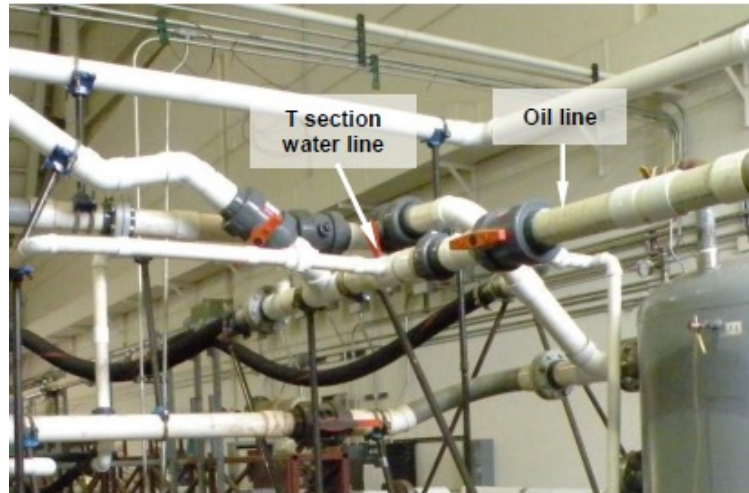


Figure 6. Mixing point of oil and water line (T-section) [30].

4.2.2 Oil and water pumps characteristics

The oil pump is a progressing cavity pump manufactured by Moyno® pump. This pump can provide an output of 14,000 to 120,000 liters per hour. The water pump is a gear pump manufactured by Baldor® electric company. This pump can provide an output of 150 to 5,400 liters per hour. Both oil and water pumps are positive displacement pumps, which can provide a constant flow rate with in $\pm 5\%$ error. The pump flow rate is controlled by operating the frequency of the electrical power input. The experimental oil and water superficial flow velocities are based on the flow rate of water and oil pumps, and the water cut is calculated using Equation 36.

4.2.3 Flow loop test sections

There are two test sections designed for two different types of pipe flow, standard pipe flow (larger droplet sizes) and pipe flow with mixing valve (smaller droplet sizes). For standard pipe flow, a high speed camera is used to take pictures of droplets from the

outside of the pipe. For pipe flow with mixing valve, the PVM is used to take pictures of droplets directly from inside the pipe.

4.2.3.1 Test section for standard pipe flow conditions

The standard pipe flow conditions are representative of turbulent flow at low dissipation rate (0.3 to 1.1 *Watt/kg*) for which the maximum droplet size ranges from 2 *mm* to 10 *mm*. The test section (Figure 7) is a 4 meter long, transparent PVC pipe. An adjustable camera mount is set on a curved bracket which allows the camera to take pictures from the different angles. This camera mount is designed to fit the SONY® NEX 5N camera. Two illumination lights are mounted at top and side of the pipe. The light sources are needed to enhance brightness when the camera is set at the maximum shutter speed which is 1/4000 *sec*.



Figure 7. Transparent PVC pipe test section.

4.2.3.2 Test section for pipe flow with mixing valve conditions

The presence of the mixing valve upstream of the test section generates turbulent flow with high turbulent dissipation rate ($122\text{-}430 \text{ Watt/kg}$), and with maximum droplet sizes ranging from 0.2 mm to 10 mm . The test section (Figure 8) is a 4 meter long, stainless 316 pipe which is designed with a special port for the PVM device. This test section includes a globe valve, ports for pressure gages, and a port for PVM. The PVM has built-in illumination lasers which are perfectly suited for the dark environment inside the pipe.

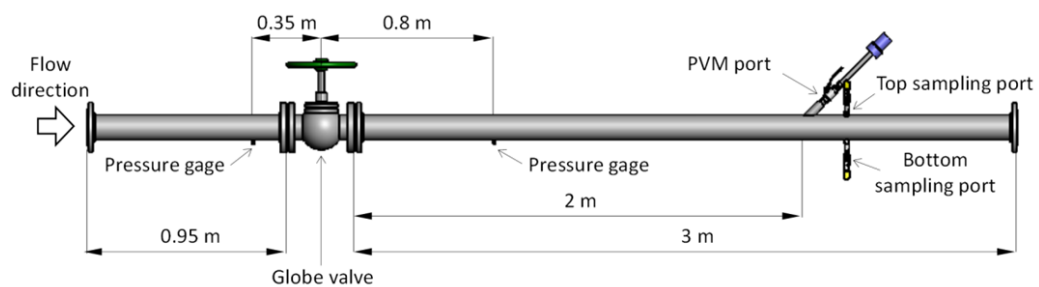


Figure 8. Test section including globe valve and sampling ports (Courtesy of Al Schubert).

The globe valve is an ASME 150 class flanged valve manufactured by Velan®. The picture and schematic of the valve is shown in Figure 9. The dimensions are shown in Table 3.

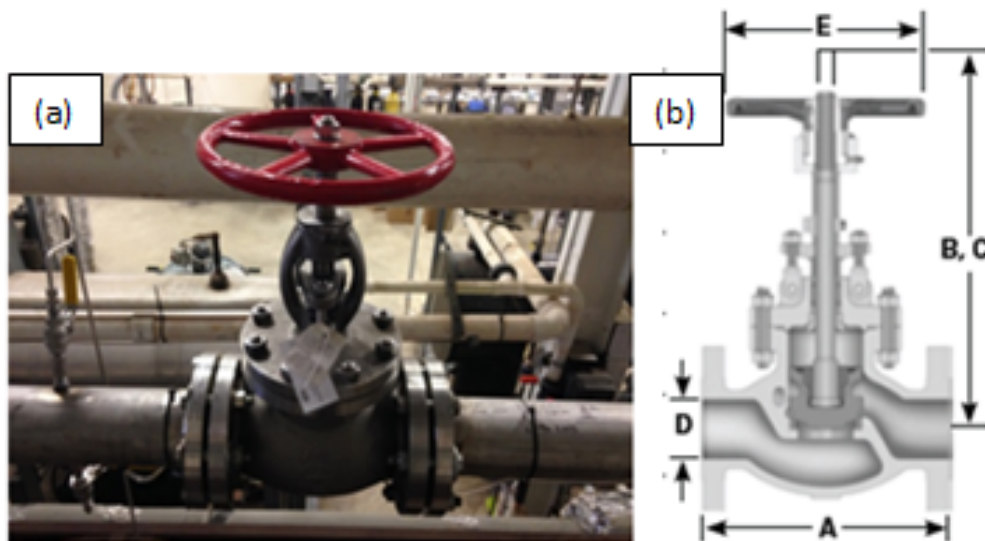


Figure 9. (a)Globe valve at experimental facilities; (b) Schematic of the globe valve.

Table 3. Dimensions of the globe valve provided by the manufacturer.

Dimension	A	B	C	D	E
Length	11.50 inch	20.88 inch	26.18 inch	4.00 inch	14.00 inch
	292 mm	530 mm	665 mm	102 mm	356 mm

The presence of the valve in the flow stream increases the pressure and leads to a higher turbulence level. At this turbulence level, the stratified water-in-oil flow upstream is converted to the fully dispersed water-in-oil flow. The extent of pressure drop created between the valve inlet and outlet depends on the opening of the valve. The pressure drop is measured by two pressure gages located upstream and downstream of the valve. The downstream pressure gage is located at 8 pipe diameters (0.8m) away from the valve outlet. This length is required to avoid low pressure effects after the valve outlet [54]. The pressure measurement values have a maximum uncertainty of $\pm 10\%$.

The PVM device is used to capture *in-situ* droplet sizes. This port is located 20 pipe diameters (2m) away from the valve outlet. This length allows the establishment of a uniform water-in-oil dispersion. The angle of incidence of the port allows the PVM lens to face the flow at 45 degree, which maximizes the quality of the pictures. Two sampling ports are located near the PVM port, on the top and bottom of the pipe, enabling measurement of water contents. Uniform dispersion is verified when the water content measurements from these two sample ports are similar. A Karl Fischer titration instrument and a centrifuge are used to measure the water content of liquid samples. The results showed that all the uniform dispersion experiments have less than a 15% difference between top and bottom water cuts.

4.4 Doughnut cell

The doughnut cell (Figure 10) is a small scale apparatus that creates an environment of turbulent water-in-oil Couette flow (flow between two parallel plates). The oil/water flows between the bottom wall and the top wall under the carousel. An electrical motor rotates the carousel and drive the flow. The droplet sizes are continuously monitored *in-situ* with the PVM. The turbulent dissipation rate, which is proportional to the carousel rotation steep, is calculated between 0.3-7.7 *Watt/kg* which is similar to what is experienced in the standard pipe flow without mixing valve. This situation leads to maximum droplet size out of the range of the PVM. In order to reduce droplet sizes, the oil-water interfacial tension can be controlled by adding a surfactant to the water phase. The surfactant used in this study is a corrosion inhibitor which includes 24 wt% active cocodimethylbenzalkonium chloride in di-ionized water solvent.

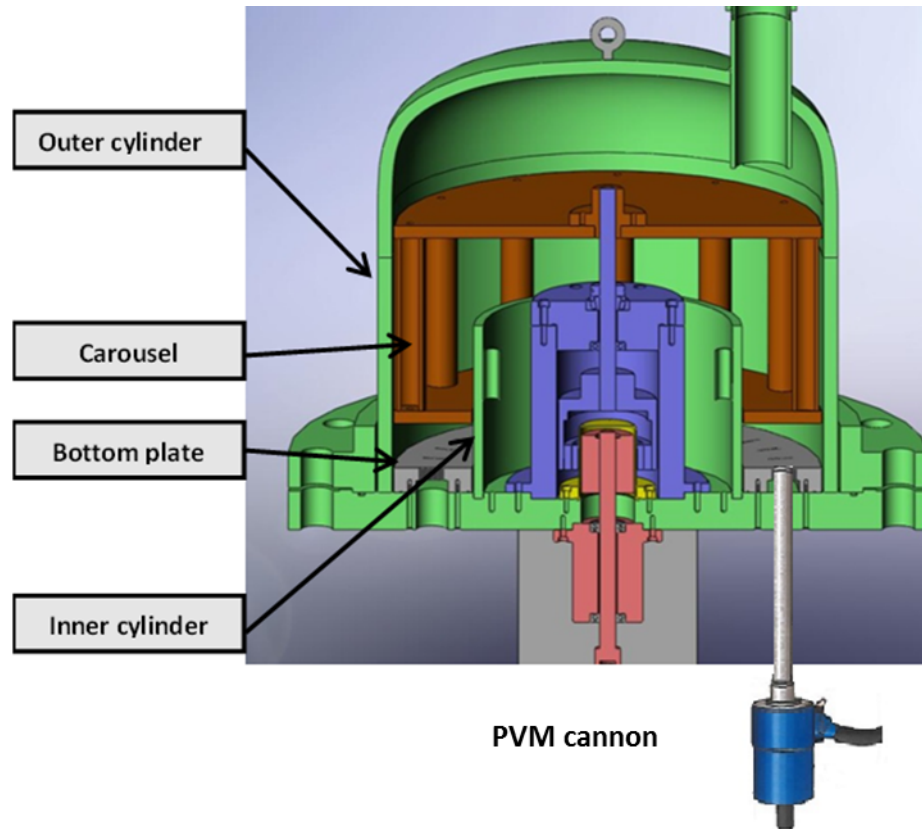


Figure 10. The prototype design of doughnut cell apparatus (Courtesy of Al Schubert).

The PVM lens is mounted at the bottom wall as shown in Figure 11. It is flush-mounted at the bottom wall to minimize flow disturbance. The white hollow cap on top of the lens is needed to reflect the illumination lasers. The cap opening is mounted facing the flow direction.

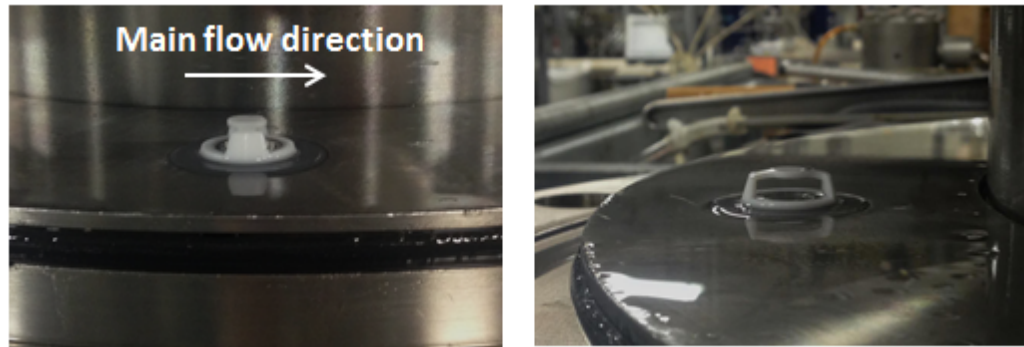


Figure 11. Details of the PVM mounting in doughnut cell

The volume of water and oil is measured prior to injection in the doughnut cell. The turbulent dissipation rate of the flow can be calculated using wall rotation speed. The calculation methodology is discussed in Chapter 2.4.3.

4.5 Analytical methods

This section presents the analytical methods used to measure droplet sizes, water cut, and oil-water interfacial tension and fluid density and viscosity.

4.5.1 Droplet size measurement

The maximum droplet size and droplet size distribution are extracted from the pictures taken either by the high speed camera or by the PVM microscopy.

4.5.1.1 High speed camera pictures

Pictures of the dispersed oil-water droplets obtained for the “standard pipe flow” experiments were captured with the high speed camera aiming at the transparent PVC test section. At least ten pictures are taken per condition. The time elapsed between each picture is ten seconds. A typical picture comprises a rectangular view of the whole pipe

diameter of 0.1 m height and about three pipe diameters (0.3 m) width. A typical example of a captured image is shown at Figure 12.

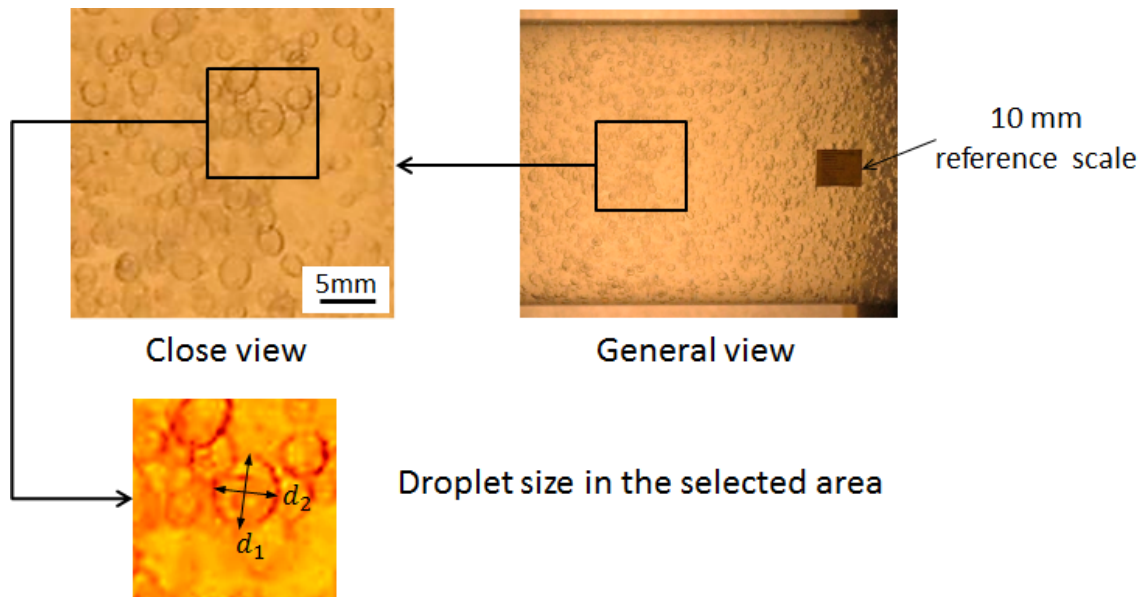


Figure 12. Sample picture of droplet in standard pipe flow

Pictures of droplets display an optical distortion due to the curvature of the transparent pipe. The correction of this optical distortion is made using plastic balls of calibrated sizes. The measurements of the maximum droplet size and droplet size distribution are performed using the concept of the mean diameter ($d_{\text{mean}} = \sqrt{d_1 d_2}$). All the droplet size results are processed using the ImageJ® software. Ten pictures are treated per condition. At least 600 droplet sizes per condition are measured for the establishment of each droplet size distribution. The analysis shows that the mean particle size d_{mean} (mm) is slightly affected by the pipe curvature (as much as -8% to +5% measurement error).

4.5.1.2 PVM pictures

This section describes the analysis of pictures of droplets obtained with the PVM (pipe flow with valve and doughnut cell experiments). The maximum droplet size and droplet size distribution results come from the analysis of 500 pictures per condition. The time elapsed between each picture is one second. The picture is a rectangular view of 1360×1097 pixels with a density of $1.24 \text{ pixels}/\mu\text{m}$. An example of typical picture is shown in Figure 13.

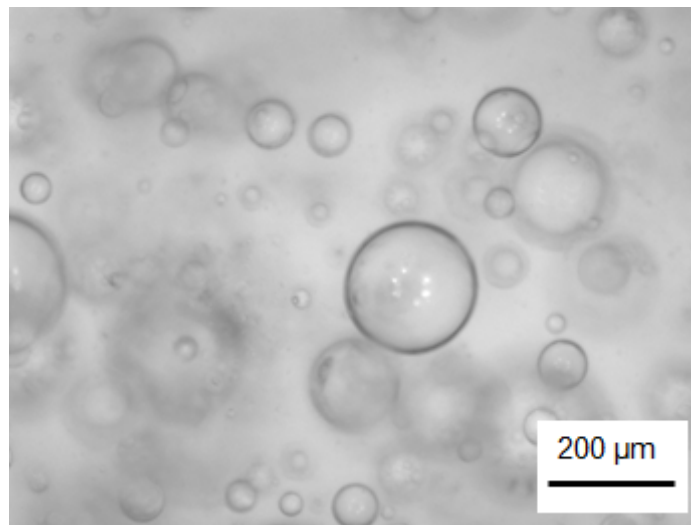


Figure 13. Sample picture of droplets

All maximum droplet size measurements are processed using the ImageJ® software by finding the largest droplet in 500 pictures per condition. As Figure 14 shows, the droplet size distribution result is digitally processed from 500 pictures using the following procedure: band-pass filtering, contrast enhancement, droplet contour identification, droplet counting, and size measurement.

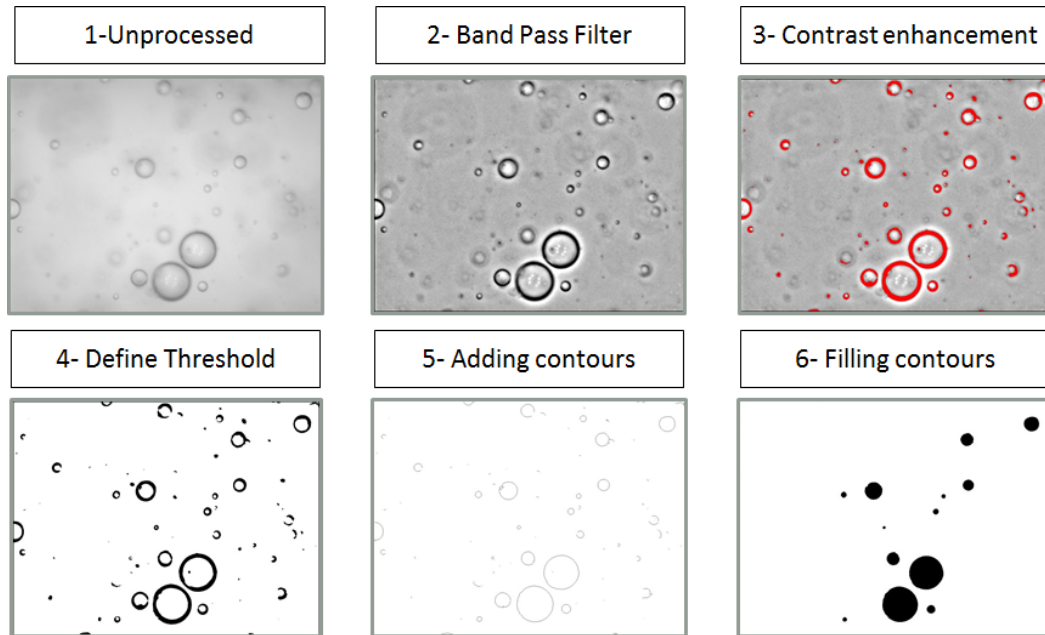


Figure 14. Digital image processing

At least 10,000 droplet sizes are digitally measured per condition for each droplet size distribution. The pictures are also double-checked by manual inspection to ensure the accuracy of digital measurements.

4.5.2 Water cut measurement

The water cut is measured by analyzing liquid samples from the standard pipe with valve configuration experiments. Fluid samples are taken from the sampling ports near the PVM port. The samples water cut are measured by a centrifuge made by L-K industry®. This method is fast but can lack accuracy. All the samples are also accurately checked using the Karl fischer moisture titrator, shown in Figure 15, which is manufactured by Kyoto Electronics®. This instrument is based on Karl Fischer reaction and analytical technique to measure the water volume fraction in liquids [55].



Figure 15. Karl Fischer instrument for measuring water content of liquid mixtures.

As mentioned earlier, experimental results showed that all the uniform dispersion experiments have less than a $\pm 15\%$ difference between top and bottom water cuts.

This sampling method is not applied when a uniform water-in-oil dispersion is not expected, which is the case for the “standard pipe” and “doughnut cell” experiments. For the “standard pipe” experiments, the water cut is calculated using the experimental oil and water flow rates, as shown in Equation 36. For the “doughnut cell” experiments, the water cut is measured prior to injection into the cell using graduated cylinders.

4.5.3 Water-oil interfacial tension measurement

The interfacial tension between oil and water is measured using the DuNouy Tensiometer, shown in Figure 16, which is manufactured by CSC scientific company.

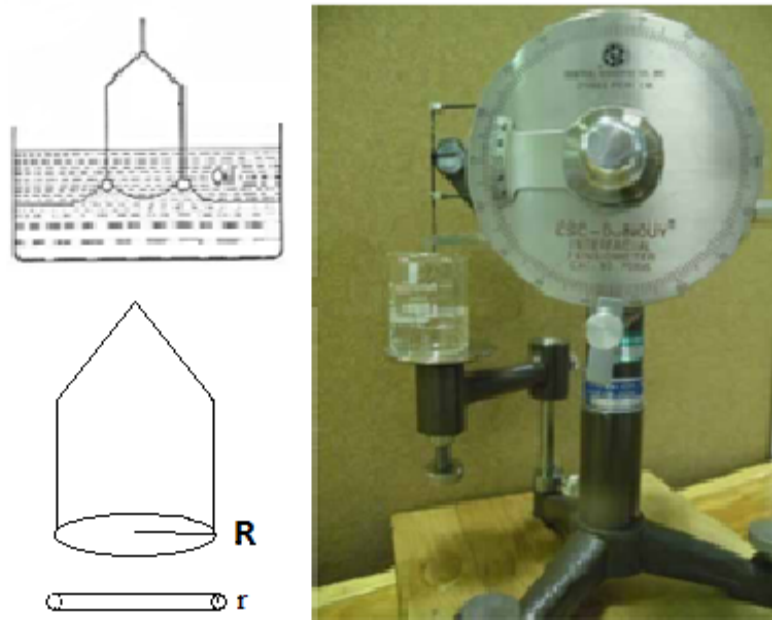


Figure 16. Tensiometer for measuring interfacial tension (Courtesy of K. E. Kee).

A platinum-iridium ring is submersed in the test oil and is pulled upward through the oil-water interface layer until the liquid film ruptures. At the rupture point, the pulling force F can be determined. The interfacial tension is presented as:

$$\sigma = \beta \frac{F}{4\pi R} \quad (70)$$

Where, σ (dyn/cm) is the interfacial tension, β (-) is a correction factor and R (m) is the radius of the platinum-iridium ring. The Zuidema-Waters Correction Factor β (Equation 71) is suggested by the instruction manual for the calculation of interfacial tension [56].

$$\beta = 0.725 + \sqrt{\frac{1.452 P}{C^2(\rho_D - \rho_d)} + 0.04534} - \frac{1.679}{\frac{R}{r}} \quad (71)$$

Where, $P(\text{dyn/cm})$ is the dial reading when the film ruptures, $C(\text{cm})$ is the mean circumference of ring, $\frac{R}{r}$ is the ratio of ring radius with wire radius, $\rho_D(\text{g/cm}^3)$ is the density of heavier phase i.e. water, and $\rho_a(\text{g/cm}^3)$ is the density of lighter phase i.e. oil. The C and $\frac{R}{r}$ of the ring is provided by manufacture.

Chapter 5 Test Matrix

The test matrix for the “standard pipe flow”, “pipe flow with mixing valve” and “doughnut cell experiments are shown in Table 4, Table 5 and Table 6 respectively.

Table 4. Test matrix for standard pipe flow.

Oil Type	Isopar V
Water type	Deionized water
Oil-water interfacial tension	50 mN/m (25 °C)
Water volume fraction	1to 10 %
Turbulent dissipation rate	0.3 to 1.1 <i>Watt/kg</i>
Temperature	25 °C
Droplet size measurement	High speed camera
Inclination	Horizontal and Vertical

Table 5. Test matrix for pipe flow with mixing valve.

Oil Type	Isopar V
Water type	Deionized water
Oil-water interfacial tension	50 mN/m (25 °C)
Water volume fraction	1to 15%
Turbulent dissipation rate	122-430 <i>Watt/kg</i>
Temperature	25 °C
Droplet size measurement	PVM
Inclination	Horizontal

Table 6. Test matrix for small scale doughnut cell test.

Oil Type	Isopar V
Water type	Deionized water + inhibitors
Oil-water interfacial tension	5 mN/m (25 °C)
Water volume fraction	5,10, 20%
Rotating speed	78 to 206 RPMs
Oil-water mixture velocity	1.4, 2, 2.5,3.1,3.7 m/s
Turbulent dissipation rate	0.3 to 7.7 <i>Watt/kg</i>
Temperature	25 °C
Droplet size measurement	PVM

Chapter 6 Experimental Results and Discussion

This chapter presents the experimental data obtained in the large scale flow loop (with or without mixing valve) and the doughnut cell. It is divided into two main parts: maximum droplet size and droplet size distribution. Experimental droplet size data are directly compared with model predictions and the effects of coalescence and other parameters are discussed. The influence of turbulent dissipation rate and water cut on the droplet size distribution is also presented, shading some light on the validity of the fitting correlations.

6.1 Maximum droplet size results

Experimental maximum droplet sizes are obtained from three flow systems: horizontal loop equipped with globe valve, standard horizontal/vertical loop, and doughnut cell apparatus. These results are treated separately for clarity reasons and since distinct differences in the data analysis could be observed:

- Considering the standard pipe with mixing valve, data are representative of a homogeneous water-in-oil dispersion with high turbulent dissipation rates.
- Considering the doughnut cell, a homogeneous water-in-oil dispersion is also created although the turbulent dissipation rates are significantly lower. This is achieved by using surfactants which prevents significant coalescence.
- Considering the standard pipe flow, the dispersion is not as homogeneous and significant water cut gradients could be observed in some cases. This leads to important differences compared to predicted results.

In each section, the influence of water cut and turbulent dissipation rate are discussed and the experimental results are compared with Hinze and Brauner model predictions. Issues related to uncertainty and repeatability of the measurements related to droplet size, turbulent dissipation rate, or water cut are discussed in depth in Appendix III. The errors in the measurements are not explicitly displayed on the following graphs in an effort to maintain the results clarity.

Finally, an updated model, labelled the “ICMT model”, is proposed and validated over a wide range of data coming from both this present study and the literature. Remaining discrepancies between experiments results and model predictions are highlighted. The influence of coalescence is then presented as the main reason for these discrepancies.

6.1.1 Summary of results obtained in a standard pipe with mixing valve

This section presents experimental maximum droplet sizes obtained in the standard pipe with mixing valve configuration. In this condition, a high turbulent dissipation rate is experienced, calculated at 122 to 430 *Watt/kg*. The oil-water interfacial tension is 50 mN/m, and the water cut ranges from 1% to 15%.

The influence of two main operating parameters, turbulent energy dissipation rate and water cut, is treated in turn. Experimental results are also compared to Hinze’s and Brauner’s model predictions.

6.1.1.1 Effect of turbulent dissipation rates

Figure 17 shows the measured maximum droplet size data in relation to the energy dissipation rate at 5% average water cut. The energy dissipation rate varies from

122-430 *Watt/kg*. The maximum droplet sizes tend to decrease as the energy dissipation rate increases. A least square fitting is performed on the experimental data using power law, a slope of -0.34 is found. This slope value is close to the Hinze theoretical value -0.4 (Equation 33). This confirms that droplet breakup is the dominant mechanism determining the maximum droplet size and that coalescence can indeed be neglected in this case. Figure 17 also shows that the maximum droplet size d_{\max} (μm) is in the range of $l_k < d_{\max} < 0.1D$, where, $l_k(m)$ is the Kolmogoroff length scale which is the smallest valid turbulent eddies' length scale in turbulence, one tenth of pipe diameter $0.1D = 1\text{cm}$ is the largest valid length scale of turbulent eddies in turbulence.

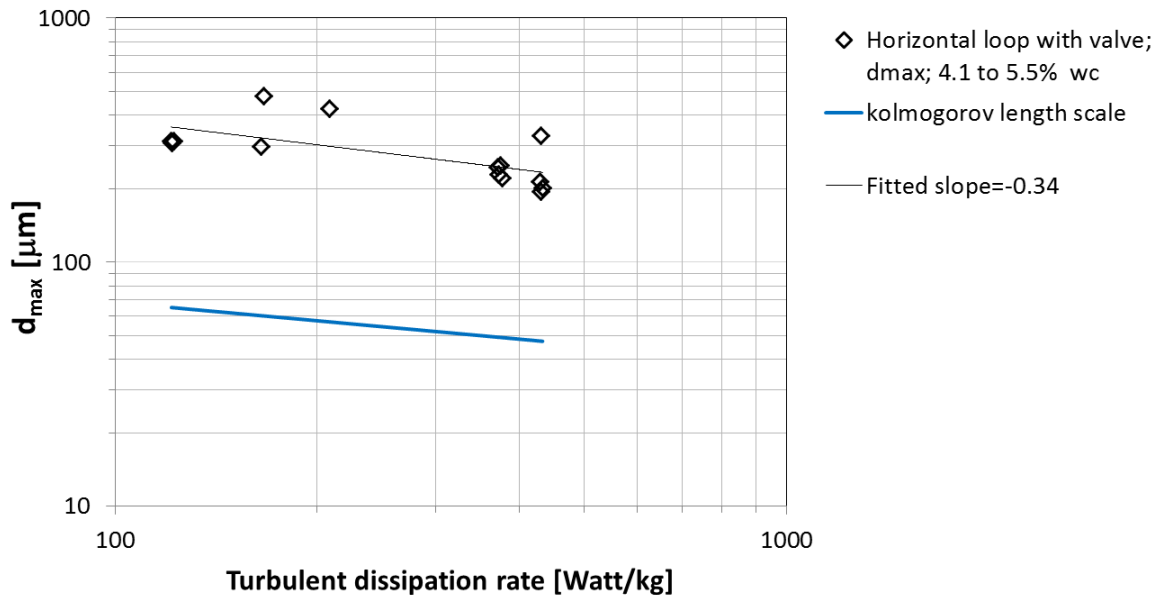


Figure 17. Measured maximum droplet size in relation to the energy dissipation rate at 5% average water cut - Standard pipe with mixing valve configuration.

The comparison between the measured maximum droplet size and the Hinze/Brauner model predictions in relation to the energy dissipation rate at 4.8%

average water cut is shown in Figure 18. It should be stressed that Hinze's model does not depend directly on the water cut while Brauner's model does. Consequently, while Hinze's model predictions are presented as a single line, results obtained from Brauner's correlations can take into account the slight variation in experimental water cut (4.1 to 5.5%) and are shown with three parallel lines corresponding to the minimum, average and maximum water cut. As expected, Hinze's model predicts relatively accurately d_{\max} for dilute dispersion (water cut < 5%) while Brauner's model tends to under-predict d_{\max} . This is not surprising since Brauner's model is only valid for dense dispersion (water cut > 5%).

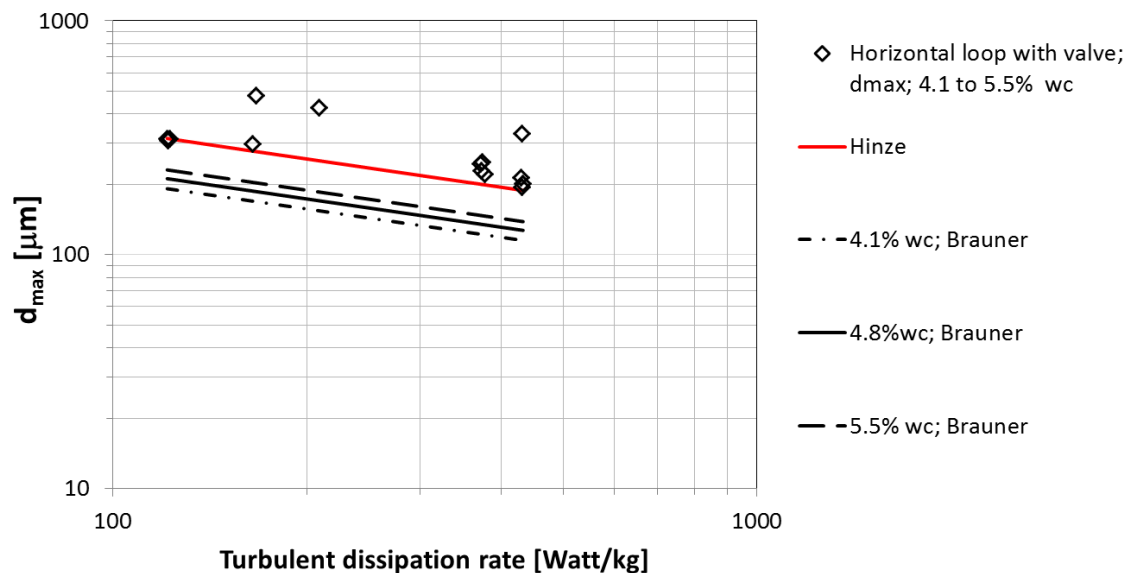


Figure 18. Comparison between measured maximum droplet size and the Hinze/Brauner model predictions in relation to the energy dissipation rate at 5% average water cut. Standard pipe with mixing valve configuration.

The measured maximum droplet size in relation to the energy dissipation rate at 10% average water cut is shown in Figure 19. The energy dissipation rate varies from

122-220 *Watt/kg*. Although data points are scattered, it is found that the maximum droplet size tends to decrease as the energy dissipation rate increases. A least square fitting is performed on the experimental data using power law, a slope of -0.35 is found. Once again, this slope value is close to the Hinze theoretical value -0.4 (Equation 33) which tends to identify droplet breakup as the dominant mechanism. Figure 19 also shows that the maximum droplet size d_{\max} (μm) is in the range of $l_k < d_{\max} < 0.1D$.

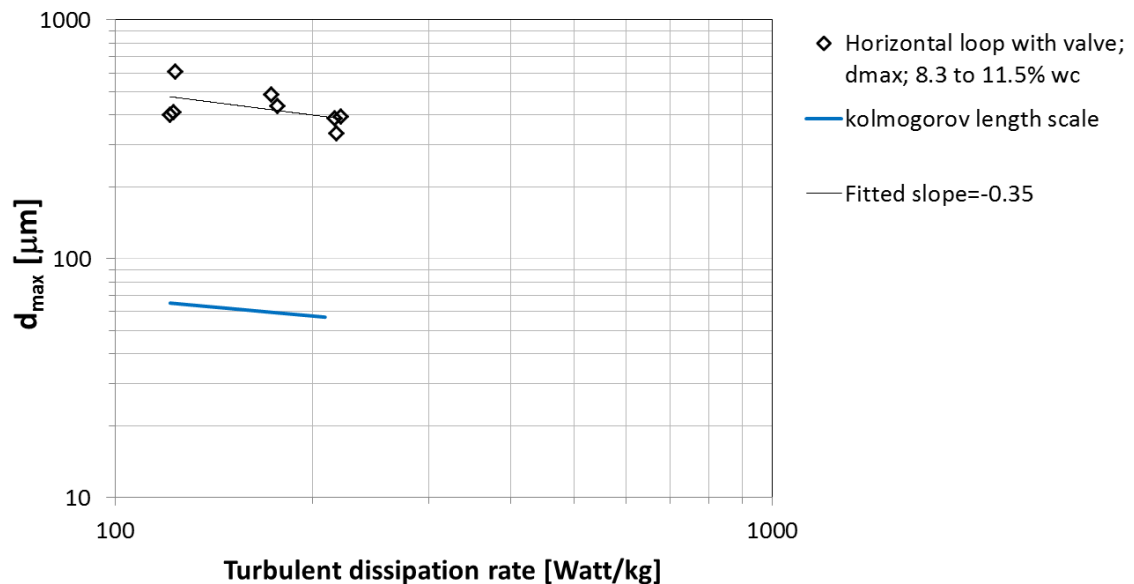


Figure 19. Measured maximum droplet size in relation to the energy dissipation rate at 10% average water cut - Standard pipe with mixing valve configuration.

The comparison between the measured maximum droplet size and the Hinze/Brauner model predictions in relation to the energy dissipation rate at 10% average water cut is shown in Figure 20. In these conditions, Brauner's model gives a better prediction of d_{\max} than Hinze's model. This is not surprising since the Hinze model is only valid for dilute dispersion (water cut $< 5\%$).

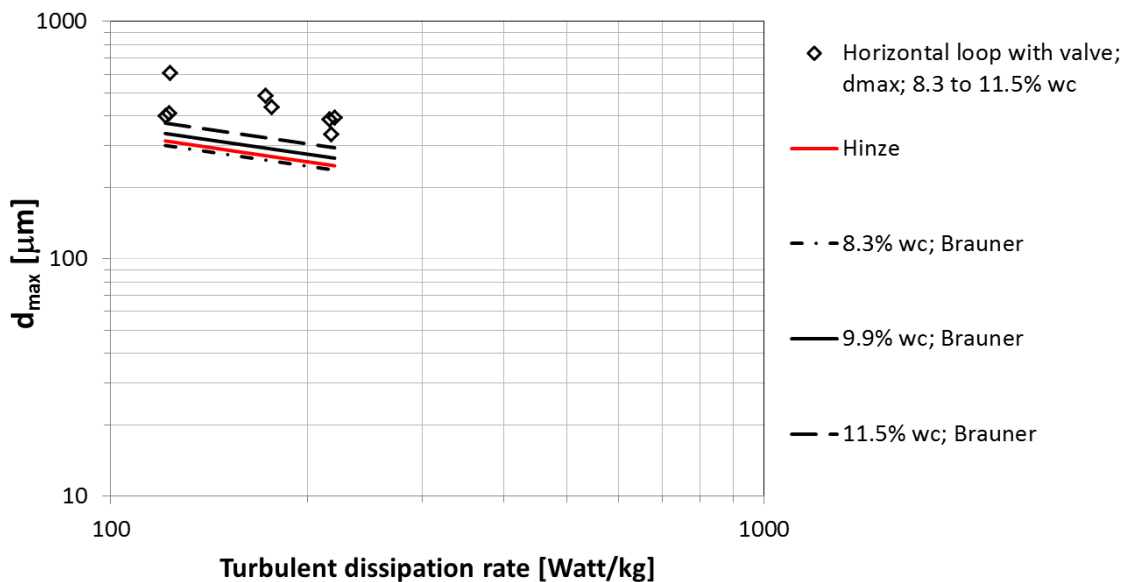


Figure 20. Comparison between measured maximum droplet size and the Hinze/Brauner model predictions in relation to the energy dissipation rate at 10% average water cut - Standard pipe with mixing valve configuration.

6.1.1.2 Effect of water cut

This section presents the same experimental results as previously shown but now the effect of water cut is highlighted. Figure 21 shows the measured maximum droplet size in relation to the water cut over the entire range of turbulent dissipation rate tested (122 and 220 Watt/kg). It is found that the maximum droplet sizes tend to increase as the water cut increases, irrespective of the dissipation rate.

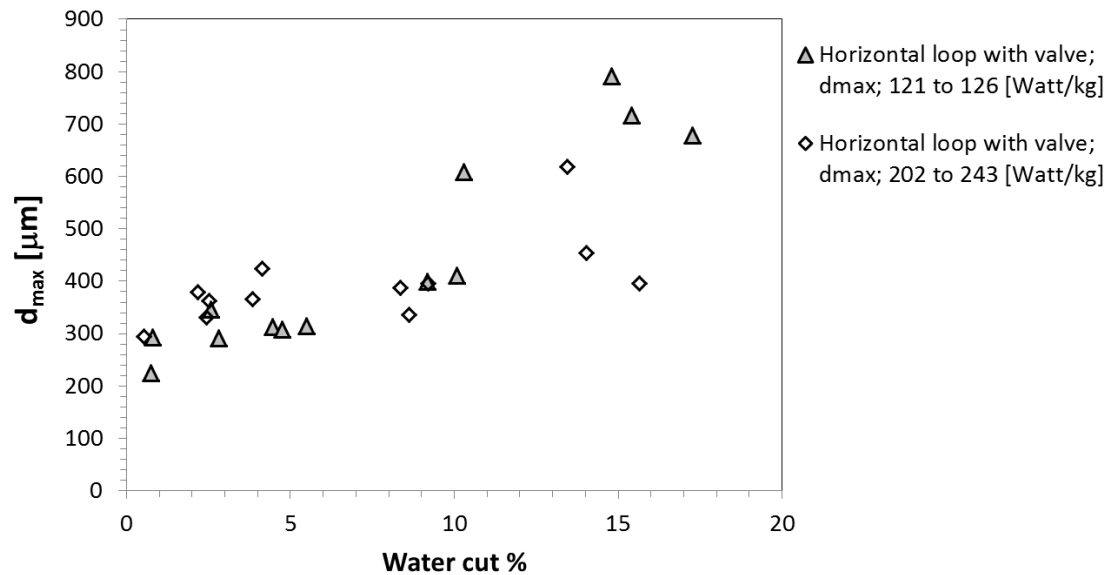


Figure 21. Measured maximum droplet size in relation to the water cut at 122 and 220 Watt/kg average turbulent dissipation rate - Standard pipe with mixing valve configuration.

Figure 22 shows the comparison between the measured maximum droplet size and the Hinze/Brauner model predictions in relation to the water cut at 122 Watt/kg average turbulent dissipation rates. Hinze's model predicts d_{max} well in dilute dispersion conditions ($0 < \text{water cut} < 5\%$) while Brauner's model slightly under predicts d_{max} at water cut range: $5\% < \text{water cut} < 10\%$. Larger prediction errors occur at high water cut range: $10\% < \text{water cut} < 20\%$.

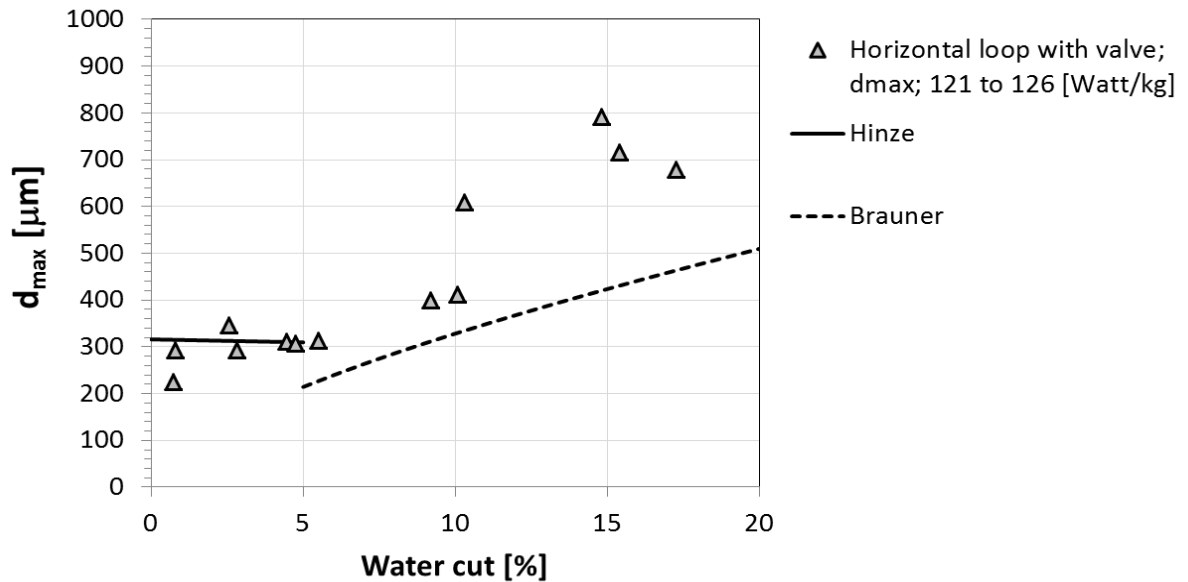


Figure 22. Comparison between the measured maximum droplet size and the Hinze/Brauner model predictions in relation to the water cut at average turbulent dissipation rate 122 Watt/kg - Standard pipe with mixing valve configuration.

Similarly, the comparison between the measured maximum droplet size and the Hinze/Brauner model predictions in relation to the water cut at higher average turbulent dissipation rates (220 Watt/kg) is shown in Figure 23. Hinze model tends to under predict the d_{max} in dilute dispersion conditions ($0 < \text{water cut} < 5\%$). Brauner model under predicts the d_{max} at dense dispersion conditions ($\text{water cut} > 5\%$). However, in both cases (dissipation rates of 122 and 220 Watt/kg), the trend seems to be correct.

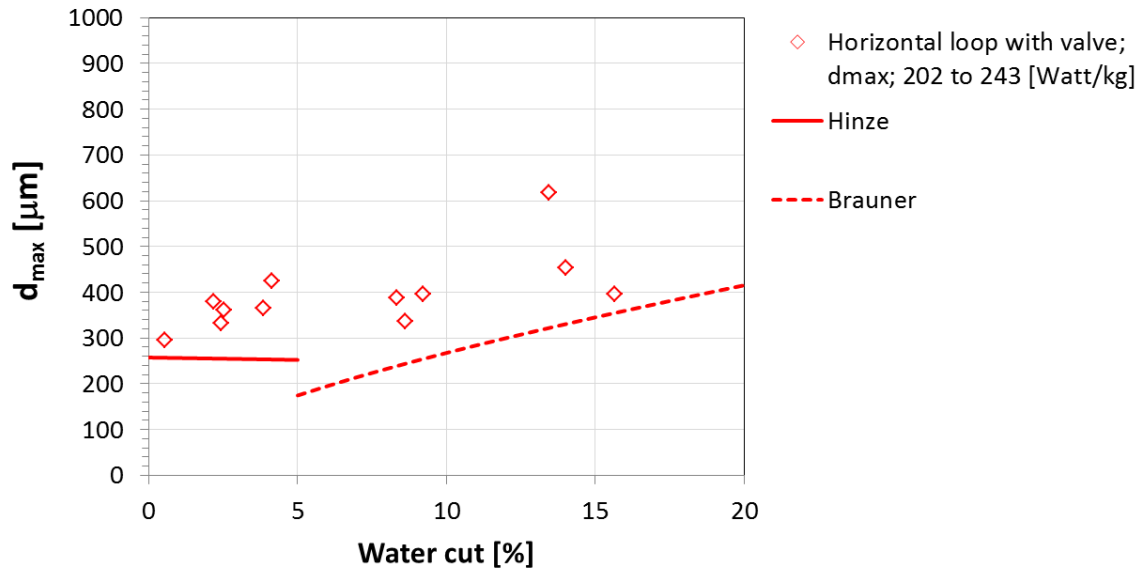


Figure 23. Comparison between the measured maximum droplet size and the Hinze/Brauner model predictions in relation to the water cut at average turbulent dissipation rate 220 Watt/kg - Standard pipe with mixing valve configuration.

Finally, Figure 24 shows the comparison between the measured maximum droplet size and Hinze's and Brauner's model predictions. Hinze model is used to predict d_{max} in dilute dispersion (water cut $< 5\%$). Brauner model is used to predict d_{max} in dense dispersion (water cut $> 5\%$). This plot shows 50% prediction points are out of the $\pm 30\%$ error bonds. The fit appears to be average at best and improvements in the modeling approach are proposed in Chapter 6.1.4.

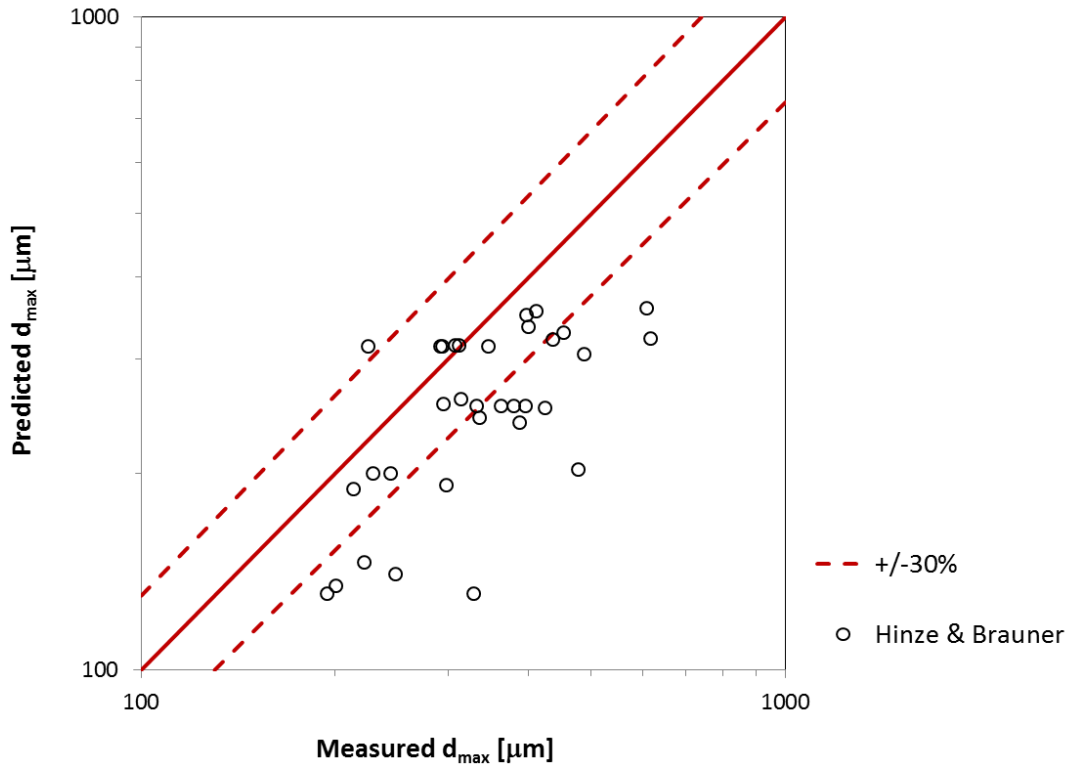


Figure 24. Comparison between measured horizontal loop with valve maximum droplet size and Hinze/Brauner model predictions - Standard pipe with mixing valve configuration.

6.1.2 Summary of results obtained in the doughnut cell

The type of flow characteristic of the Doughnut cell system is Couette flow (flow between two parallel plates, one stagnant and one moving). The conditions tested display turbulent dissipation rates in the range: 0.3 to 7.7 *Watt/kg*, an oil-water interfacial tension of 5 mN/m, and water cuts in the range of 5%, 10%, and 20%. As mentioned earlier, a surfactant is used to reduce the oil-water surface tension in order to decrease the droplet sizes. Although artificial, this change is taken into account on the predictions since surface tension is a model input.

As for the previous section, the influence of two main operating parameters, turbulent energy dissipation rate and water cut, is treated in turn. Experimental results are also compared to Hinze's and Brauner's model predictions.

6.1.2.1 Effect of turbulent dissipation rates

The measured maximum droplet size in relation to the energy dissipation rate at 5% average water cut is shown in Figure 25. The energy dissipation rate varies from 0.3 to 7 *Watt/kg*. As expected, the maximum droplet sizes tend to decrease as the energy dissipation rate increases. A least square fitting is performed on the experimental data using power law, a slope of -0.32 is found. This slope value is once again close to the Hinze theoretical value -0.4 (Equation 33) confirming that droplet breakup is still the dominant mechanism for maximum droplet size determination. Figure 25 also shows that the maximum droplet size d_{\max} (μm) is in the range of $l_k < d_{\max} < l_e$, where, l_k is the Kolmogoroff length scale which is the smallest valid turbulent eddies' length scale in turbulence, $l_e = 0.875\text{cm}$ is the largest valid length scale of turbulent eddies in turbulent flow.

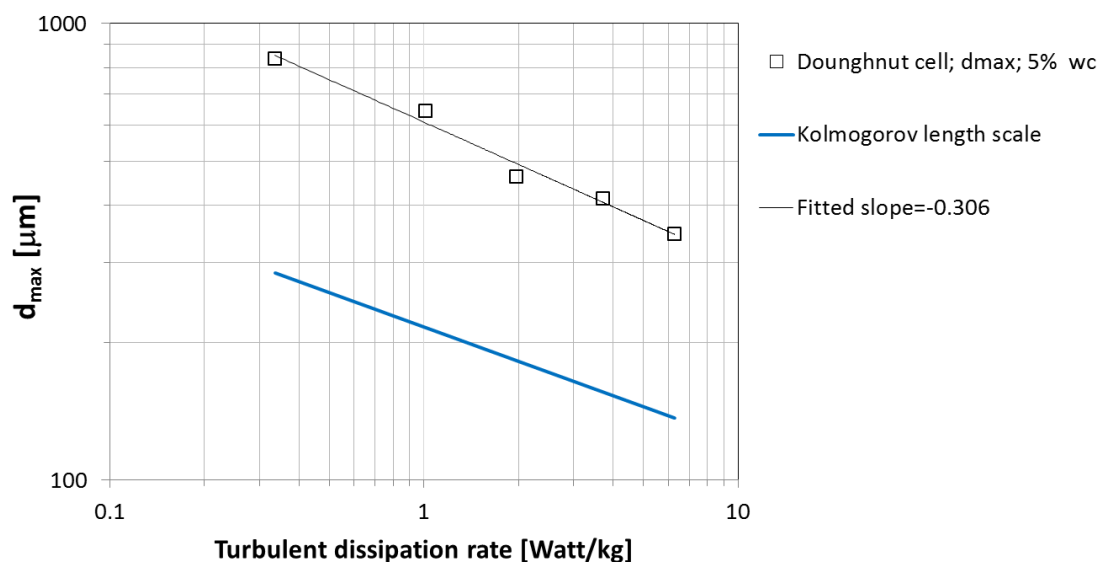


Figure 25. Measured maximum droplet size in relation to the energy dissipation rate at 5% average water cut - Doughnut cell configuration.

Figure 26 is the comparison between the measured maximum droplet size and the Hinze/Brauner model predictions in relation to the energy dissipation rate at 5% average water cut in doughnut cell system. Hinze's model predicts the d_{max} well for dilute dispersion (water cut < 5%) while Brauner's model tends to under predict the d_{max} which is not surprising since the Brauner model is only valid for dense dispersion (water cut > 5%).

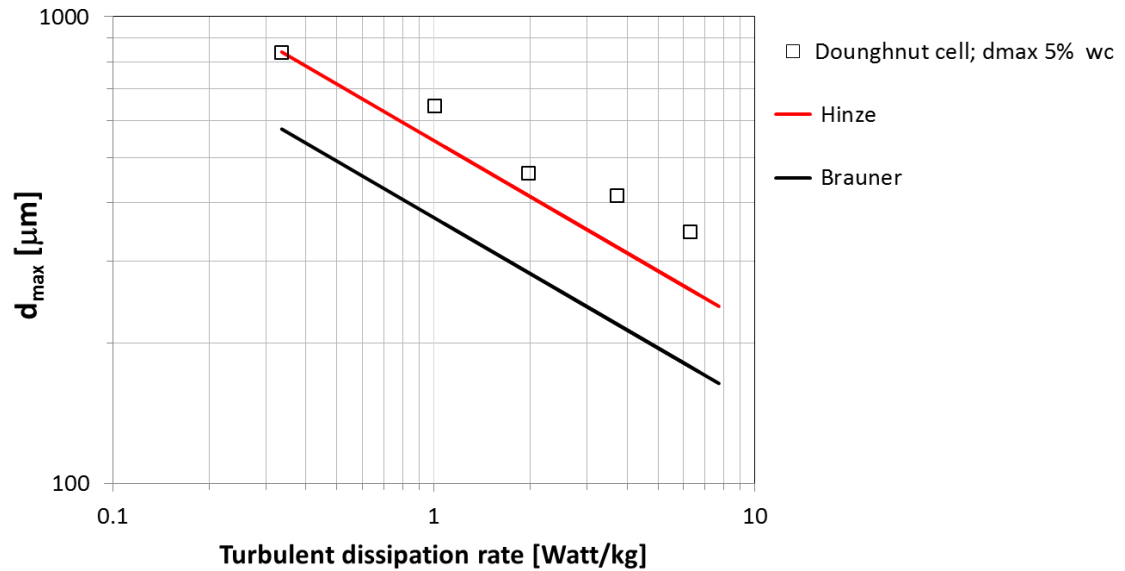


Figure 26. Comparison between the measured maximum droplet size and the Hinze/Brauner model predictions in relation to the energy dissipation rate at 5% average water cut - Doughnut cell configuration.

The measured maximum droplet size in relation to the energy dissipation rate at 10% average water cut is shown in Figure 27. The energy dissipation rate varies from 1.1-6.7 *Watt/kg*. The maximum droplet size tends to decrease as the energy dissipation rate increases. A least square fitting is performed on the experimental data using power law, a slope of -0.36 is found which is close to the Hinze theoretical value -0.4 (Equation 33). Droplet breakup is still the dominant mechanism. Figure 27 also shows that the maximum droplet size d_{max} (μm) is in the range of $l_k < d_{max} < l_e$.

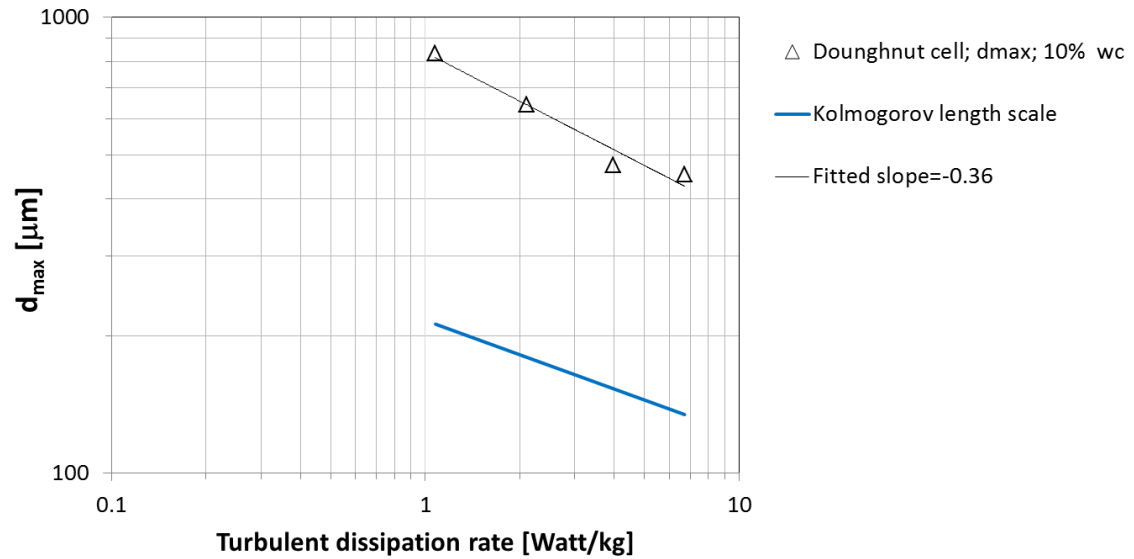


Figure 27. Measured maximum droplet size in relation to the energy dissipation rate at 10% average water cut - Doughnut cell configuration.

The comparison between the measured maximum droplet size and the Hinze/Brauner model predictions in relation to the energy dissipation rate at 10% average water cut in horizontal loop with valve is shown in Figure 28. Both Hinze's and Brauner's model under predict the d_{max} . Brauner's model predictions are naturally better than Hinze's model since Brauner's model is valid for dense dispersion (water cut > 5%) and Hinze's model is only valid for dilute dispersion (water cut < 5%).

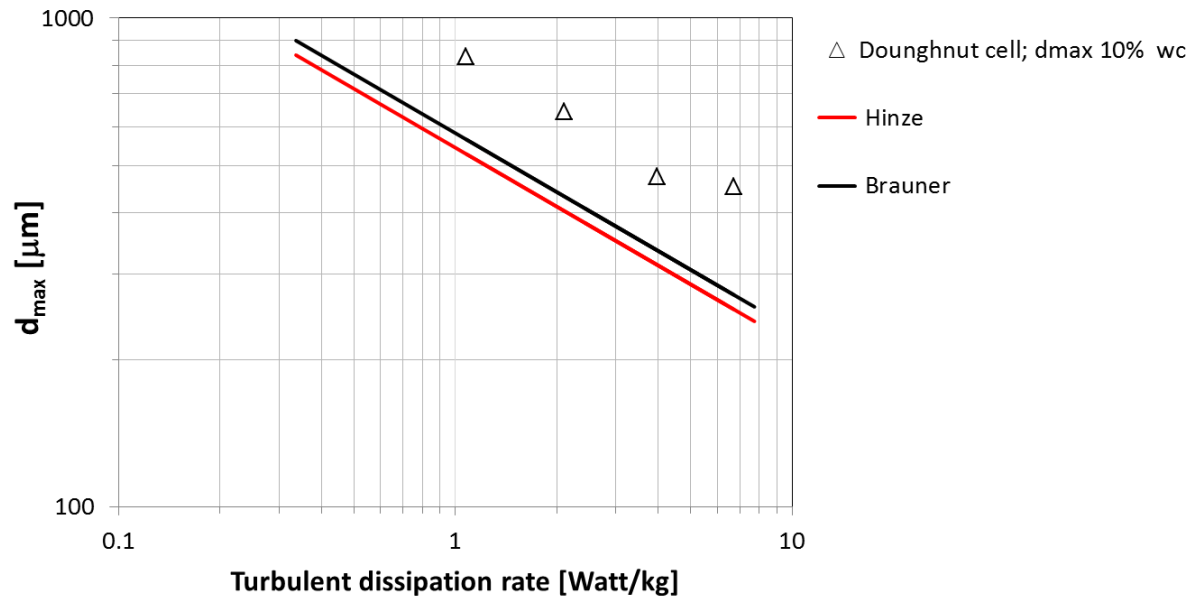


Figure 28. Comparison between the measured maximum droplet size and the Hinze/Brauner model predictions in relation to the energy dissipation rate at 10% average water cut - Doughnut cell configuration.

6.1.2.2 Effect of water cut

The comparison between the measured maximum droplet size and the Hinze/Brauner model predictions in relation to the water cut at 2, 4 and 7 *Watt/kg* average turbulent dissipation rates are shown in Figure 29, Figure 30, Figure 31, respectively. The shortage of the data points makes any meaningful comparison difficult. However, in both cases, Hinze's model predicts d_{max} within a 5% error margin. Brauner's model under predicts d_{max} at higher water cuts ($5\% < \text{water cut} < 20\%$).

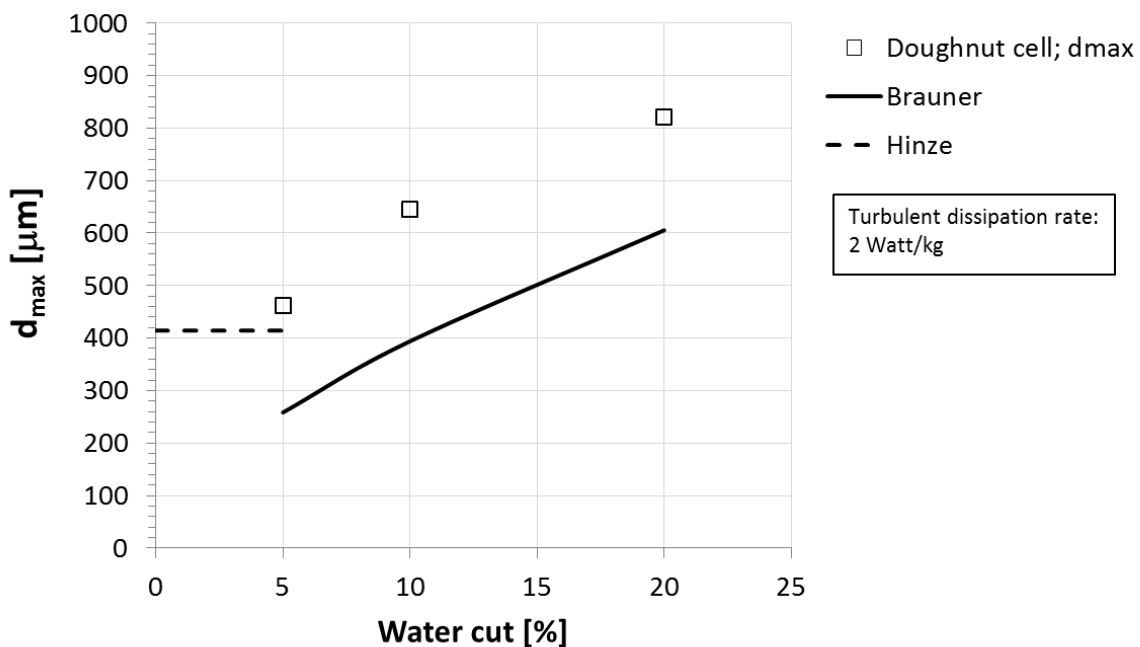


Figure 29. Comparison between the measured maximum droplet size and the Hinze/Brauner model predictions in relation to the water cut at 2 *Watt/kg* turbulent dissipation rate - Doughnut cell configuration.

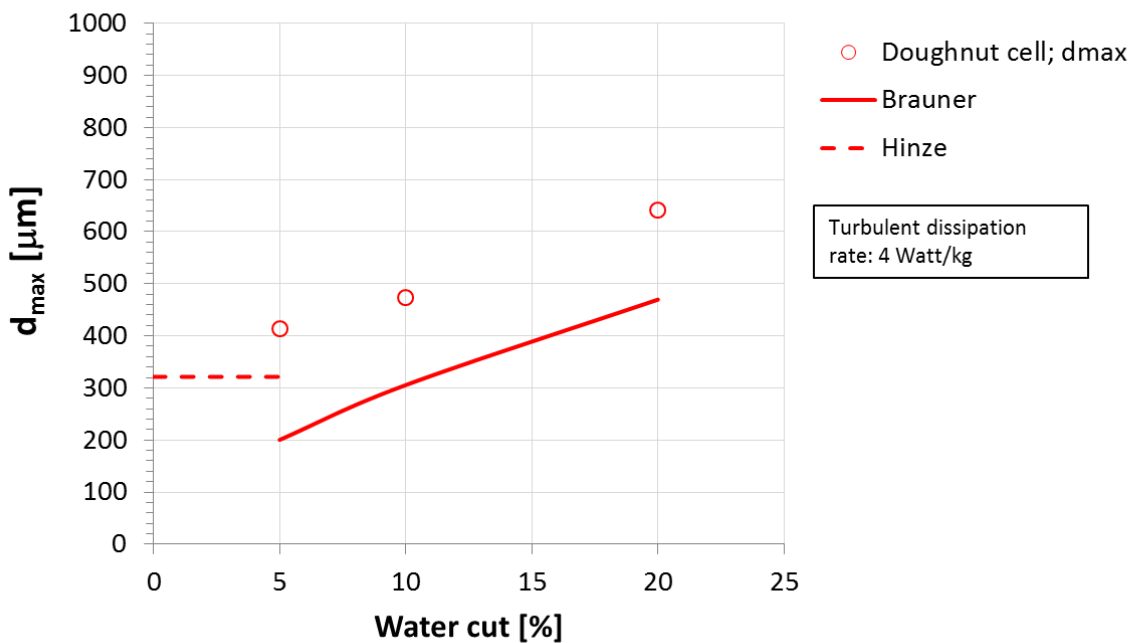


Figure 30. Comparison between the measured doughnut cell maximum droplet size and the Hinze/Brauner model predictions in relation to the water cut at 4 *Watt/kg* turbulent dissipation rate - Doughnut cell configuration.

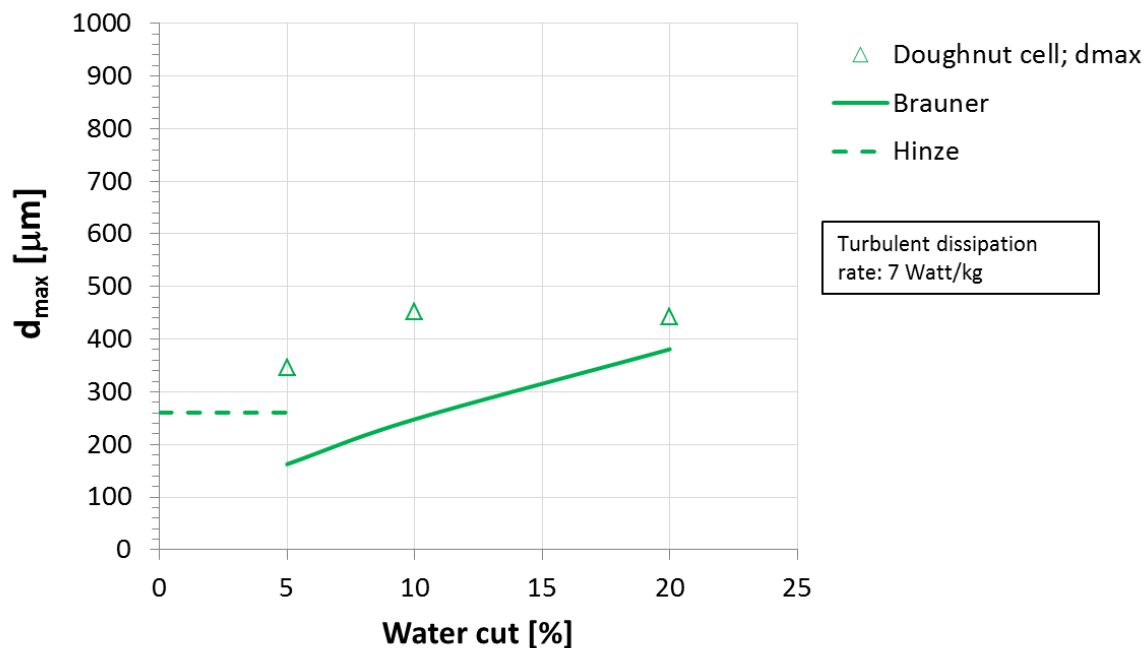


Figure 31. Comparison between the measured maximum droplet size and the Hinze/Brauner model predictions in relation to the water cut at 7 *Watt/kg* turbulent dissipation rate - Doughnut cell configuration.

Figure 32 shows the comparison between the measured maximum droplet size and Hinze and Brauner model predictions. Hinze's model is used to predict d_{max} in dilute dispersion (water cut = 5%). Brauner model is used to predict d_{max} in dense dispersion (water cut > 5%). This plot shows 50% prediction points are out of the $\pm 30\%$ error bonds. As mentioned in the previous section, improvements in the modeling approach are proposed in Chapter 6.1.4.

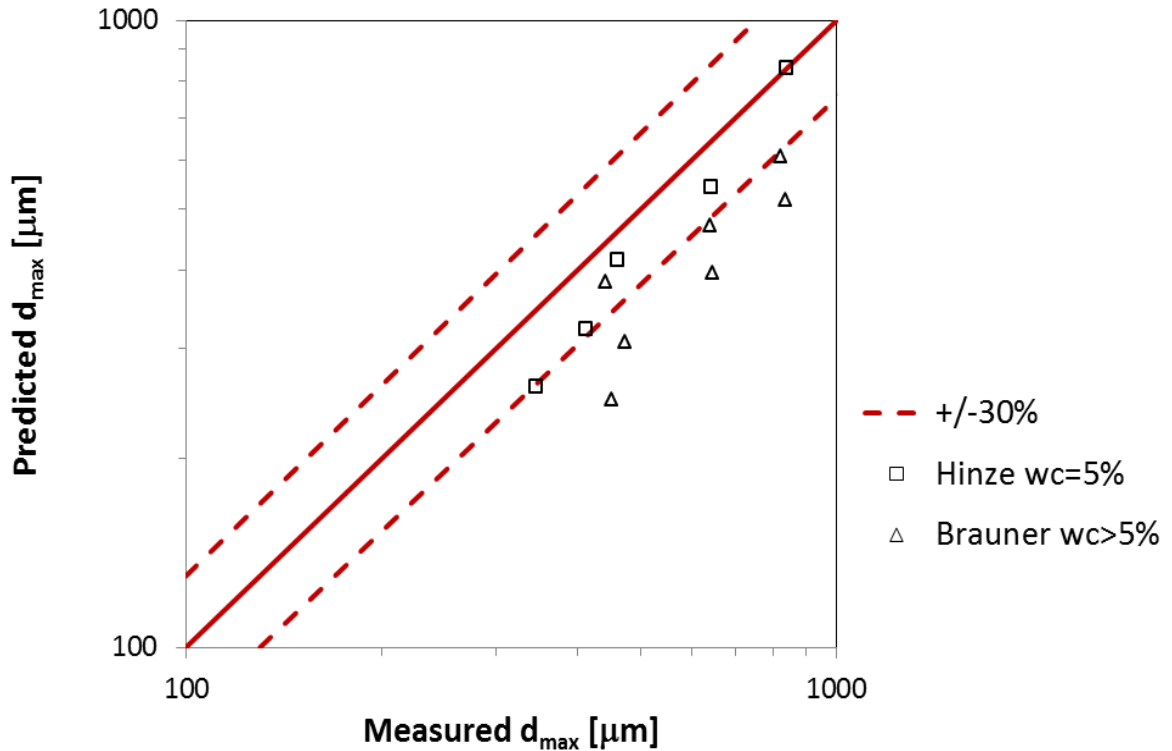


Figure 32. Comparison between the doughnut cell maximum droplet size data and Hinze/Brauner model predictions - Doughnut cell configuration.

6.1.3 Summary of results obtained in the standard pipe

The operating conditions characteristics of the “standard pipe” are a turbulent dissipation range: of 0.3 to 1.1 *Watt/kg*, an oil-water interfacial tension of 50 mN/m, and a water cut range: 1% to 10%. As for the previous section, the influence of two main operating parameters, turbulent energy dissipation rate and water cut, is treated in turn. Experimental results are also compared to Hinze’s and Brauner’s model predictions.

6.1.3.1 Effect of turbulent dissipation rate

The measured maximum droplet size in relation to the energy dissipation rate at 1% average water cut in horizontal and vertical standard pipe configurations is shown in Figure 33. The energy dissipation rate varies from 0.02-1.2 *Watt/kg*. As for the previous

experimental setups (doughnut cell and standard pipe with mixing valve), the maximum droplet size tends to decrease as the energy dissipation rate increases. A least square fitting is performed on the experimental data using power law, a slope of -0.21 is found. This slope value differs from the Hinze theoretical value -0.4 (Equation 33), which indicates this time that droplet breakup is not the controlling mechanism defining the maximum droplet size. It is postulated that droplet coalescence has a significant effect here, especially considering that the turbulent dissipation rate is low. Figure 33 also shows that the maximum droplet size d_{\max} (μm) is in the range of $l_k < d_{\max} < 0.1D$, where, l_k is the Kolmogoroff length scale which is the smallest valid turbulent eddies' length scale in turbulence, $0.1D = 1\text{cm}$ is one tenth of pipe diameter which is the largest valid length scale of turbulent eddies in turbulence.

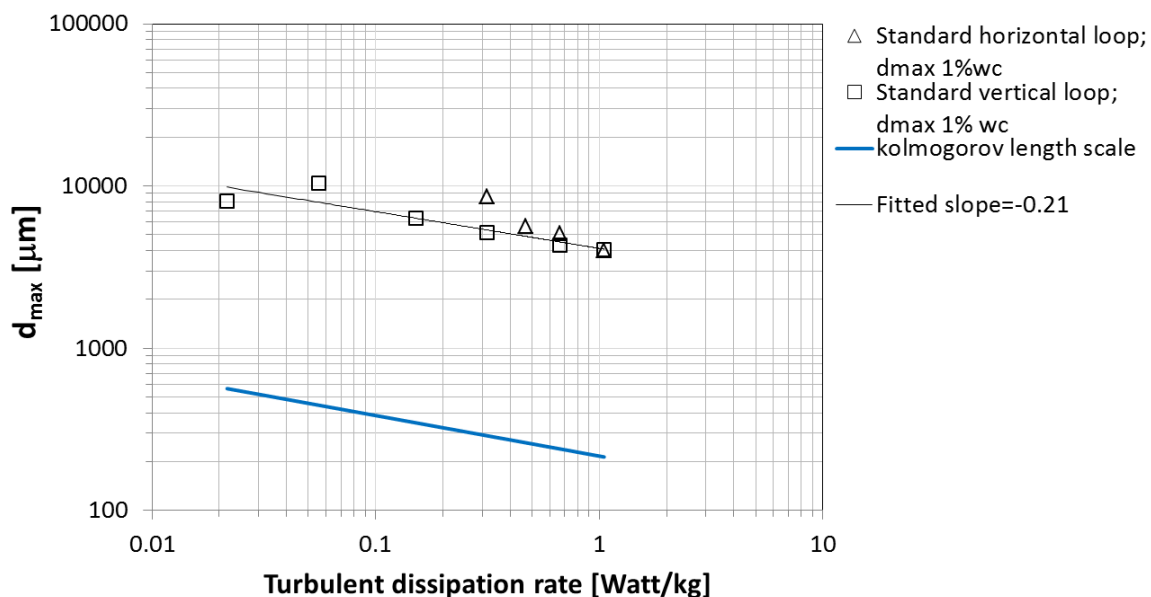


Figure 33. Measured maximum droplet size in relation to the energy dissipation rate at 1% average water cut – Horizontal standard pipe configuration.

The comparison between the measured maximum droplet size and the Hinze/Brauner model predictions in relation to the energy dissipation rate at 1% average water cut is presented in Figure 34. Hinze's model prediction agree relatively well with experimental data although the slope of the fitted line deviates from what is expected in a "pure" droplet breakup dominated environment. Brauner's model tends to under predict d_{max} , which is to be expected in dilute dispersion (water cut < 5%).

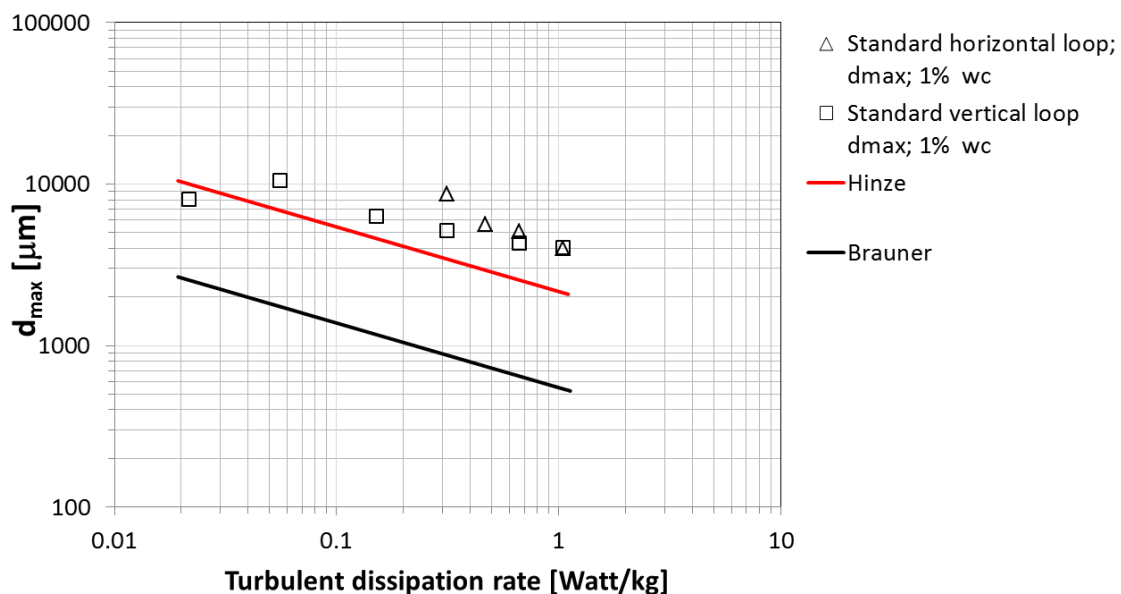


Figure 34. Comparison between the measured maximum droplet size and the Hinze/Brauner model predictions in relation to the energy dissipation rate at 1% average water cut – Horizontal standard pipe configuration.

The measured maximum droplet size in relation to the energy dissipation rate at 5% average water cut in vertical standard pipe flow is shown in Figure 35. The energy dissipation rate varies from 0.02-0.8 *Watt/kg*. Similar as for the horizontal pipe case, the maximum droplet size tends to decrease as the energy dissipation rate increases. A least square fitting using power law leads to a slope of -0.26. This slope also differs from

the Hinze theoretical value -0.4 in Equation 33, which indicates that droplet breakup is not the dominant mechanism. Droplet coalescence is suspected to play a role as well.

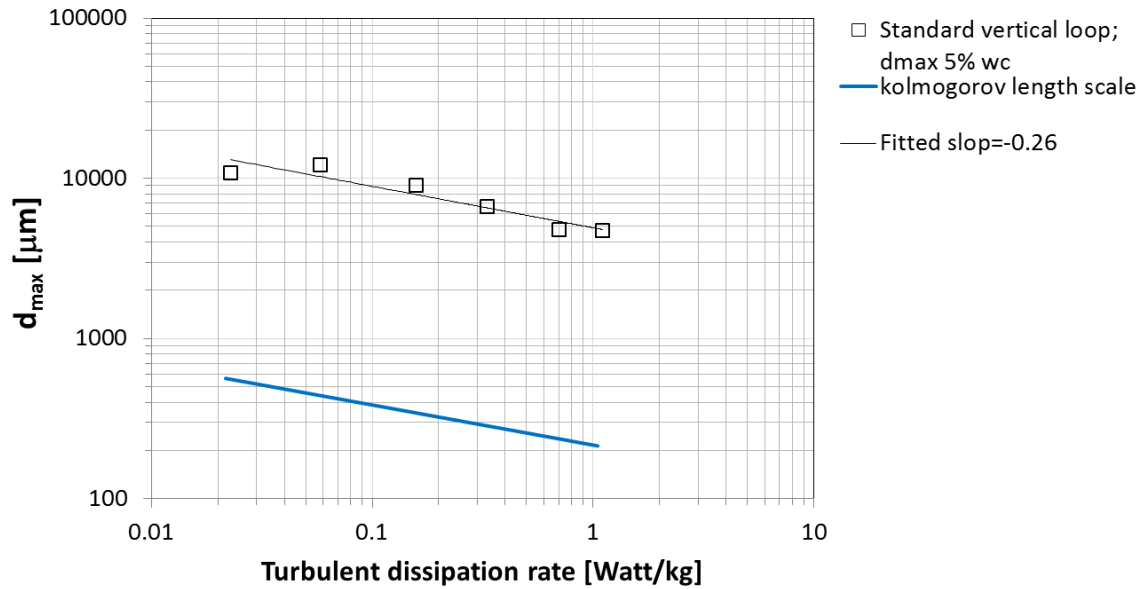


Figure 35. Measured maximum droplet size in relation to the energy dissipation rate at 5% average water cut in vertical standard pipe flow – Vertical standard pipe configuration.

Figure 36 shows the comparison between the measured maximum droplet size and the Hinze/Brauner model predictions in relation to the energy dissipation rate at 5% average water cut. Both Hinze's and Brauner's models under predict d_{max} .

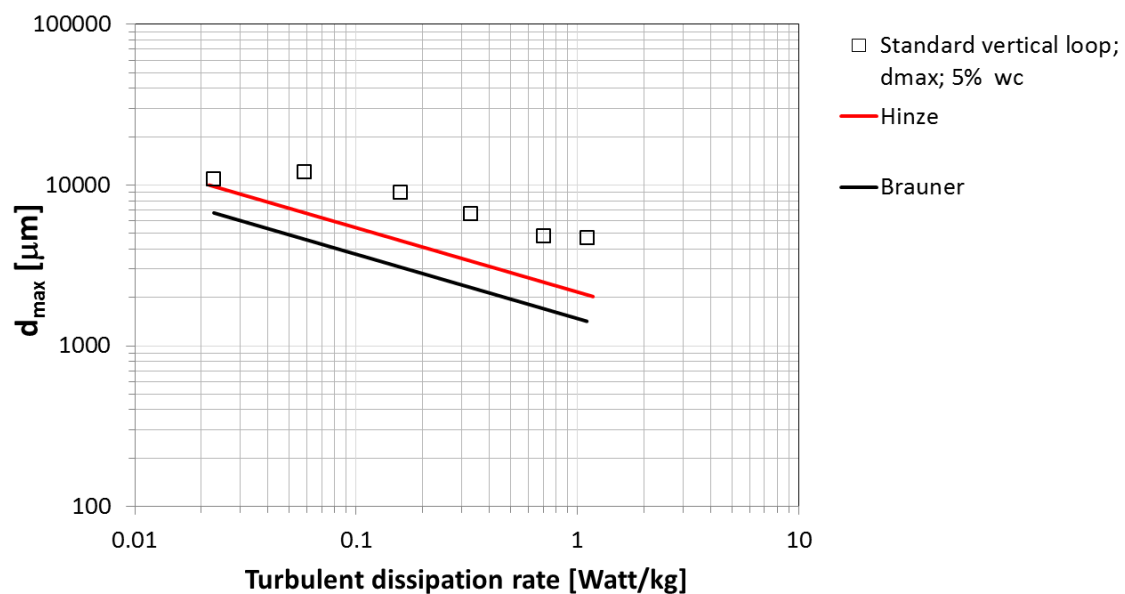


Figure 36. Comparison between the measured maximum droplet size and the Hinze/Brauner model predictions in relation to the energy dissipation rate at 5% average water cut -- Vertical standard pipe configuration.

The measured maximum droplet size in relation to the energy dissipation rate at 10% average water cut in vertical standard pipe flow is shown in Figure 37. The energy dissipation rate varies from 0.05-1.2 Watt / kg . A least square fitting gives a slope of -0.24 which is not in agreement with Hinze's theoretical value of 0.4.

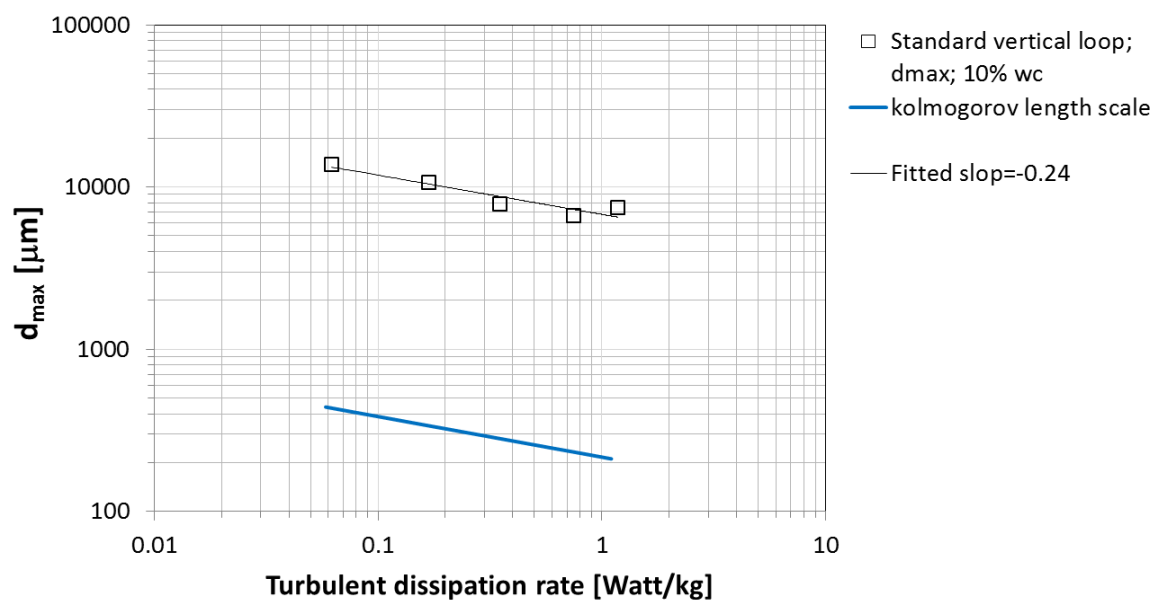


Figure 37. Measured maximum droplet size in relation to the energy dissipation rate at 10% average water cut in vertical standard pipe flow— Vertical standard pipe configuration.

Figure 38 shows the comparison between the measured maximum droplet size and the Hinze/Brauner model predictions in relation to the energy dissipation rate at 10% average water cut. Both Hinze's and Brauner's models under predict the d_{max} .

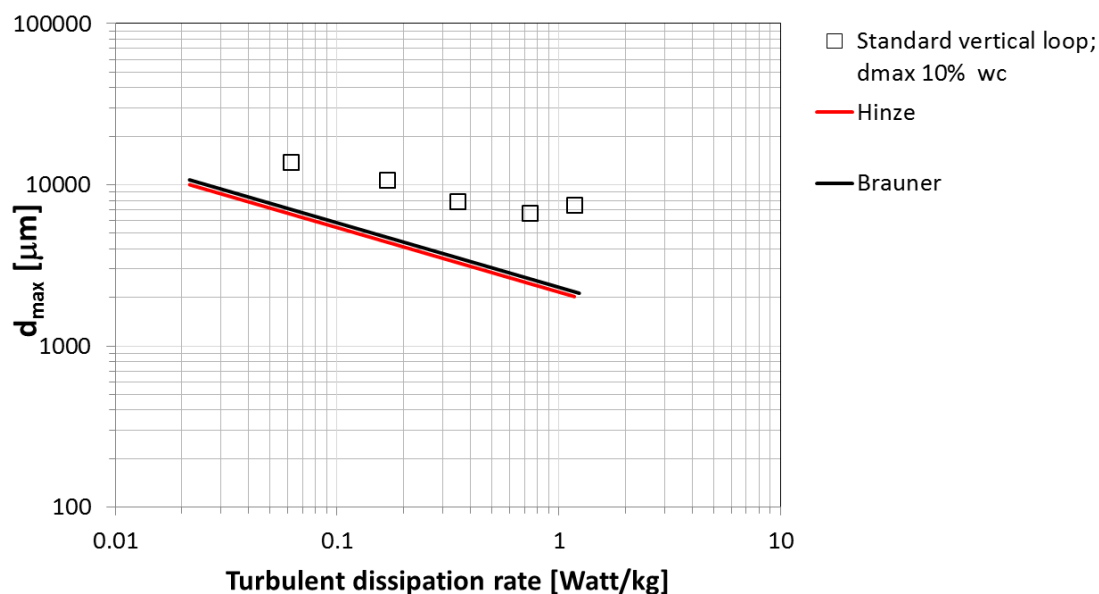


Figure 38. Comparison between the measured maximum droplet size and the Hinze/Brauner model predictions in relation to the energy dissipation rate at 10% average water cut— Vertical standard pipe configuration.

6.1.3.2 Effect of water cut

The comparison between the measured maximum droplet size and the Hinze/Brauner model predictions in relation to the water cut at 0.66 *Watt/kg* average turbulent dissipation rates in horizontal and vertical standard pipe configurations is shown in Figure 39. Both Hinze and Brauner models under predict the d_{max} at water cut range: 1% to 10%. The discrepancies are especially large in this case.

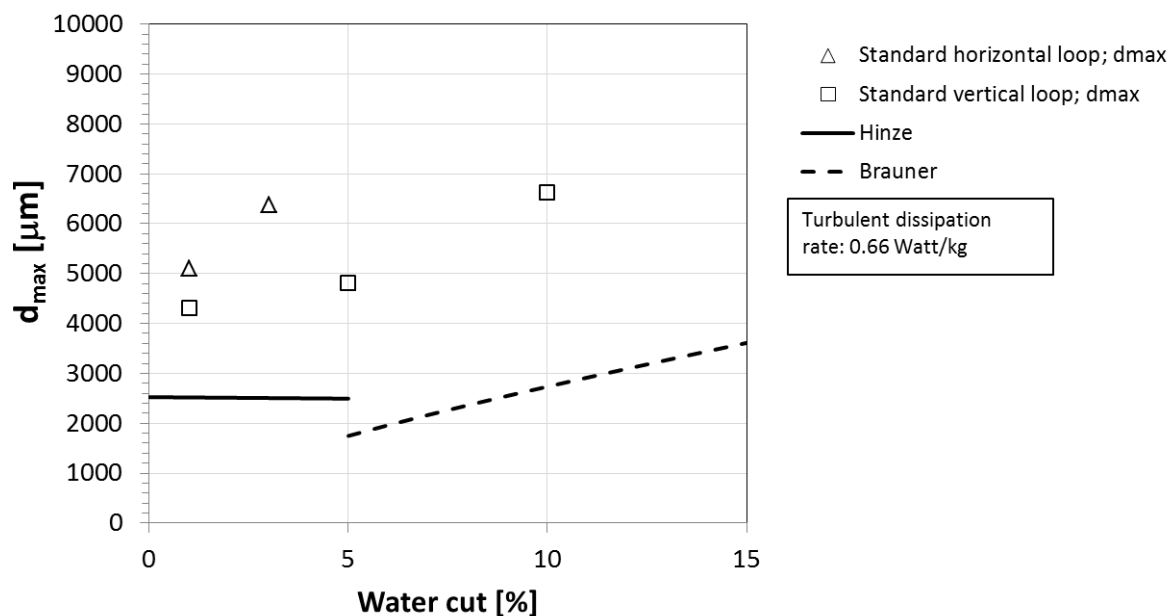


Figure 39. Comparison between the measured standard loop maximum droplet size and the Hinze/Brauner model predictions in relation to the water cut at 0.66 Watt/kg average turbulent dissipation rates - Standard pipe configuration.

Similarly, the comparison between the measured maximum droplet size and the Hinze/Brauner model predictions in relation to the water cut at higher average turbulent dissipation rates (1.1 Watt/kg) in horizontal and vertical standard loop is shown in Figure 40. Both Hinze's and Brauner's model predictions under predict the d_{max} at water cut range: 1% to 10%.

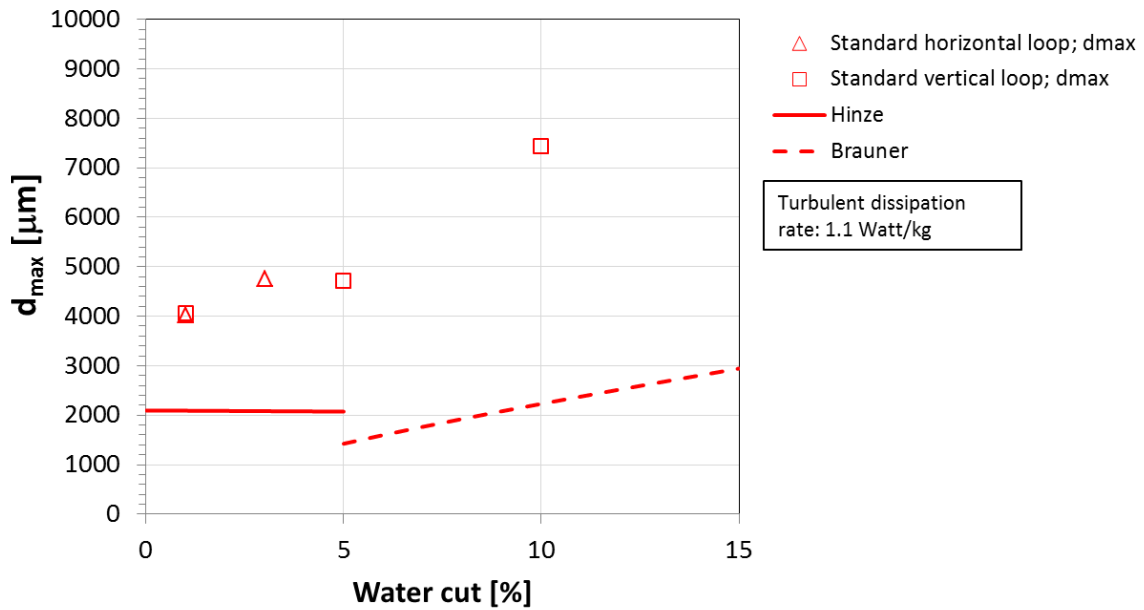


Figure 40. Comparison between the measured maximum droplet size and the Hinze/Brauner model predictions in relation to the water cut at 1.1 *Watt/kg* average turbulent dissipation rates - Standard pipe configuration.

The comparison between the measured experimental data and the Hinze/Brauner model predictions is shown in Figure 41. As mentioned earlier, Hinze's model is used to predict d_{\max} in dilute dispersion (water cut < 5%) while Brauner's model is used to predict d_{\max} in dense dispersion (water cut > 5%). This plot shows 88% prediction points are out of the $\pm 30\%$ error bonds. The discrepancy here is very large and highlights that the modeling approach is probably incorrect. The effect of coalescence, which is ignored in both Hinze's and Brauner's models, should be playing a larger role.

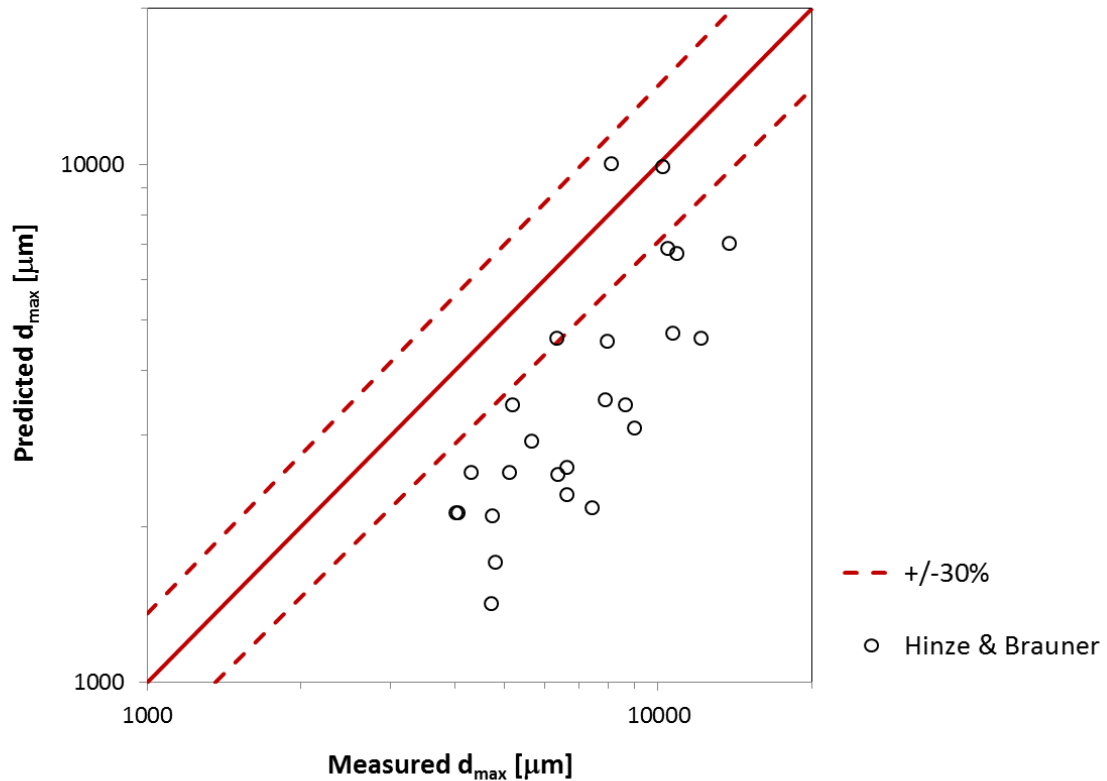


Figure 41. Comparison between the standard loop measured maximum droplet size and Hinze/Brauner model predictions.

6.1.4 Model improvement – Development of the ICMT model

The present results show that both Hinze’s and Brauner’s model predictions present significant deviations compared to experimental data, especially in standard pipe configuration. Although the underlying mechanism of droplet breakup is correct in case of the “doughnut cell” and the “standard pipe with mixing valve” experiments, half of the prediction points still show over 30% percentage error. This is partly due to their limited range of validity, with Hinze’s model being only valid for low water cuts and Brauner’s model being only valid for high water cuts. Developing a unified model for a wider range of water cut would address most of the issues.

A single comprehensive model covering maximum droplet size predictions for both dilute and dense dispersion was developed by Paolinelli, at Institute of Corrosion and Multiphase Technology (ICMT), Ohio University [57]. The development of this model, labeled the ICMT model, was not an objective of the present study although the data generated here were used for the model calibration. It is briefly summarized in the following section.

The ICMT model uses the same approach proposed by Hinze and Brauner. The underlying mechanism is droplet breakup and coalescence is still neglected. The ICMT model's main improvement is by modifying the fitting constant (C_H). The Brauner model (Equation 72) initially assumed the fitting constant $C_H = 1$ [17].

$$d_{max} = \left(C_H \frac{6\varepsilon_d}{(1 - \varepsilon_d)} \right)^{3/5} \left(\frac{\sigma}{\rho_c} \right)^{3/5} \bar{e}^{-2/5} \quad (72)$$

The ICMT model (Equation 73) modifies Brauner's model fitting constant C_H to a function of water cut: $g(\varepsilon)$.

$$d_{max} = \left(g(\varepsilon) \frac{\varepsilon_d}{(1 - \varepsilon_d)} \right)^{3/5} \left(\frac{4\sigma}{\rho_c} \right)^{3/5} \bar{e}^{-2/5} \quad (73)$$

The function of water cut $g(\varepsilon)$:

$$g(\varepsilon) = C_I + C_{II} \left(\frac{\varepsilon_d}{1 - \varepsilon_d} \right) - \frac{C_I C_{II} \varepsilon_d}{C_{II} \varepsilon_d + C_I (1 - \varepsilon_d)} \quad (74)$$

The constants C_I and C_{II} are obtained from the least square fitting of experimental data obtained from loop with valve system. The fitting result gives $C_I = 0.156 \pm 0.026$ and $C_{II} = 2.64 \pm 0.23$. The ICMT model is valid for the whole range of water cut from 0 to the inversion point.

6.1.4.1 Comparison between experimental data and ICMT model predictions

Standard pipe with mixing valve

The comparison between the measured maximum droplet size and the ICMT model predictions in relation to the water cut at average turbulent dissipation rate of 122 and 220 *Watt/kg*, is shown in Figure 42 and Figure 43, respectively. The predictions are logically good since the model constants were fitted over the same data.

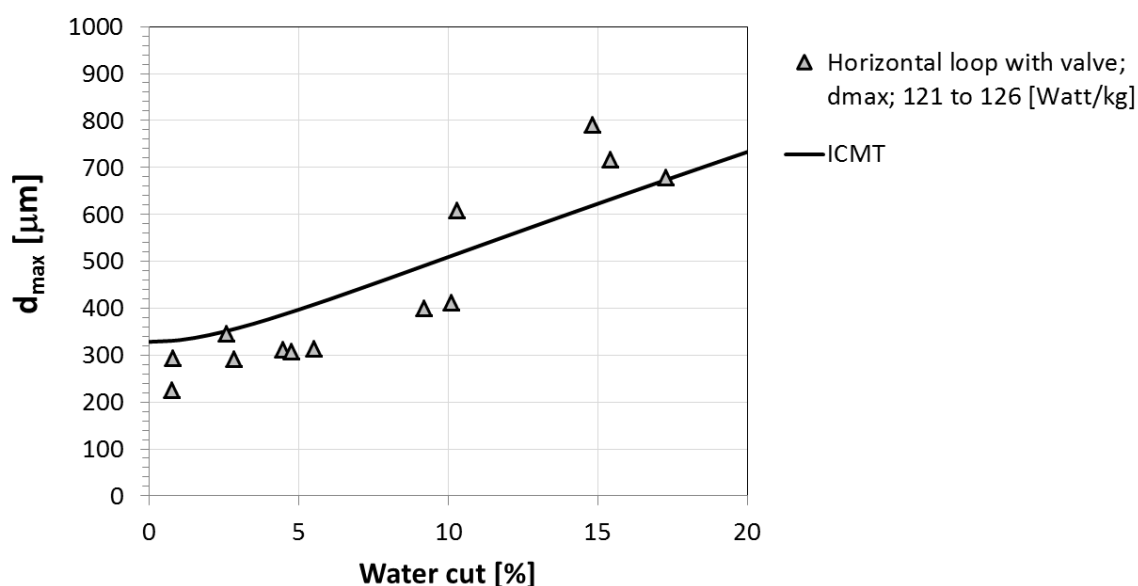


Figure 42. Comparison between the measured maximum droplet size and the ICMT model predictions in relation to the water cut at average turbulent dissipation rate 122 *Watt/kg* – Standard pipe with mixing valve configuration.

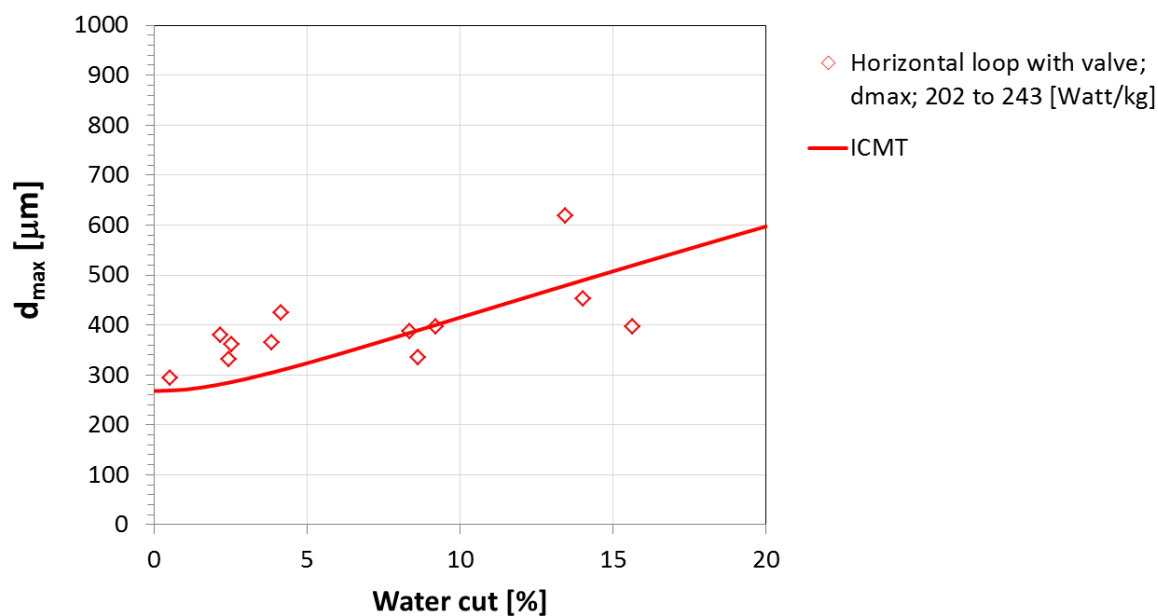


Figure 43. Comparison between the measured maximum droplet size and the ICMT model predictions in relation to the water cut at average turbulent dissipation rate 220 *Watt/kg* – Standard pipe with mixing valve configuration.

The comparison between the measured and model predicted maximum droplet size is in Figure 44. The ICMT model predicts d_{max} in dilute dispersion (water cut < 5%) and dense dispersion (water cut > 5%) with good accuracy. This plot shows 11% prediction points are out of the $\pm 30\%$ error bonds. Again, this is not surprising since this model is tuned using this same set of data.

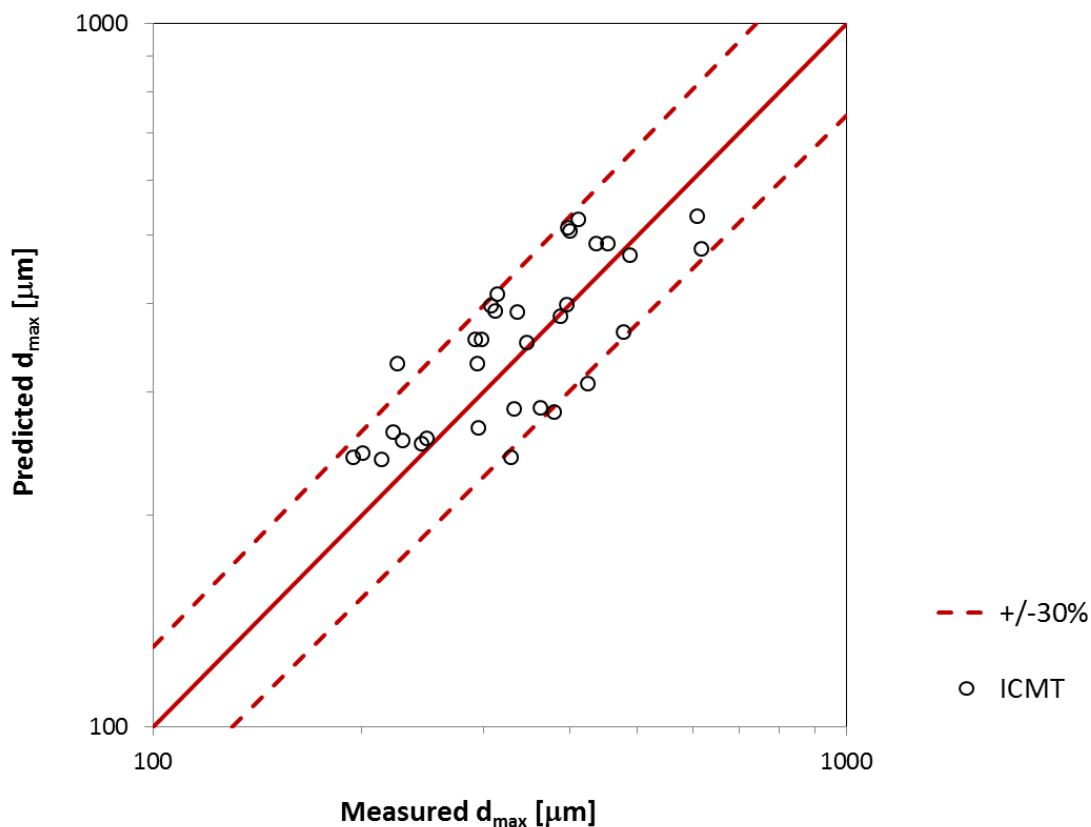


Figure 44. Comparison between the measured maximum droplet size and ICMT model predictions — Standard pipe with mixing valve configuration

Doughnut cell

Figure 45, Figure 46, and Figure 47 are showing the comparison between the measured maximum droplet size and the ICMT model predictions in relation to the water cut for the doughnut cell system. Both Figure 45 and Figure 46 show good prediction results for whole water cut range. Figure 47 shows the ICMT model under prediction occurs at 5% and 10% water cut and over prediction occurs at 20% water cut.

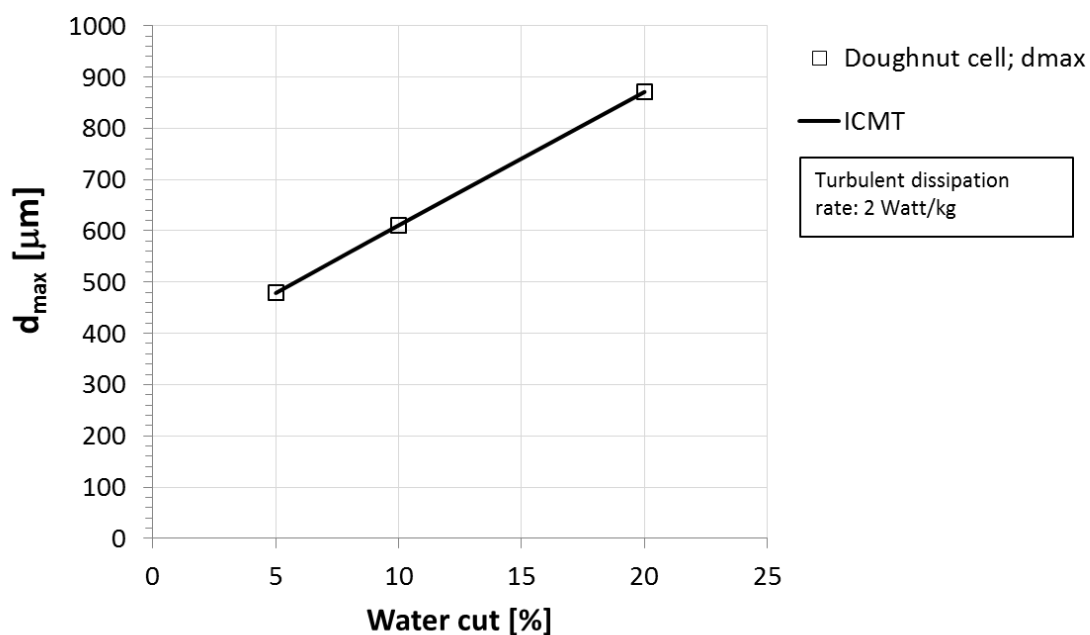


Figure 45. Comparison between the measured maximum droplet size and the ICMT model predictions in relation to the water cut at 2 *Watt/kg* turbulent dissipation rate – Doughnut cell configuration

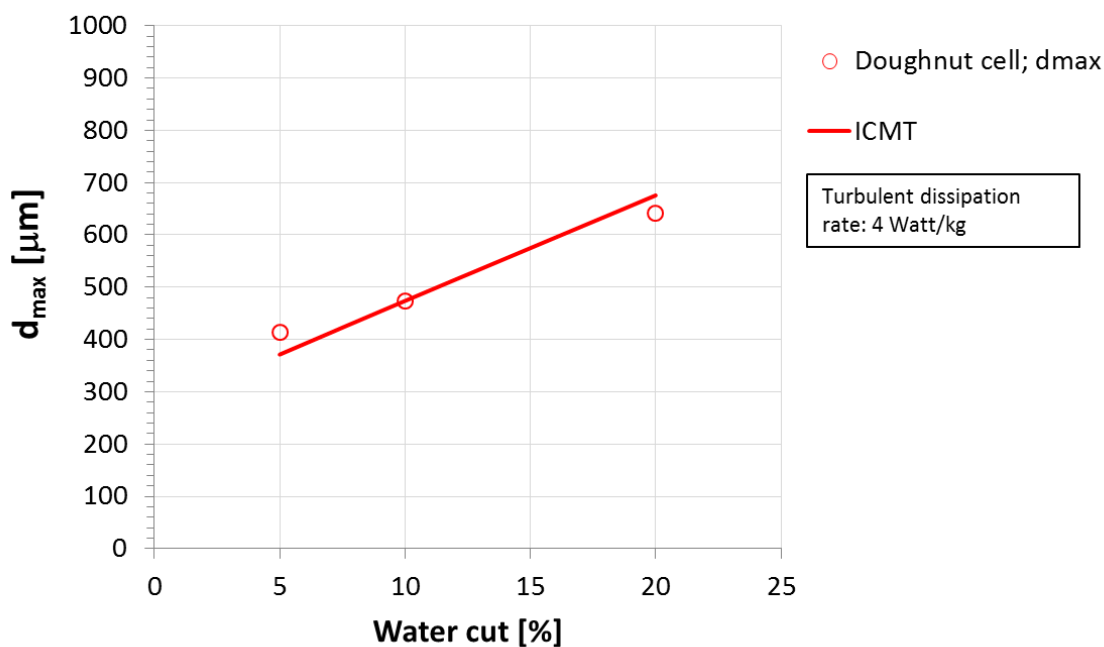


Figure 46. Comparison between the measured maximum droplet size and the ICMT model predictions in relation to the water cut at 4 *Watt/kg* turbulent dissipation rate – Doughnut cell configuration

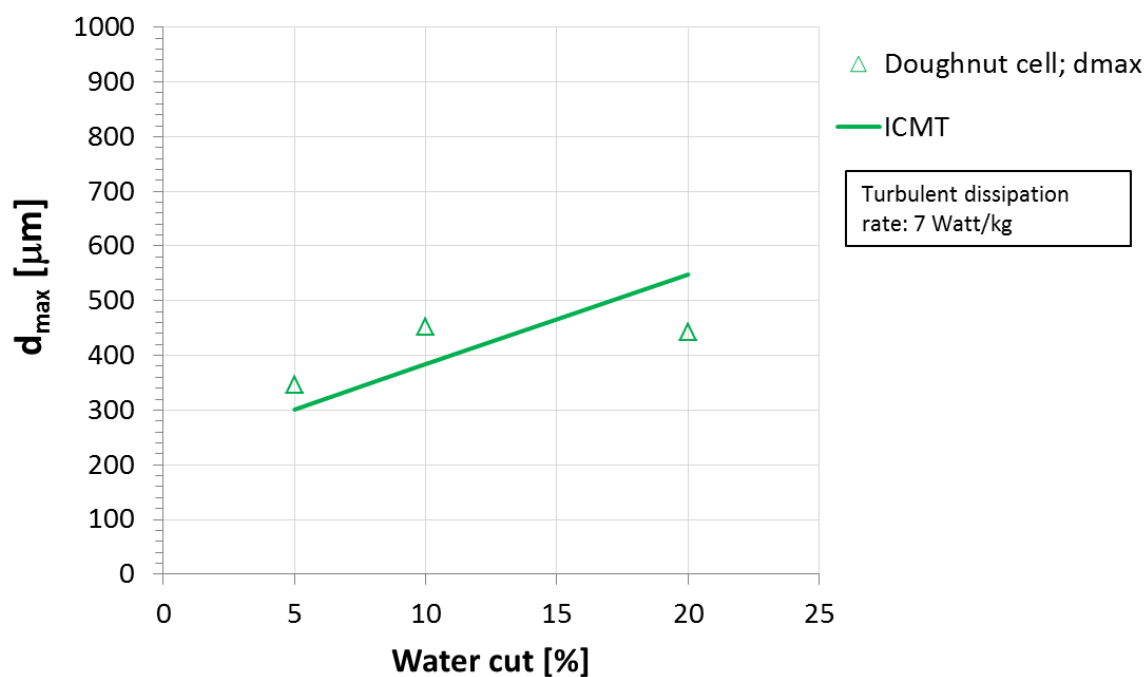


Figure 47. Comparison between the measured maximum droplet size and the ICMT model predictions in relation to the water cut at 7 *Watt/kg* turbulent dissipation rate — Doughnut cell configuration

Comparison between the measured maximum droplet size data and the ICMT model predictions has been showed in Figure 48. The ICMT model predicts d_{max} for both dilute dispersion (water cut = 5%) and dense dispersion (water cut > 5%) within $\pm 30\%$ error.

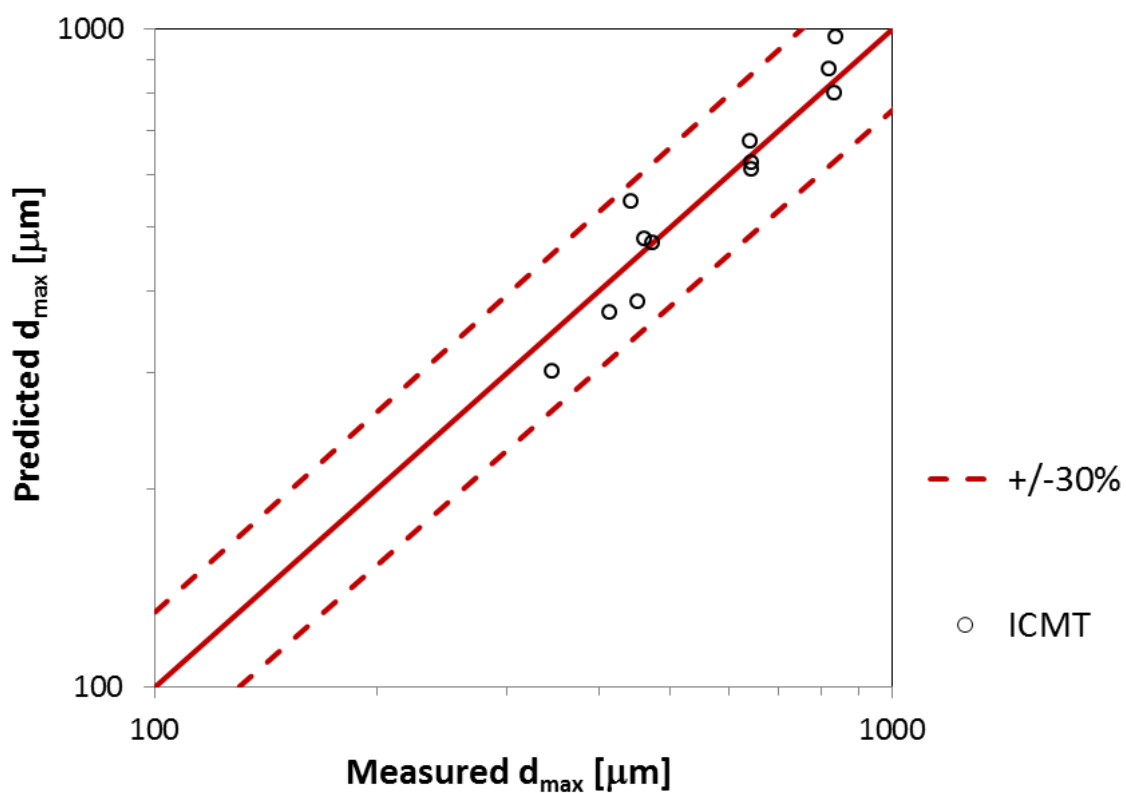


Figure 48. Comparison between the doughnut cell maximum droplet size data and ICMT model predictions.

The ICMT model shows logically better accuracy compared to the Hinze/Brauner model in the doughnut cell and standard pipe with mixing valve configurations. This confirms that droplet breakup is the dominant mechanism determining maximum droplet size.

Standard pipe (no mixing valve)

Figure 49 and Figure 50 show the comparisons between the measured maximum droplet size and the ICMT model predictions in horizontal and vertical standard pipe configuration. The data are plotted in relation to the water cut at average turbulent

dissipation rates of 0.66 and 1.1 *Watt/kg* Both comparisons show ICMT model largely under predicts the d_{\max} at water cut range from 1% to 10%.

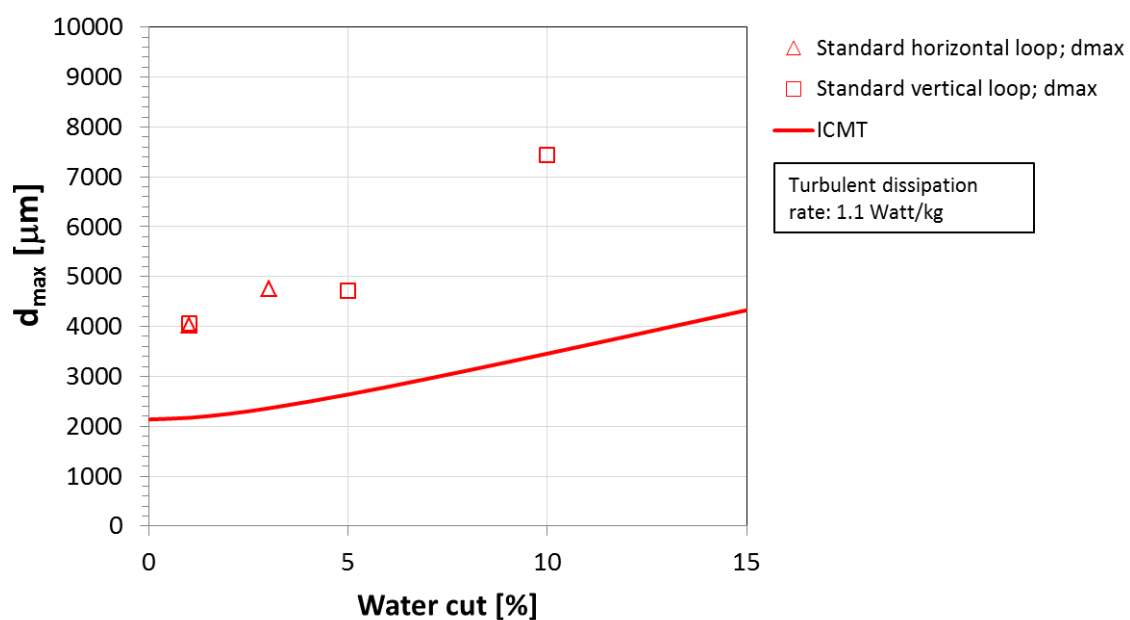


Figure 49. Comparison between the measured maximum droplet size and the ICMT model predictions in relation to the water cut at 1.1 *Watt/kg* average turbulent dissipation rates – Standard pipe configuration

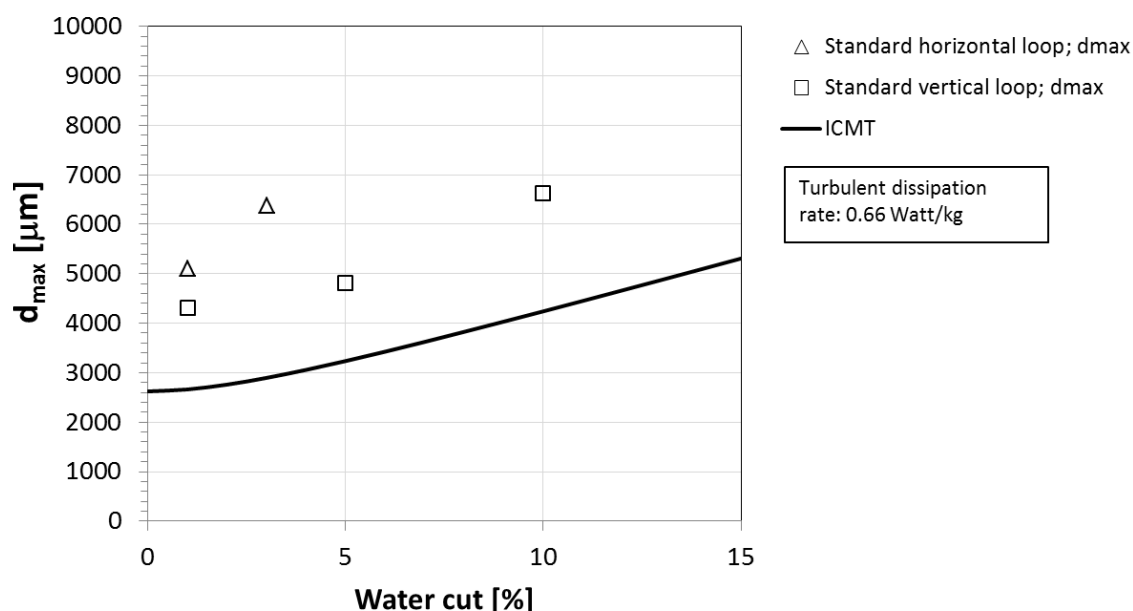


Figure 50. Comparison between the measured maximum droplet size and the ICMT model predictions in relation to the water cut at 0.66 *Watt/kg* average turbulent dissipation rates - - Standard pipe configuration

ICMT model predictions are compared with the experimental data from “standard pipe” experiments using a parity plot in Figure 51. The plot shows that 80% prediction points are out of the $\pm 30\%$ error bonds. Although the correlation of the ICMT model was fitted over the entire set of experimental, it is clear that this particular set (standard pipe flow configuration without a mixing valve) is not well predicted. Large discrepancies were also found when compared to the Hinze/Brauner model predictions. This suggests that the reason for these discrepancies is related to the underlying mechanism, in this case the assumption that coalescence can be neglected, rather than the fitting of the constants.

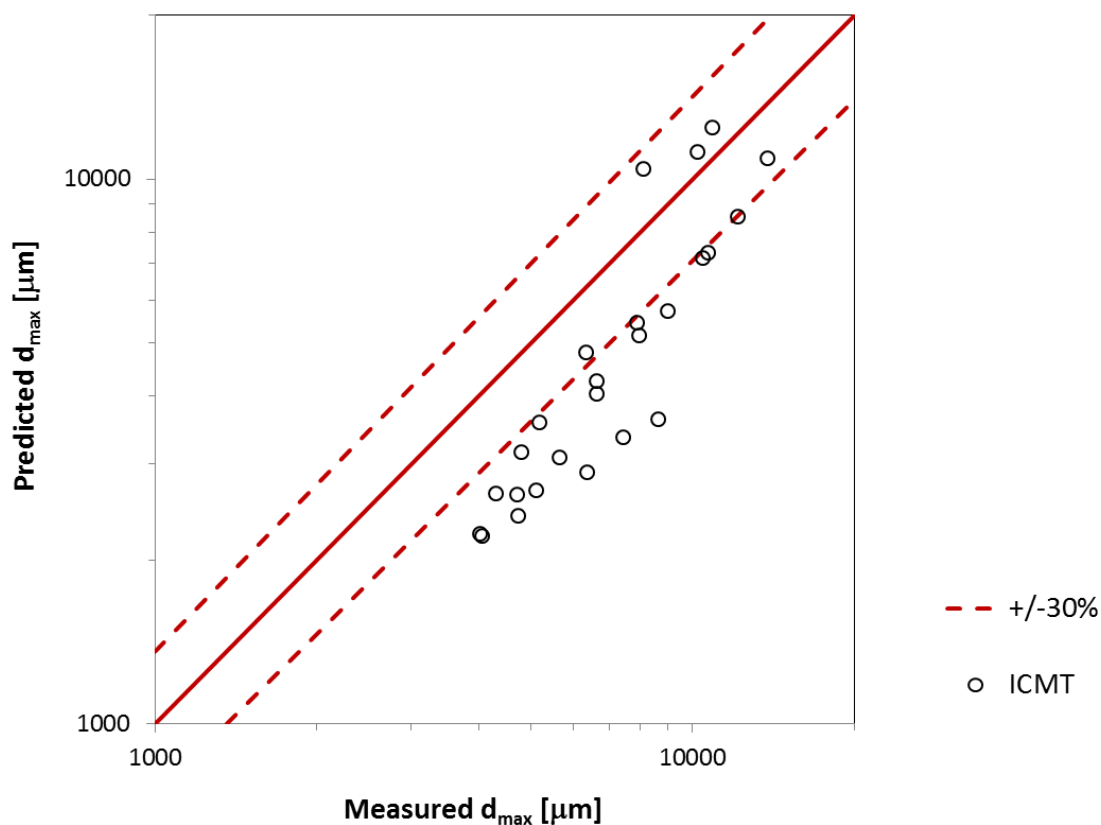


Figure 51. Comparison between the standard pipe measured maximum droplet size and ICMT model predictions.

6.1.4.2 Comparison between literature data and ICMT model predictions

Until now, the data used for comparison with model predictions have all been generated in-house. To be complete, the models validation needs to be performed against more literature data, like the ones introduced in Chapter 2.5.

First, the literature maximum droplet size data are compared with Hinze/Brauner model predictions in Figure 52. Hinze's model is used to predict d_{\max} in dilute dispersion (water cut $< 5\%$) while Brauner's model is used to predict d_{\max} in dense dispersion (water cut $> 5\%$). This plot shows 49% prediction points are out of the $\pm 30\%$ error bonds.

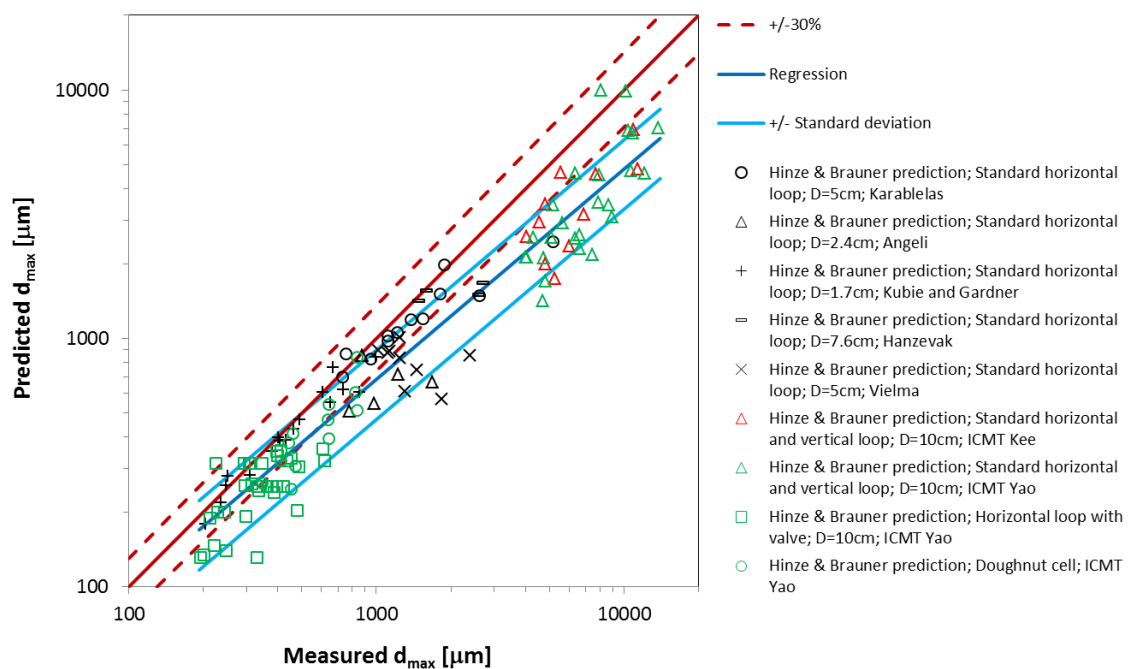


Figure 52. Comparison of Hinze/Brauner model predictions with literature experimental maximum droplet size

Figure 53 shows the comparison between the literature maximum droplet size data and the ICMT model predictions. The plot shows 25% prediction points are out of the $\pm 30\%$ error bonds.

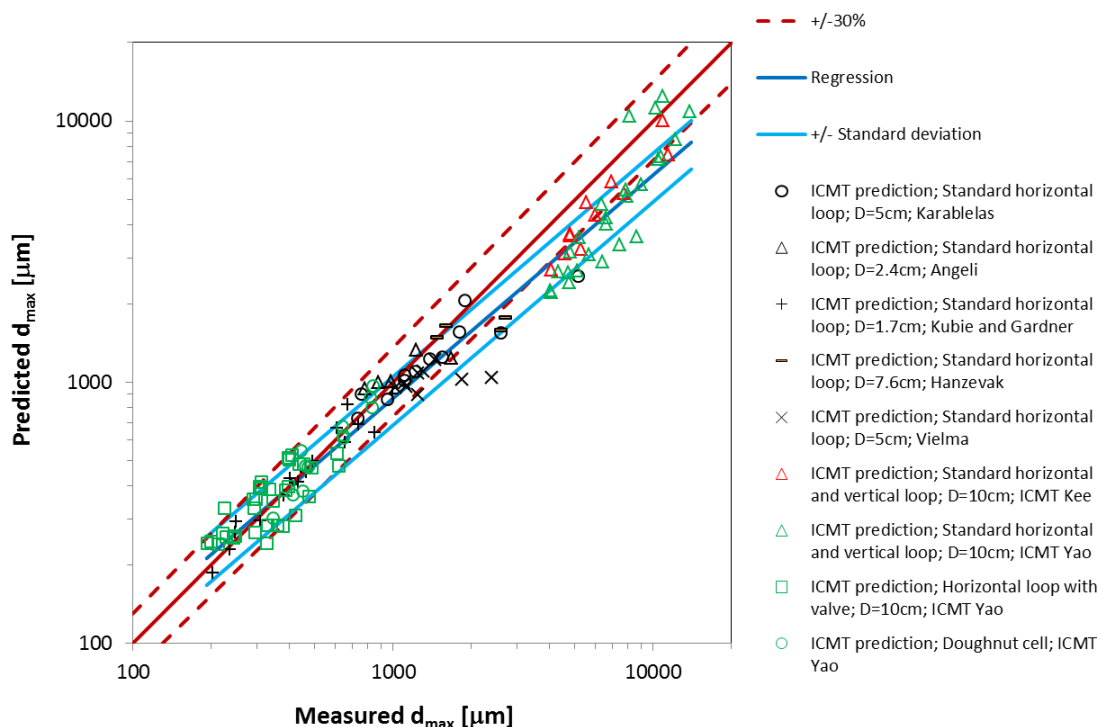


Figure 53. Comparison of ICMT model predictions with literature experimental maximum droplet size.

The ICMT model clearly shows better accuracy compared to the Hinze/Brauner modeling approach. To further demonstrate this point, Figure 52 and Figure 53 also show linear regression functions (dark blue lines) of the predicted d_{\max} vs. measured d_{\max} data points. A measure of how spread the data are is given by calculating the standard deviation (light blue lines). First, a linear regression is applied on all the data points and compared with the parity line “ $y=x$ ”. The percentage error between the two lines is then collected for each data point. The regression line is then modified to minimize the mean percentage error. The upper and lower bonds of the regression line are then created by adding/subtracting the standard deviation of the percentage error.

Comparing the ICMT and Hinze/Brauner model predictions, it is clear that the regression function obtained for the ICMT model is closer to the parity line, meaning the prediction accuracy is higher than for the Hinze/Brauner model. In addition, the predicted d_{\max} vs. measured d_{\max} plots for the ICMT model show smaller standard deviations, which means that the ICMT model displays also a higher prediction precision. As this point, it is believed that the ICMT model gives superior predictions as long as the underlying mechanism governing the maximum droplet size is determined by droplet breakup. The ICMT model can therefore be applied with confidence when assessing highly turbulent systems or industrial flows, such as multiphase water / crude oil lines, where droplet breakup is clearly dominant and where droplet coalescence can be reasonably neglected. However, Figure 53 still shows that the model tends to significantly underestimate large maximum droplet sizes. This is the case for horizontal or vertical pipe flow configurations with low level of turbulent dissipation rate and high oil/water interfacial tension. In these cases, typically encountered in multiphase gas condensate lines, coalescence cannot be neglected anymore and large model prediction errors are expected. The next section presents a qualitative analysis on the effect of coalescence on maximum droplet size predictions.

6.1.4.3 Effect coalescence on maximum droplet size

Current maximum droplet size prediction models are based on the mechanism of droplet breakup and the effect of coalescence is typically neglected. Large prediction error occurs when these models are used to predict maximum droplet size at low turbulent intensity or when the coalescence cannot be neglected. In this section, the

magnitude of the prediction errors is plotted against the ratio of droplet breakup rate to droplet coalescence rate. The intent here is to clearly identify coalescence as the main culprit by trying to correlate high prediction errors with low breakup/coalescence rates ratio. More generally, coalescence effects on maximum droplet size predictions are also discussed.

As mentioned earlier, droplet coalescence is enhanced in two ways, by increasing the chance of droplet-droplet interactions and by decreasing the ratio of breakup rate g (m^3/s) to coalescence rate Γ (m^3/s) [13], [17]. Low values of g/Γ are representative of “high coalescence” systems (relative to breakup). In addition, high values of local water concentration correspond to high chances of droplet-droplet interactions. In general, a dilute uniform dispersion has a low local water concentration and low chance of droplet-droplet interaction. A dense uniform dispersion displays a high local water concentration and a high chance of droplet-droplet interaction. A dilute non-uniform dispersion shows a high local water concentration at the bottom of the pipe and a high chance of droplet-droplet interaction.

In this section, the effect of droplet coalescence on the d_{max} prediction error is first demonstrated with the Hinze/Brauner model and then with the ICMT model.

6.1.4.3.1 Coalescence effect on Hinze and Brauner model predictions.

Figure 54, Figure 55 and Figure 56 plot the magnitude of the Hinze/Brauner model prediction errors against the ratio of breakup rate to coalescence rate in uniform dilute dispersion, in uniform dense dispersion and in non-uniform dilute dispersion, respectively. In all cases, the largest prediction errors tend to occur at low

breakup/coalescence ratios (g/Γ). These cases are typical of standard pipe flow experiments where the coalescence effect is the greatest. The experimental data of “doughnut cell” configuration is not included in this comparison due to the added surfactant which can affect the surface mobility of the oil-water contact interface and lead to in-accurate calculation of coalescence rate [35].

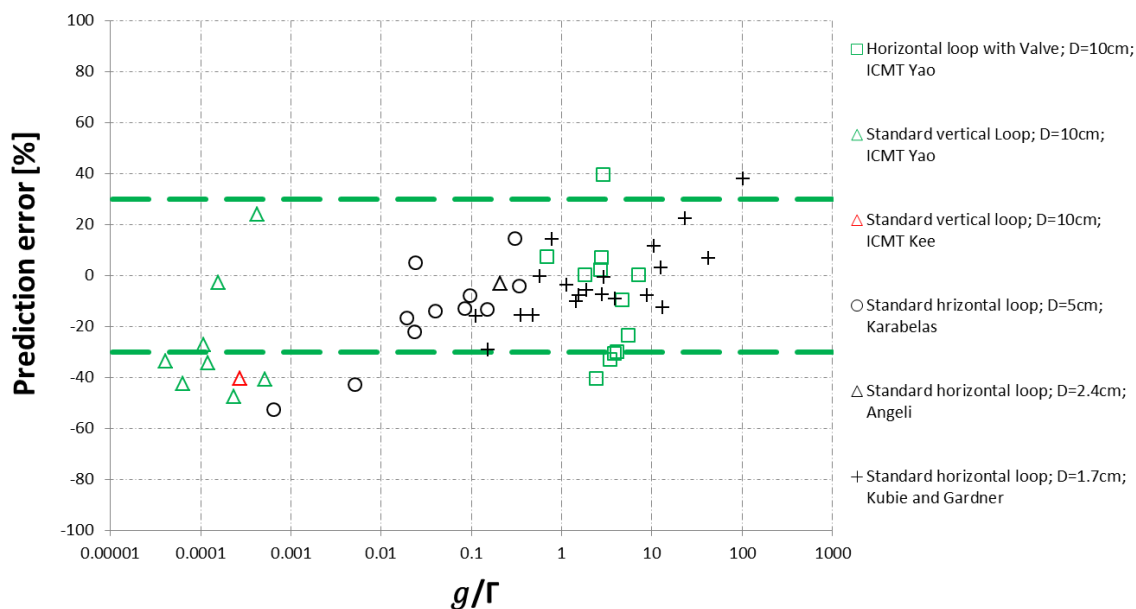


Figure 54. Comparing Hinze/Brauner model prediction errors with the ratio of breakup rate to coalescence rate in uniform dilute dispersion.

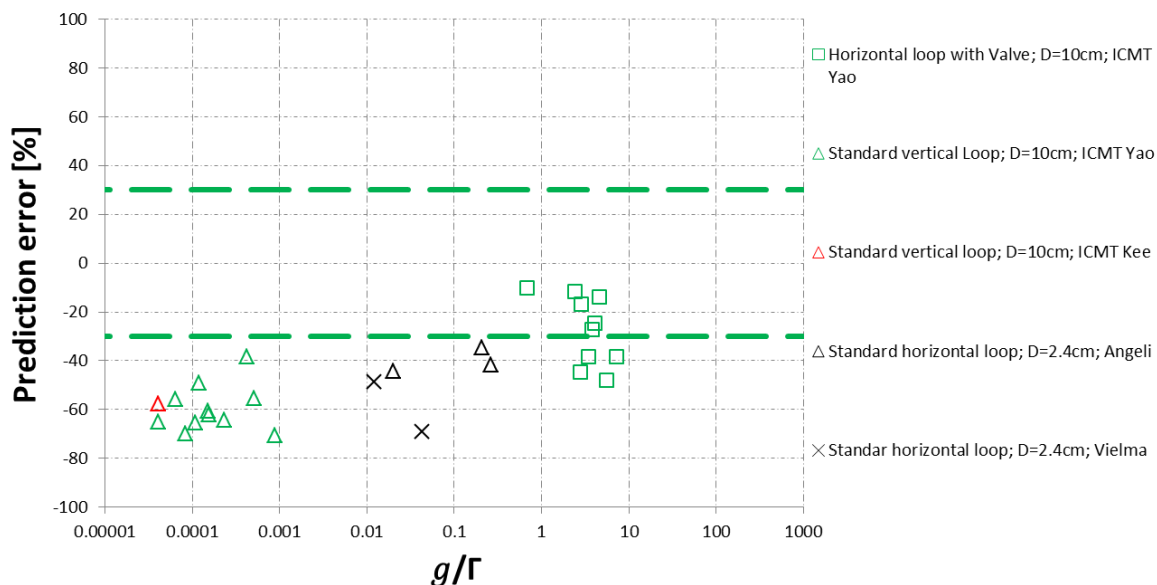


Figure 55. Comparing Hinze/Brauner model prediction errors with the ratio of breakup rate to coalescence rate in uniform dense dispersion.

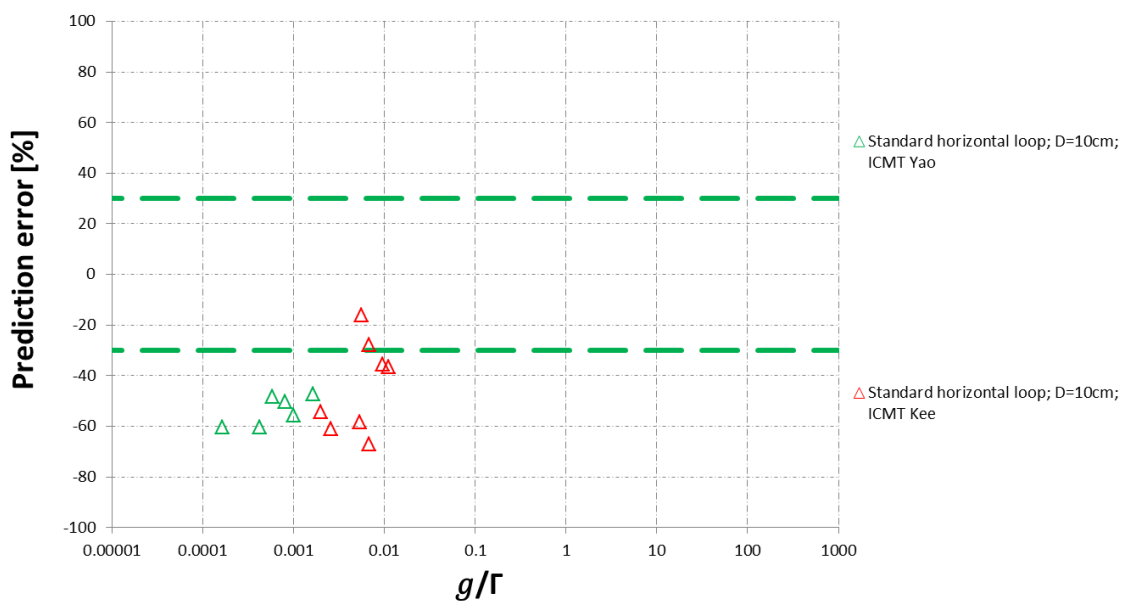


Figure 56. Comparing Hinze/Brauner model prediction errors with the ratio of breakup rate to coalescence rate in non-uniform dilute dispersion.

6.1.4.3.2 Coalescence effect on ICMT model predictions

The comparison of the magnitude of prediction errors, obtained with the ICMT model, with the ratio of breakup rate to coalescence rate in uniform dilute dispersion, in uniform dense dispersion and non-uniform dilute dispersion are presented in Figure 57, Figure 58 and Figure 59, respectively. As for the Hinze/Brauner model, most of the large prediction errors occur at low ratio (g/Γ). The ICMT model consistently under predicts the maximum droplet size, with a magnitude of error above 30%, when the coalescence rate is high relatively to the breakup rate. The effect of coalescence is clearly identified as the main reason for prediction errors. Consequently, future models should take coalescence into account in order to extend the domain of validity of the maximum droplet size model predictions.

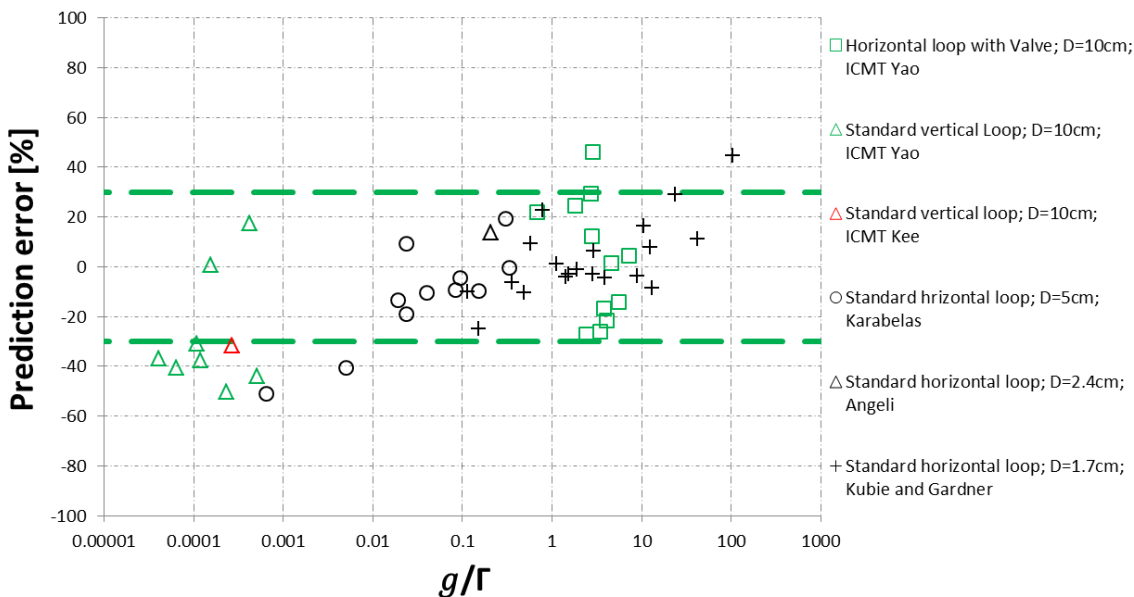


Figure 57. Comparing ICMT model prediction errors with the ratio of breakup rate to coalescence rate in uniform dilute dispersion.

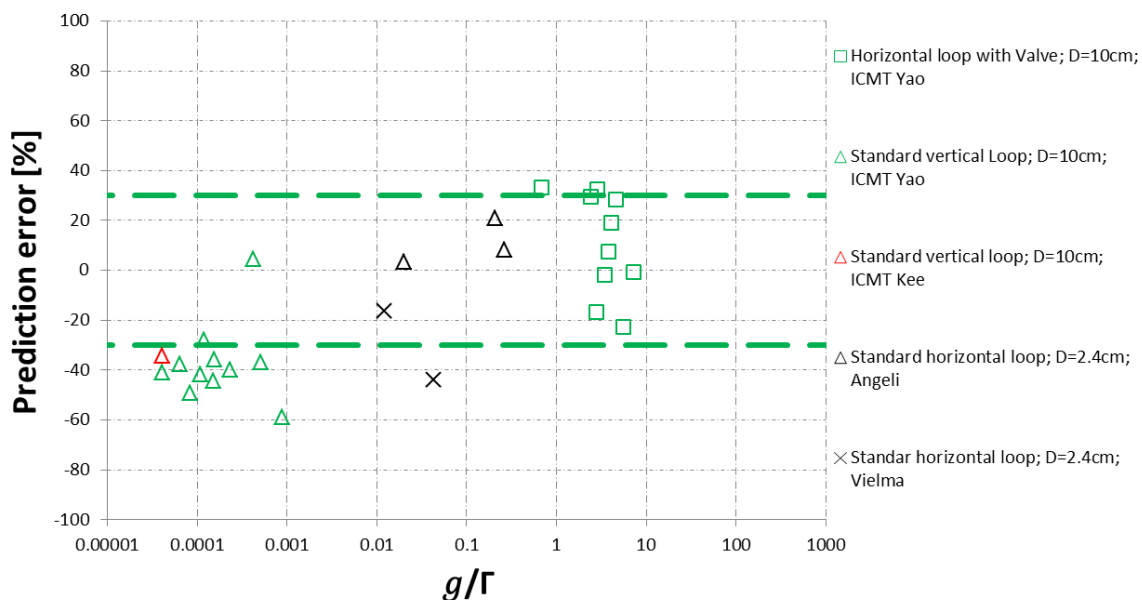


Figure 58. Comparing ICMT model prediction errors with the ratio of breakup rate to coalescence rate in uniform dense dispersion.

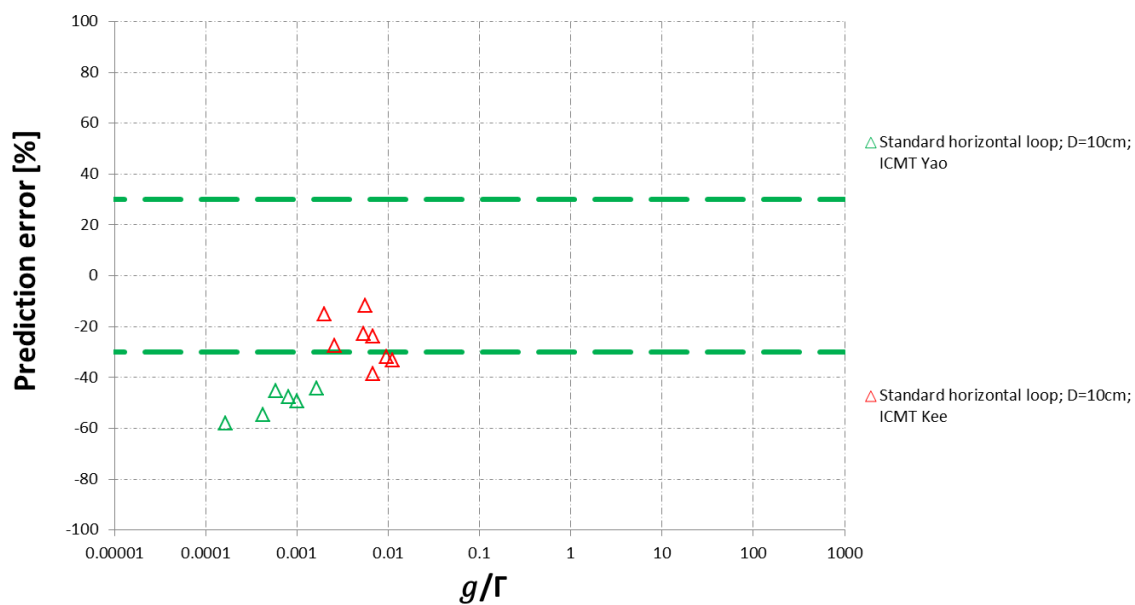


Figure 59. Comparing ICMT model prediction errors with the ratio of breakup rate to coalescence rate in non-uniform dilute dispersion.

6.2 Droplet size distribution results

In addition to the determination of maximum droplet sizes, another main objective of this work is to collect experimental data of droplet size distribution in water-in-oil dispersion for a wide range of flow conditions and fluid properties. Similarly to the previous section, experimental droplet size distributions are obtained from three different flow configurations: horizontal pipe with mixing valve, doughnut cell apparatus and standard horizontal pipe. The data are also compared to existing prediction model predictions (in this case the Rosin Rammler empirical equation). The dependence of fitted parameters on the operating conditions as discussed in order to identify physical relationships and eventually develop a more mechanistic approach to the prediction of droplet size distributions.

More specifically, the experimental results of droplet size distribution are shown as cumulative volume fractions versus droplet size, instead of the more standard volume fraction versus droplet size. This way, the results can be directly compared to model predictions using the Rosin-Rammler correlation (Equation 37). An example of fitted droplet size distribution is shown in Figure 60 with the measured parameter $d^* = 106\mu\text{m}$ and fitted parameter $n = 2.1$ at 2.2% water volume fraction and 205 *Watt/kg* turbulent dissipation rate.

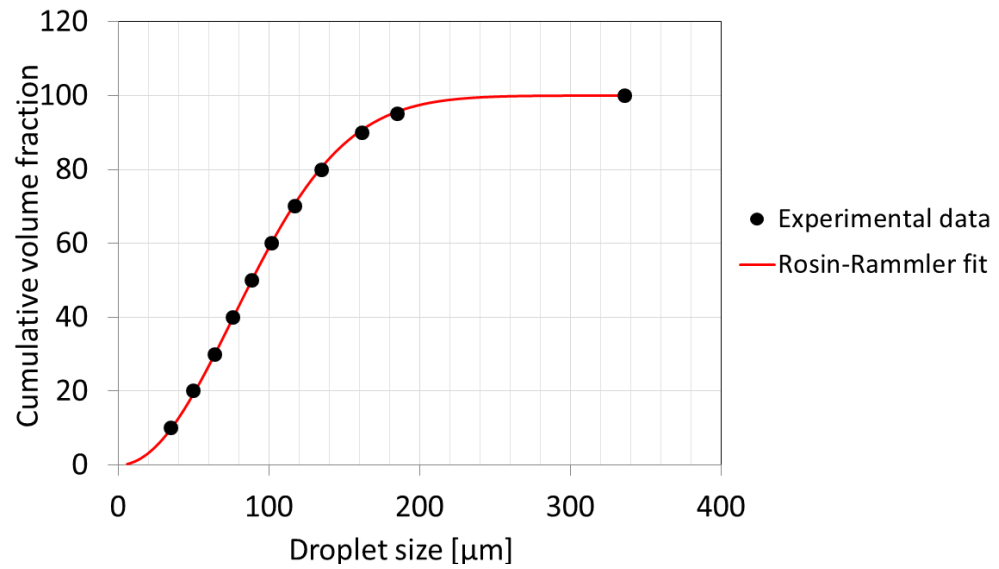


Figure 60. Example of a droplet size distribution obtained at 2.2% water cut and 205Watt/kg turbulent dissipation rate

Since the parameter $d^* = d_{63}$ is directly, measured from each droplet size distribution, the fitted parameter $n(-)$ can be easily calculated by determining the slope of the function $f(V)$ over function $f(d/d^*)$ as is shown in Figure 61.

$$f(V) = \ln(-\ln(1 - V)) \quad (75)$$

$$f(d/d^*) = -\ln(d/d^*) \quad (76)$$

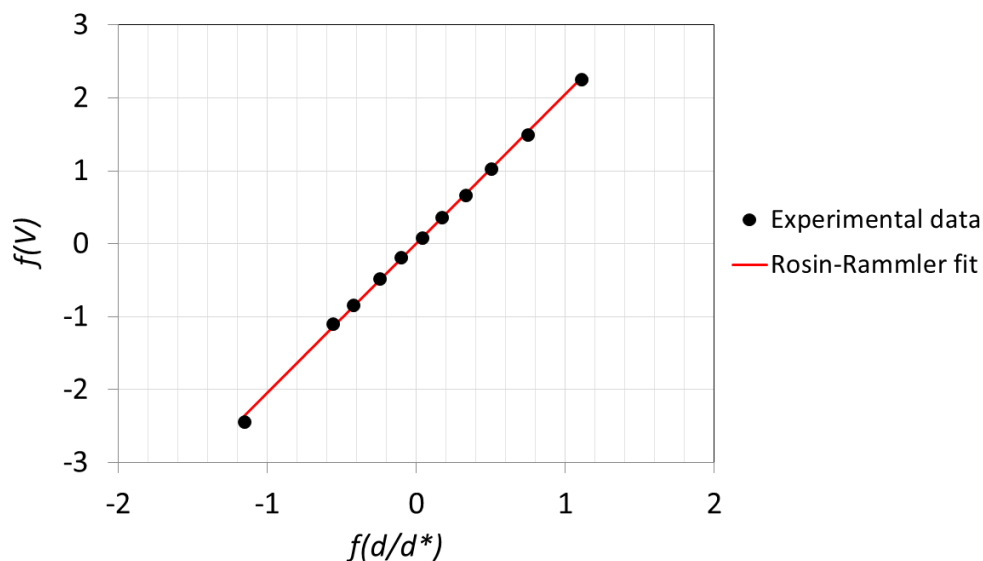


Figure 61. Example of parameter $n(-)$ determination.

In the following sections, the experimental results are first plotted in order to highlight the effect of water cut and turbulent energy dissipation rate in the three different experimental setups selected. As mentioned earlier, uncertainty and repeatability of the measurements in term of droplet size, turbulent dissipation rate, and water cut are discussed in Appendix III.

Then, efforts are made to highlight dependences of the fitted parameters n and d^* on the operating conditions in order to extract trends that could be useful for a more physical modeling approach.

6.2.1 Summary of results obtained in the standard pipe with mixing valve

The experimental results (points) and the Rosin-Rammler fitted correlation (lines) at different turbulent dissipation rate are plotted in Figure 62 for 5% water cut and Figure 63 for 10% water cut, respectively. The distribution profiles are shifted rightward and droplet size increases as the turbulent dissipation rate decreases. This makes sense since

lower turbulent dissipation rates allow for larger droplets according to the droplet breakup mechanism.

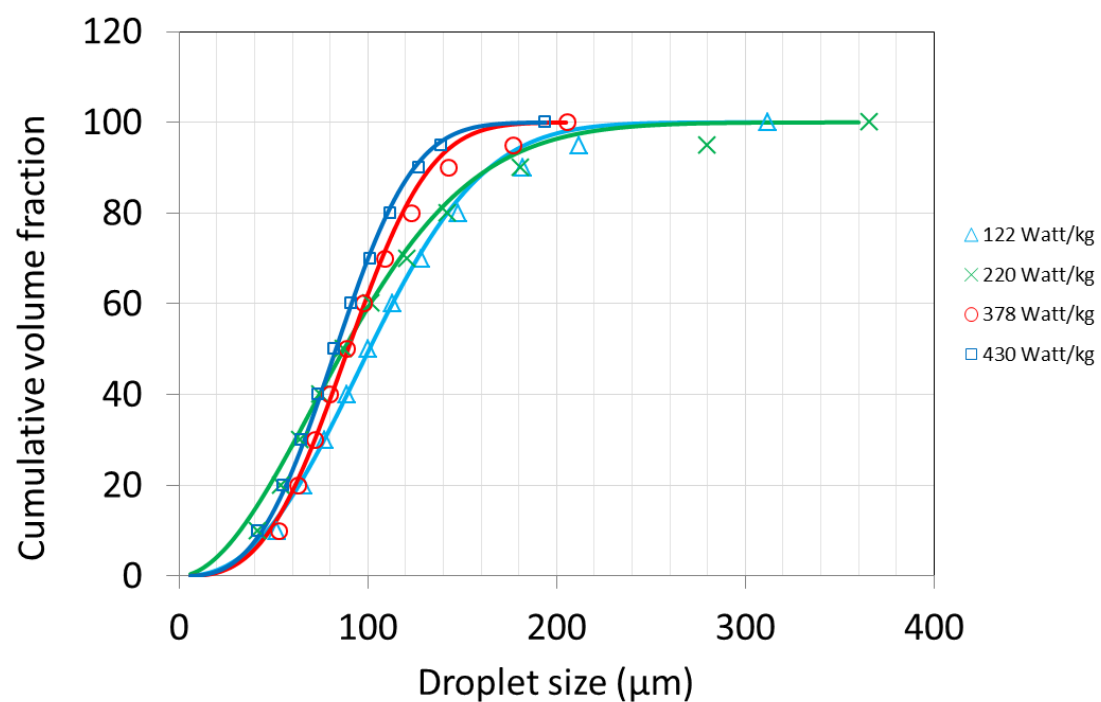


Figure 62. Effect of energy dissipation rate on the measured droplet size distribution at 5% average water cut – Standard horizontal pipe with mixing valve configuration.

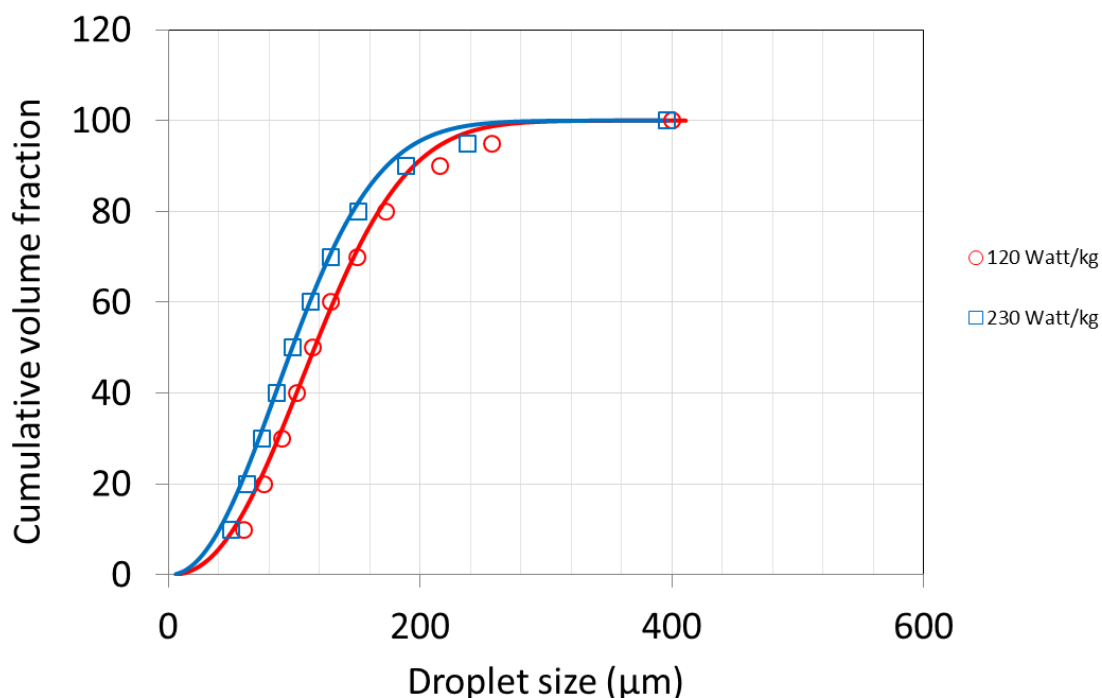


Figure 63. Effect of the energy dissipation rate on the measured droplet size distribution at 10% average water cut – Standard horizontal pipe with mixing valve configuration.

The next two graphs are plotting the same results but this time focusing on the effect of water cut. The experimental results (points) are plotted against the Rosin-Rammler correlation (lines) at different water cut for 122 *Watt/kg* (Figure 64) and for 220 *Watt/kg* (Figure 65) respectively. As the water cut increases, so do the droplet sizes and the distribution profiles are shifted rightward. A larger portion of the total water volume is held by larger droplets.

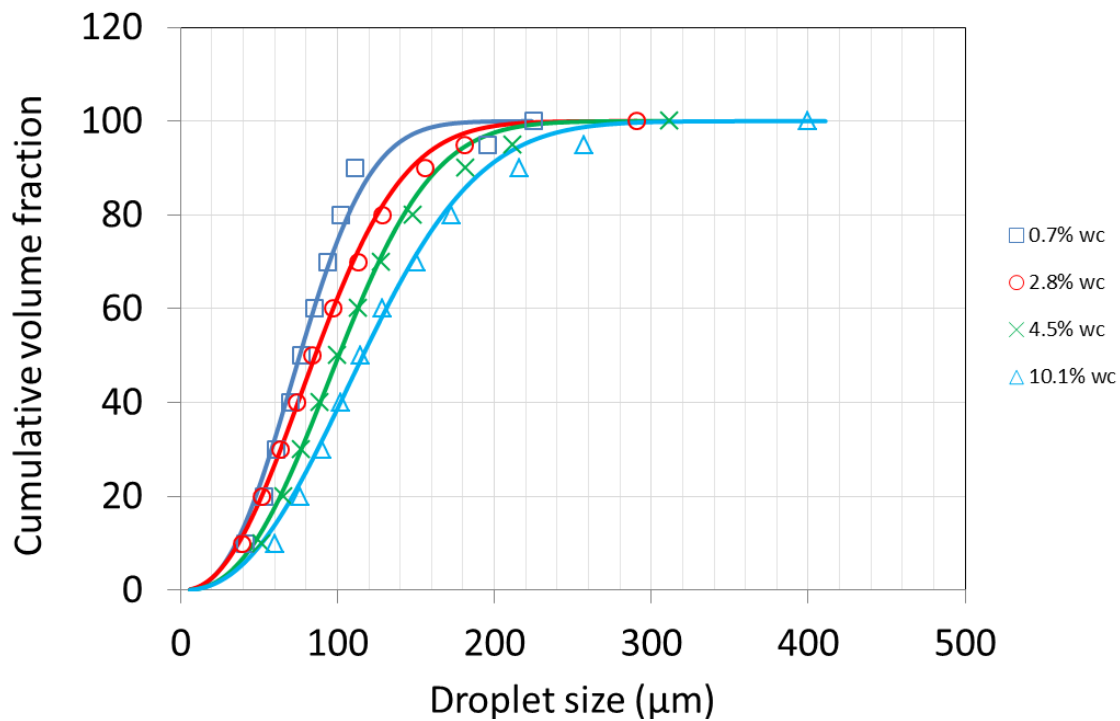


Figure 64. Effect of the water cut on the measured droplet size distribution at 122 *Watt/kg* turbulent dissipation rate – Standard horizontal pipe with mixing valve configuration.

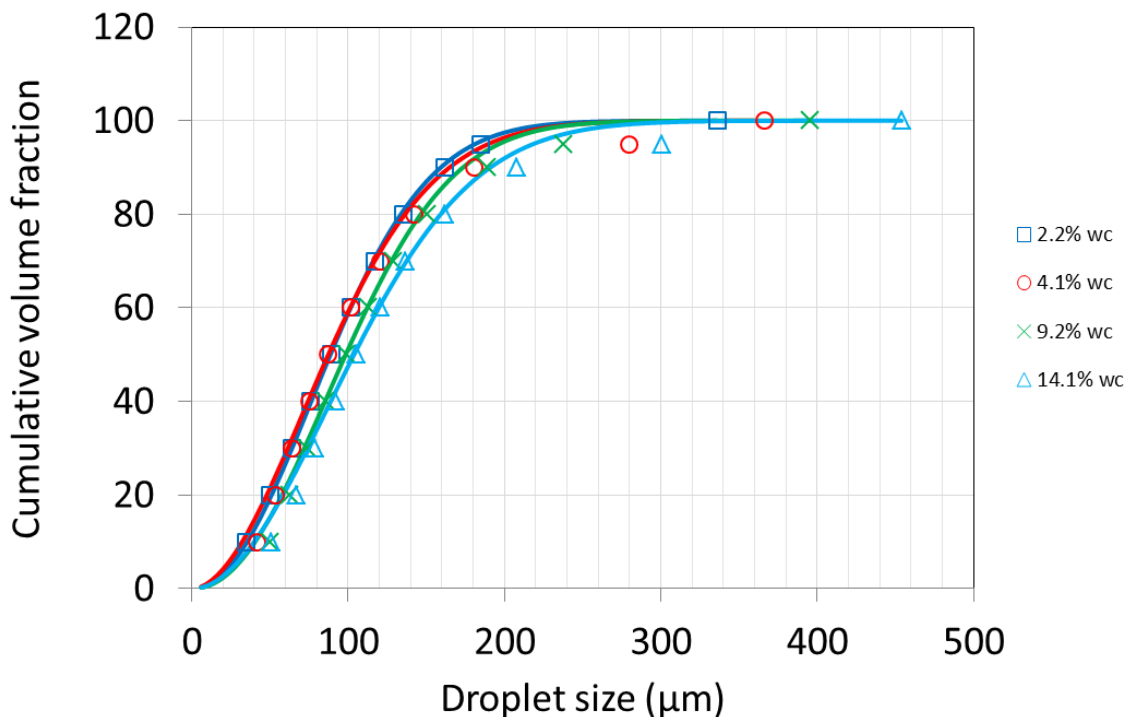


Figure 65. Effect of the water cut on the measured droplet size distribution at 220 *Watt/kg* turbulent dissipation rate – Standard horizontal pipe with mixing valve configuration.

6.2.2 Summary of results obtained with the Doughnut cell

Similarly to the previous section, the experimental cumulative volume distributions, obtained in the doughnut cell, are plotted with the fitted Rosin-Rammler correlation. The effect of turbulent dissipation rate is shown in Figure 66, for 5% water cut, and Figure 67, for 10% water cut, while the effect of water cut is shown in Figure 68, for 2 *Watt/kg*, and Figure 69, for 6 *Watt/kg*. The results are very similar to the previous section (standard pipe with mixing valve). The distribution profiles are shifted rightward and droplet size increases as the turbulent dissipation rate decreases and as the water cut increases.

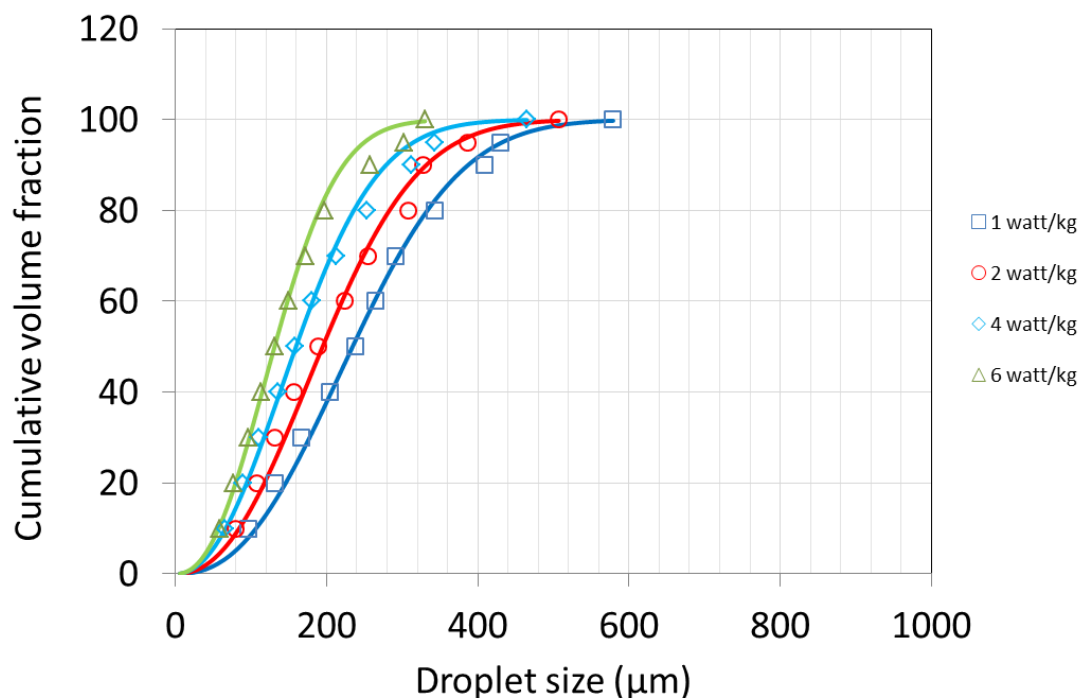


Figure 66. Effect of energy dissipation rate on the measured droplet size distribution at 5% average water cut – Doughnut cell configuration.

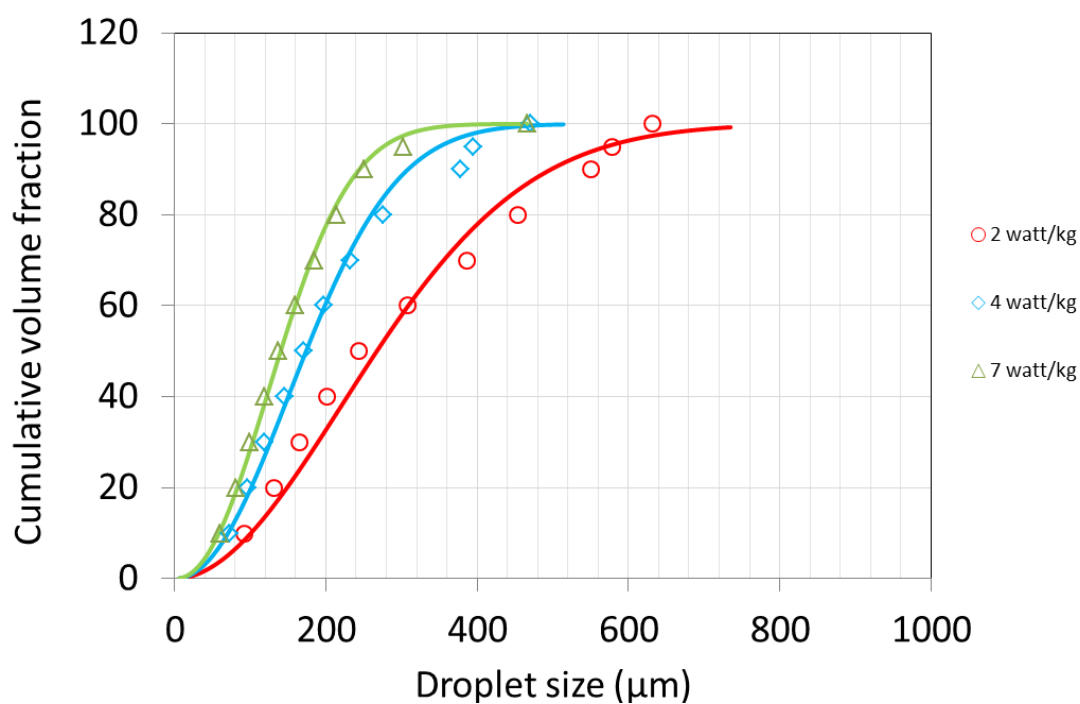


Figure 67. Effect of the energy dissipation rate on the measured droplet size distribution at 10% average water cut – Doughnut cell configuration.

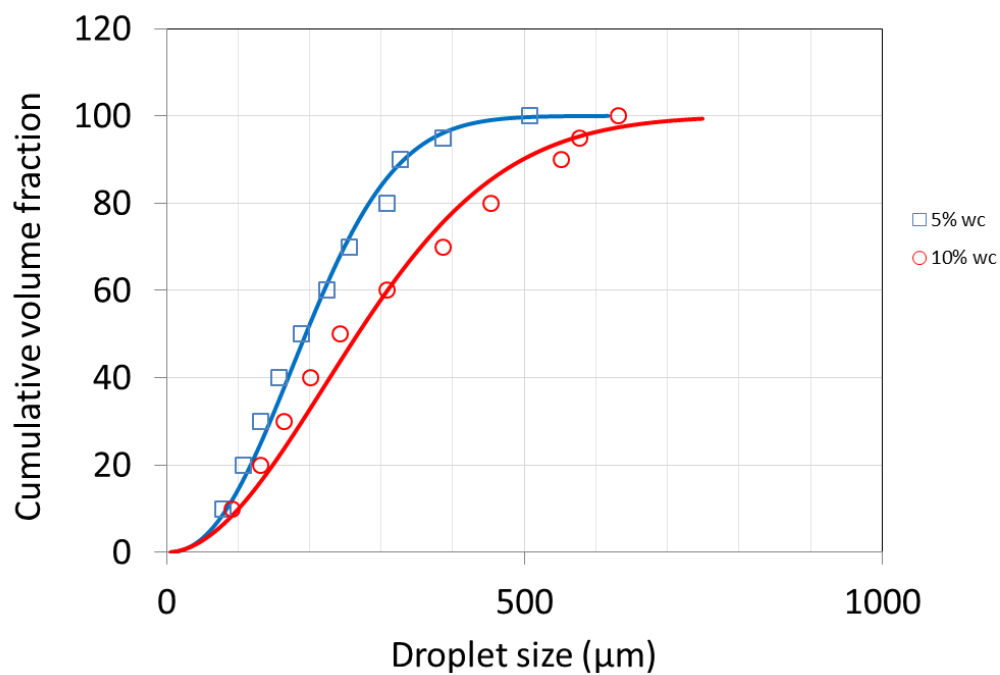


Figure 68. Effect of the water cut on the measured droplet size distribution at 2 *Watt/kg* turbulent dissipation rate – Doughnut cell configuration.

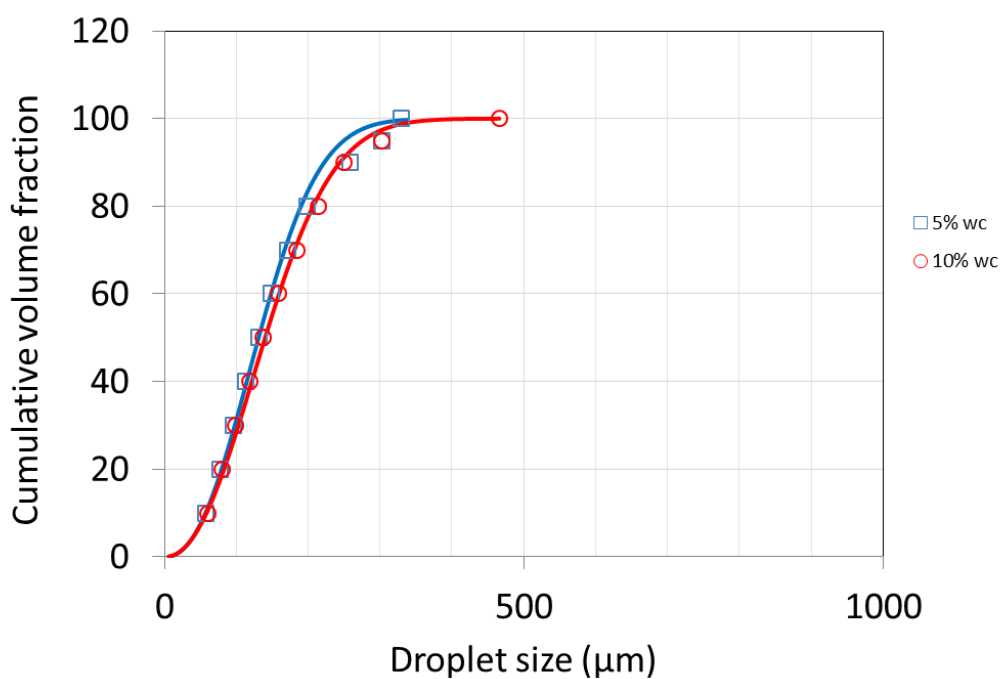


Figure 69. Effect of the water cut on the measured droplet size distribution at 6 *Watt/kg* turbulent dissipation rate – Doughnut cell configuration.

6.2.3 Summary of results obtained with the standard pipe

Finally, the presentation of the experimental results is repeated for the standard pipe flow configuration. The effect of turbulent dissipation rate is shown in Figure 70, for 1% water cut, while the effect of water cut is shown in Figure 71 for 0.6 *Watt/kg* and Figure 72 for 1.1 *Watt/kg*. The same overall trend as in the standard pipe flow with mixing valve and the doughnut cell configurations are observed. The distribution profiles are shifted rightward and droplet size increases as the turbulent dissipation rate decreases and as the water cut increases.

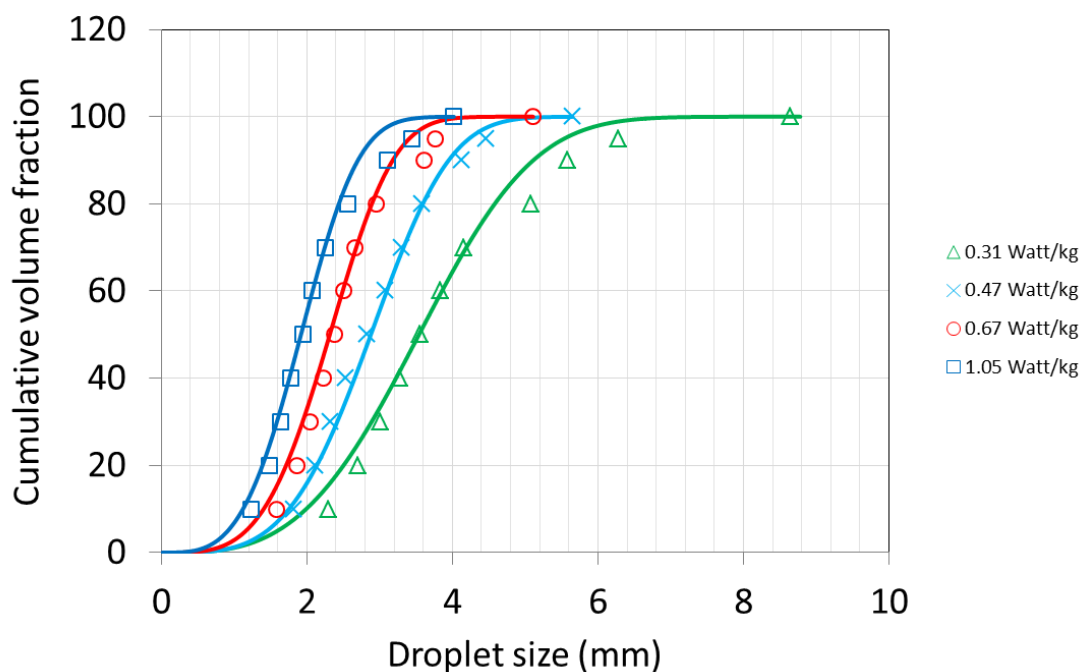


Figure 70. Effect of energy dissipation rate on the measured droplet size distribution at 1% average water cut – Horizontal standard pipe flow configuration.

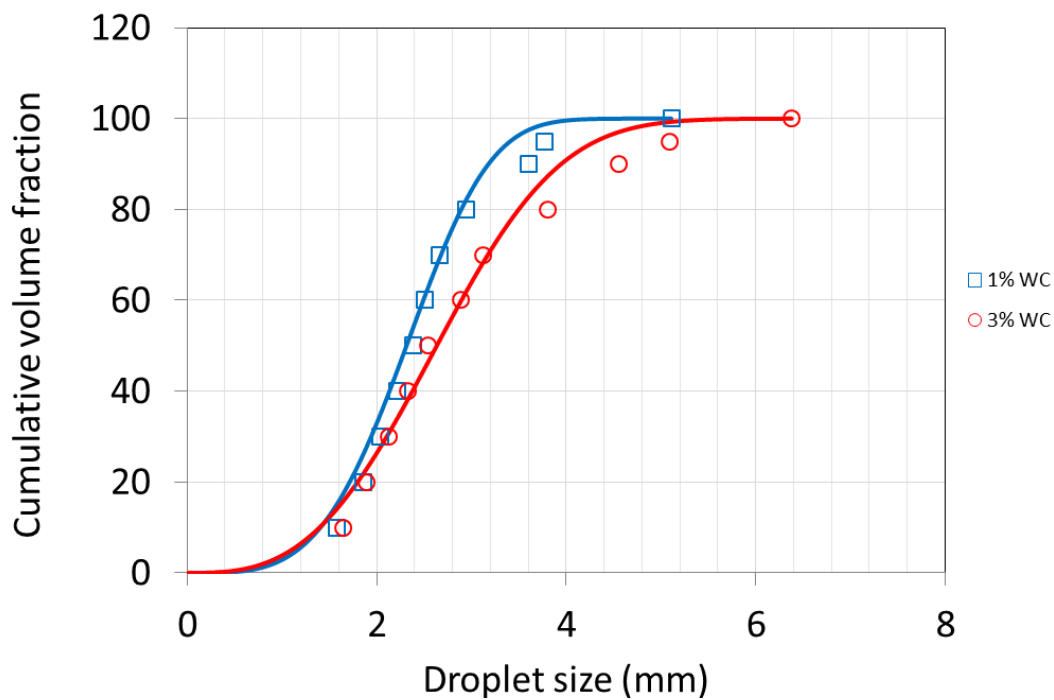


Figure 71. Effect of the water cut on the measured droplet size distribution at 0.6 Watt/kg turbulent dissipation rate - Horizontal standard pipe flow configuration.

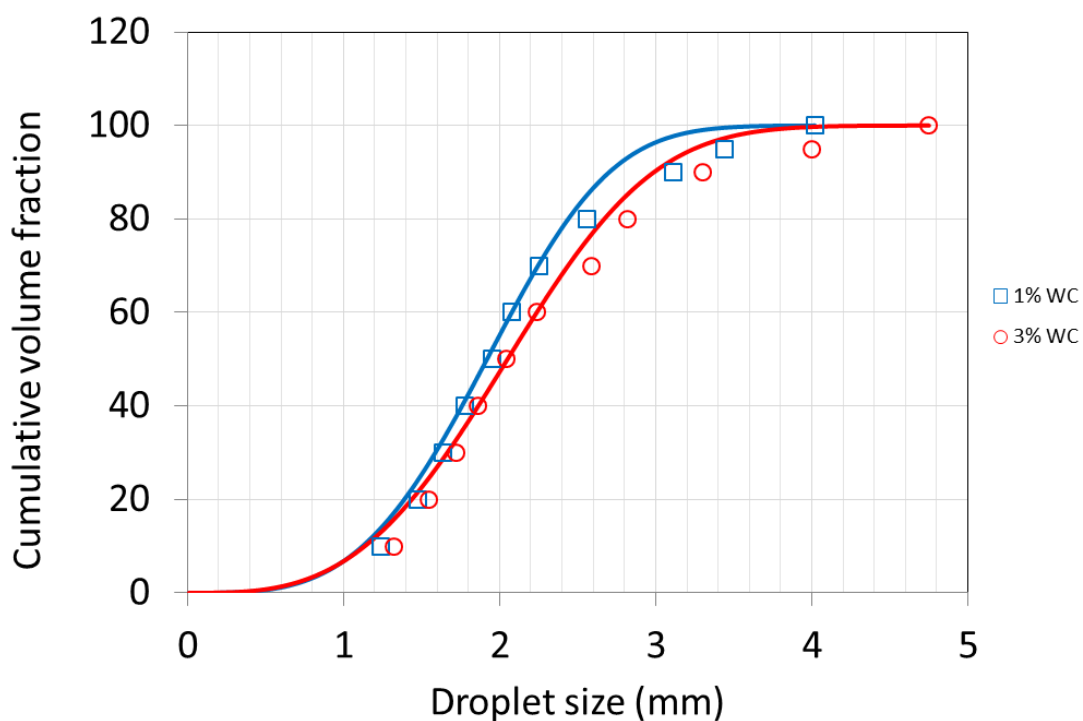


Figure 72. Effect of the water cut on the measured droplet size at 1.1 Watt/kg turbulent dissipation rate - Horizontal standard pipe flow.

6.2.4 Analysis of the Rosin-Rammler distribution parameters

This chapter investigates the effect of operating conditions on two parameters, $n(-)$ and $d^*(\mu\text{m})$ in order to extract trends or correlations that would permit their predictions. The results presented in the previous chapters and obtained in three different experimental setups are combined. Details on the values of $n(-)$ and $d_{63}(\mu\text{m})$ selected for each distribution can be found in Appendix II.

The effect of turbulent energy dissipation rate and water cut on the parameter $n(-)$ are presented in Figure 73 and Figure 74, respectively. It is interesting to notice that when considering data from the “standard pipe with valve” and the “doughnut cell” configuration, the value of $n(-)$ seems to be relatively independent of both dissipation rate and water cut. In these conditions $n(-)$ varies from 1.6 to 3.0. However, the values of $n(-)$ fitted from the “standard pipe” configuration present clear outliers since $n(-)$ varies from 2.9 to 3.9. The fact that of $n(-)$ seems to be distinctively different in the “standard pipe” configuration infers that the relative effect of droplet breakup and coalescence could be significant, as it was determined for the prediction of maximum droplet sizes.

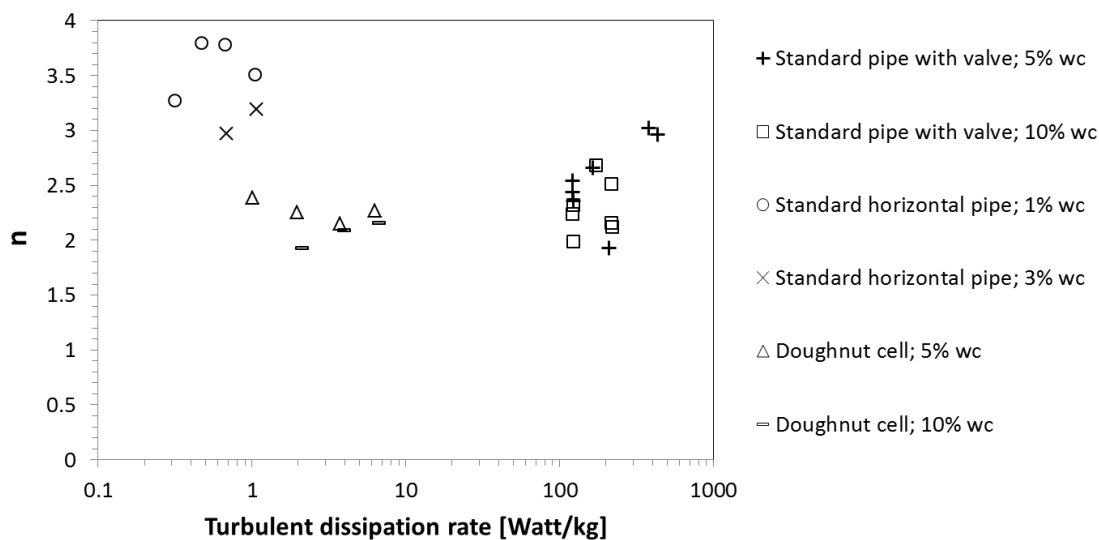


Figure 73. Effect of turbulent dissipation rate on the Rosin-Rammler parameter n .

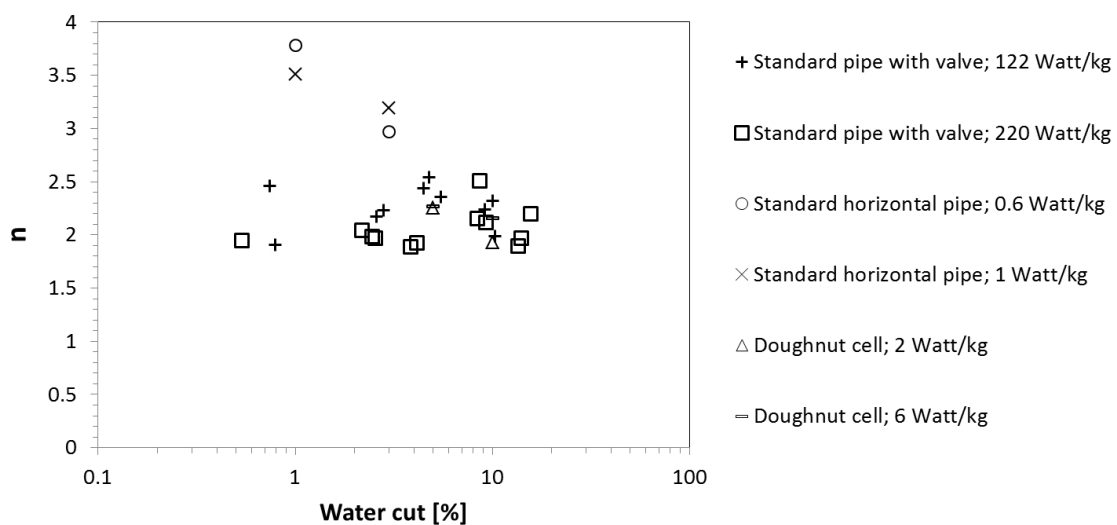


Figure 74. Effect of water cut on the Rosin-Rammler parameter n .

The same exercise is repeated for d^* (μm) which is a parameter directly measured during the experiments since $d^* = d_{63}$. The effect of water cut and turbulent energy dissipation rate on d_{63} (μm) are presented in Figure 75 and Figure 76, respectively. The

value of $d_{63}(\mu\text{m})$ seems to slightly increase as water cut increases and considerably decrease as turbulent dissipation rate increases. The same behavior was observed for the prediction of maximum droplet sizes although the effect of water cut was more pronounced.. The measured value of $d_{63}(\mu\text{m})$ varies from 88 to 154 μm for “standard pipe with valve” configuration and from 158 to 274 μm for “doughnut cell” configuration. Nevertheless, the value of $d_{63}(\mu\text{m})$ measured from the “standard pipe” configuration is from 2331 to 4024 μm . The fact that the value of $d_{63}(\mu\text{m})$ seems to be distinctively different in the “standard pipe” configuration infers again that the relative effect of droplet breakup and coalescence could be significant.

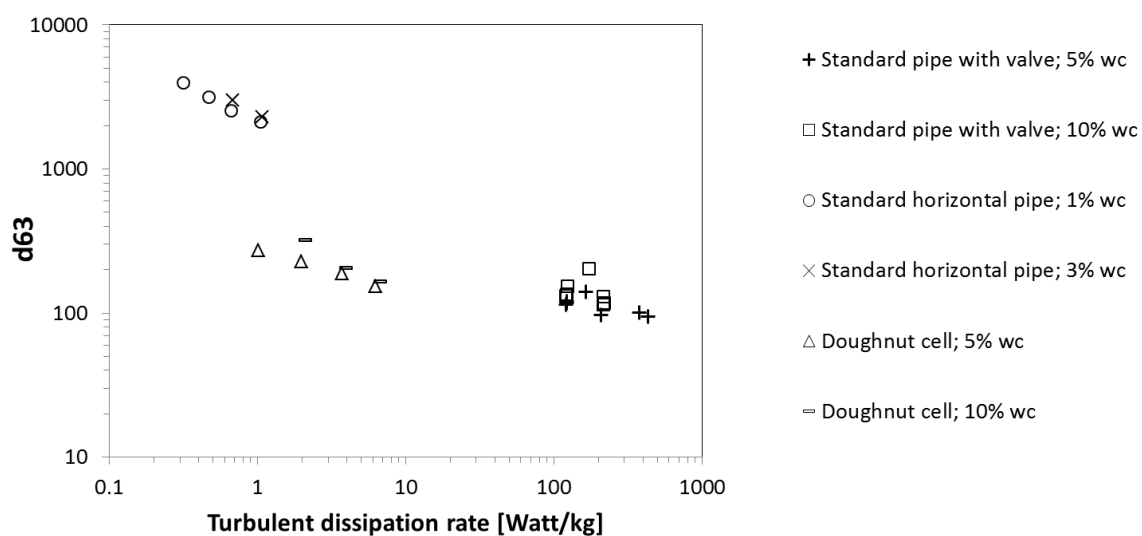


Figure 75. Effect of turbulent dissipation rate on the Rosin-Rammler parameter d_{63} (μm).

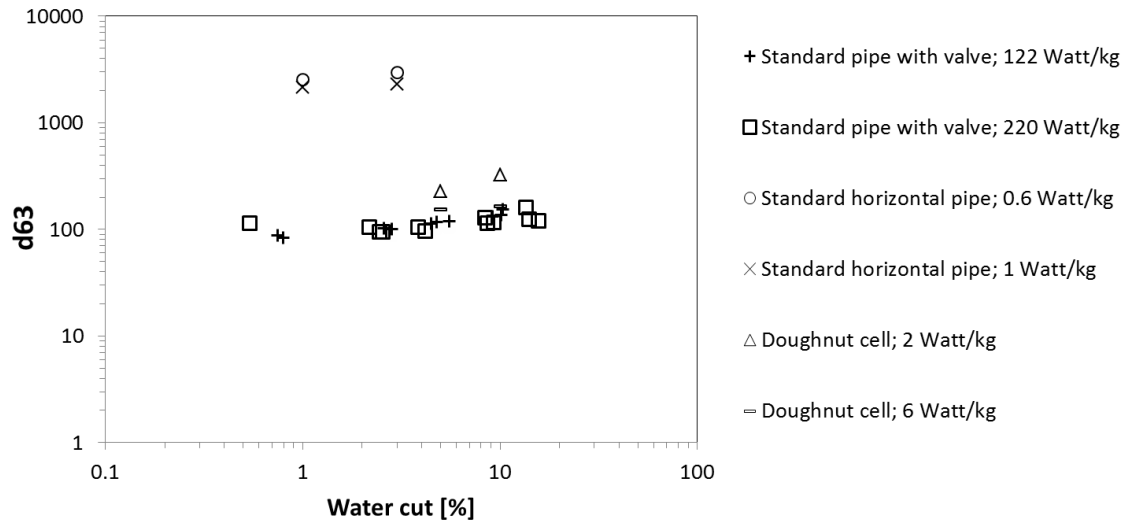


Figure 76. Effect of water cut on the Rosin-Rammler parameter d_{63} (μm).

Since a prediction model for maximum droplet size d_{max} (μm) has already been developed, it is convenient now to introduce the non-dimensional ratio of d_{max} (μm) to d_{63} (μm). Developing a correlation representing the effect of operating parameters on this ratio (d_{max}/d_{63}) would enable the determination of d_{63} (μm) from d_{max} (μm), followed by the determination of the entire droplet size distribution using the Roslin-Rammler equation. Several studies have proposed very similar approaches by investigating the effect of flow properties on either the ratio of the maximum droplet size d_{max} (μm) to droplet sauter mean diameter (SMD) (d_{max}/SMD) or the ratio of maximum droplet size to the mean droplet size d_{50} (μm) (d_{max}/d_{50}) [8], [9], [30]. The (d_{max}/d_{63}) ratio is chosen here simply because d_{max} can be predicted with the ICMT model and since d_{63} is an input of the Rosin-Rammler correlation. This ratio can be either calculated using the measured d_{max} , which can be affected by large measurement

errors, or the predicted d_{max} , which is believed to be more coherent as long as coalescence is not dominant.

The effects of turbulent energy dissipation rate and water cut on (d_{max}/d_{63}) , using measured d_{max} (μm), are presented in Figure 77 and Figure 78. In this case, the ratio (d_{max}/d_{63}) varies from 1.6 to 3.6 for “standard pipe with valve” and “doughnut cell” configurations, from 2.1 to 4.3 for “standard pipe with valve” configuration. There is no clear effect of the experimental setup configuration. The ratio (d_{max}/d_{63}) seems to increase as turbulent dissipation increases while no effect of the water cut could be identified since a lot of scatter can be observed in general.

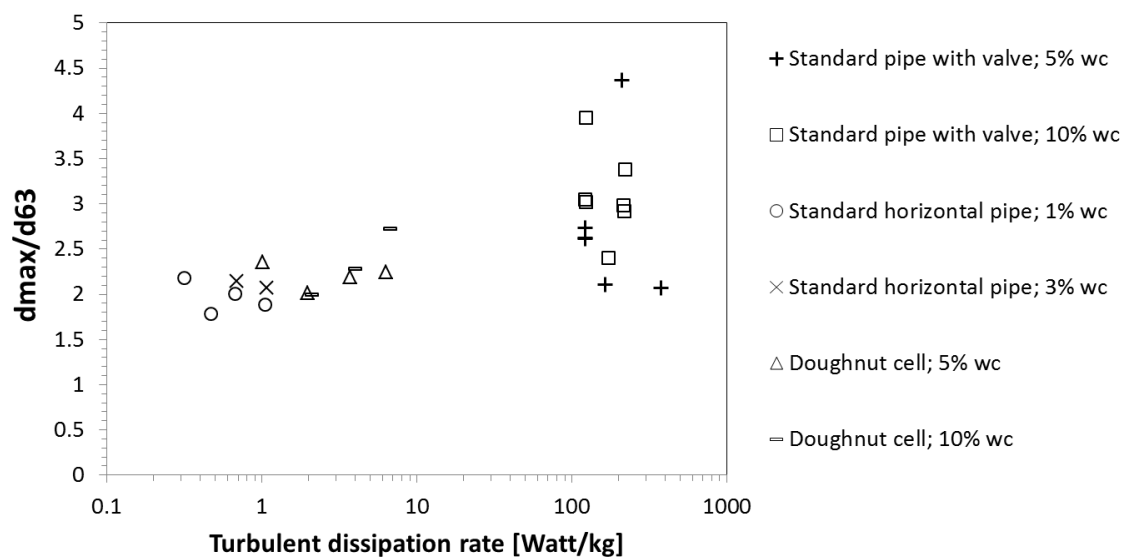


Figure 77. Effect of turbulent dissipation rate on the Rosin-Rammler parameter ratio d_{max}/d_{63} - measured d_{max} .

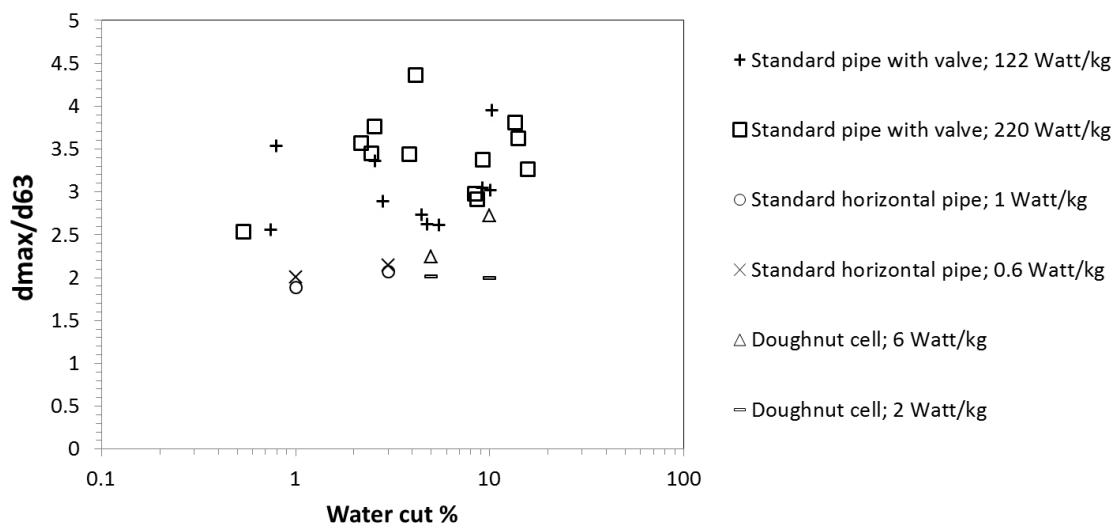


Figure 78. Effect of water cut on the Rosin-Rammler parameter ratio d_{max}/d_{63} - measured d_{max} .

The effect of turbulent energy dissipation rate and water cut on the ratio (d_{max}/d_{63}), this time using the maximum droplet size predicted by the ICMT model, are presented in Figure 79 and Figure 80, respectively. The results are essential the same as for the previous paragraph. The ratio (d_{max}/d_{63}) seems to increase as turbulent dissipation increases. No dependence on water cut is found. However, the “standard pipe” configuration has low ratio (d_{max}/d_{63}) values around 0.92 to 1.1 which are not physically possible. This is due to the fact that ICMT model neglects the effect of coalescence on droplets which can cause an under prediction of maximum droplet size.

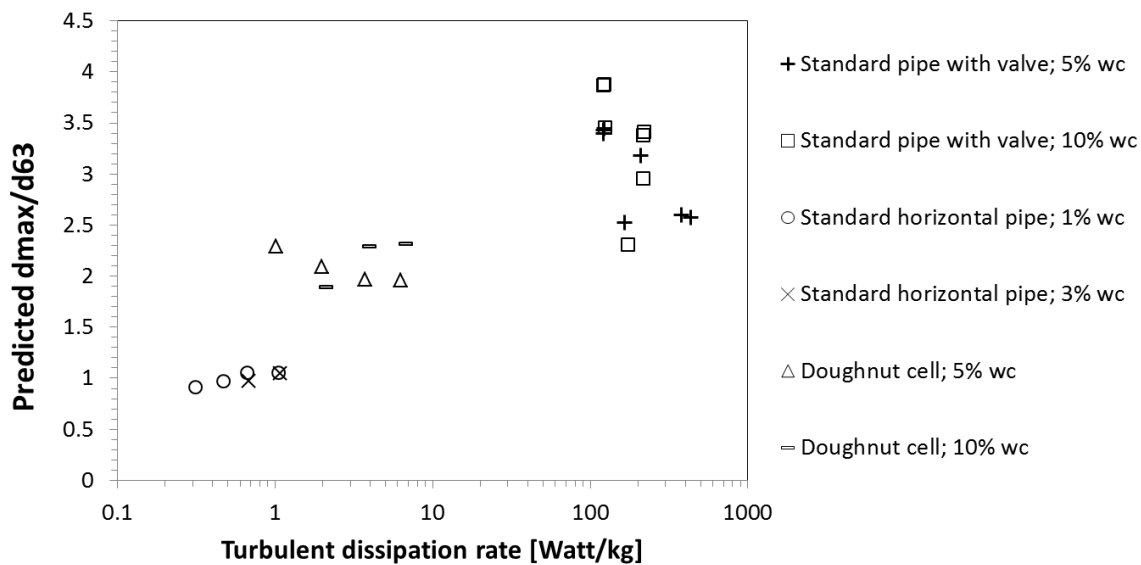


Figure 79. Effect of turbulent dissipation rate on the Rosin-Rammler parameter ratio d_{max}/d_{63} -predicted d_{max} .

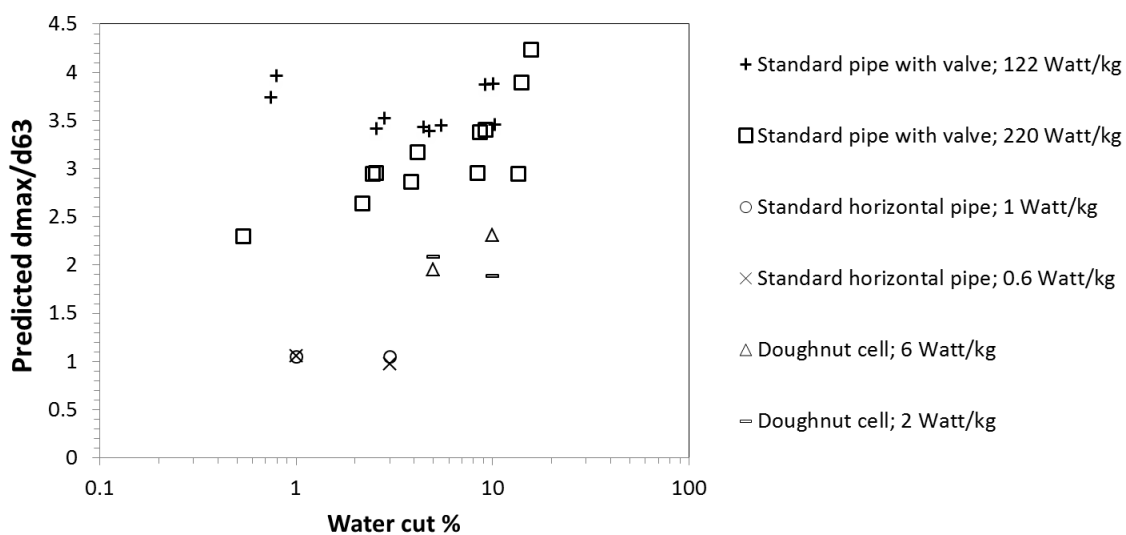


Figure 80. Effect of water cut on the Rosin-Rammler parameter ratio d_{max}/d_{63} -predicted d_{max} .

As inferred in the previous section, there could be a dependence of the relative droplet breakup and coalescence rates on the parameters $n(-)$ and $d_{63}(\mu m)$. These

parameters are consequently compared with the ratio of breakup rate to coalescence rates (g/Γ) in the following figures. Once again, the experimental data of “doughnut cell” configuration is not included in this section since the coalescence model is not valid for this setup[35]. The experimental data from Karabelas and Angeli [8], [9] are also included in this section. It is also worth mentioning that the relative ratio (g/Γ) is calculated using measured droplet sizes and this ratio (g/Γ) currently cannot be directly used for prediction since it relies on experimental measurements.

The parameter $n(-)$ is plotted as a function of the ratio of breakup rate to coalescence rate (g/Γ) in Figure 81. The parameter $n(-)$ clearly decreases as the ratio g/Γ increases.

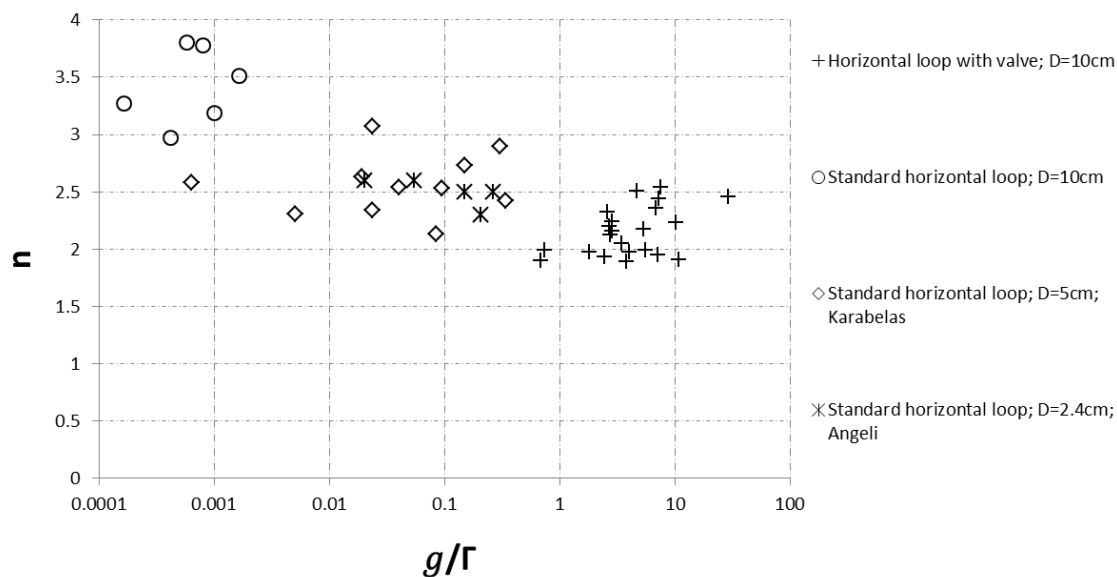


Figure 81. Effect of ratio of breakup rate to coalescence rate on the Rosin-Rammler parameter n

Similarly, the parameter $d_{63}(\mu\text{m})$ is plotted in Figure 82 as a function of the ratio of breakup rate to coalescence rate (g/Γ). It shows a clear relationship that $d_{63}(\mu\text{m})$ decreases as $g/\Gamma(-)$ increases. It is worth mentioning that the log-log plot tends to mask the extent of the data scatter.

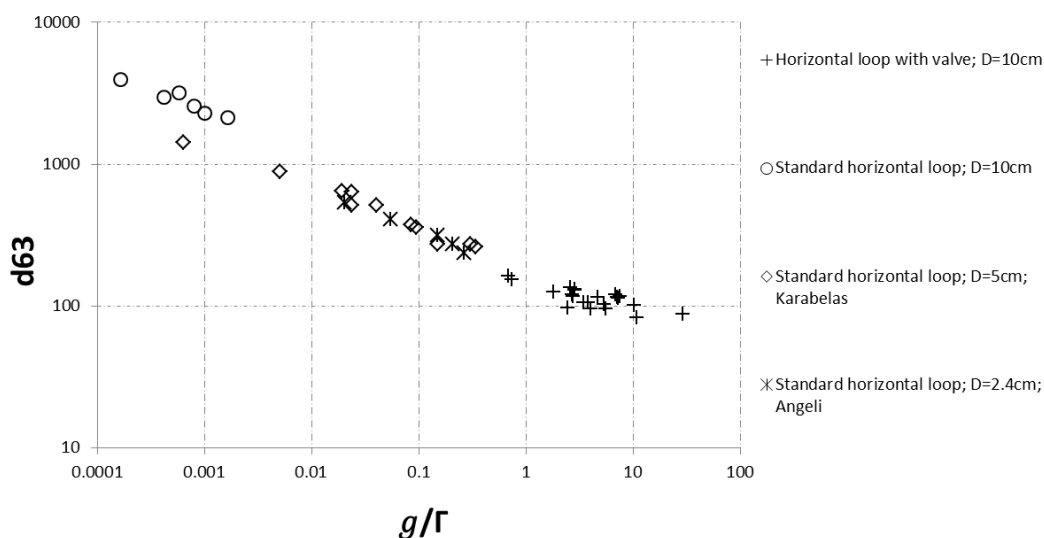


Figure 82. Effect of ratio of breakup rate to coalescence rate on the Rosin-Rammler parameter $d_{63}(\mu\text{m})$.

Next, the effect of the ratio of breakup rate to coalescence rate (g/Γ) on the ratio of measured maximum droplet size $d_{max}(\mu\text{m})$ to parameter $d_{63}(\mu\text{m})$ (d_{max}/d_{63}) is shown in Figure 83. Although the results are very scattered, a distinctive upward trend can be identified.

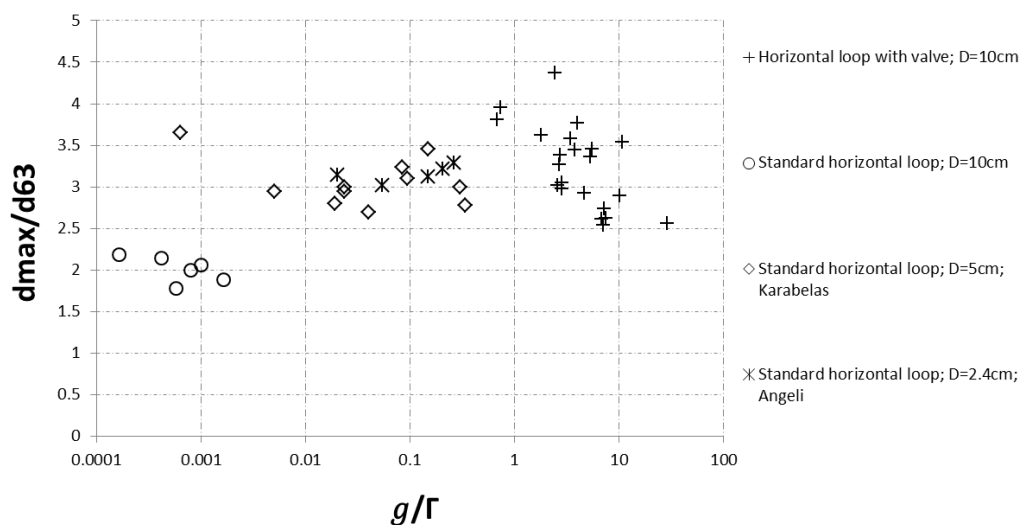


Figure 83. Effect of ratio of breakup rate to coalescence rate on the Rosin-Rammler parameter ratio d_{max}/d_{63} -measured d_{max} .

Finally, the effect of the ratio of breakup rate to coalescence rate (g/Γ) on the ratio of predicted maximum droplet size d_{max} (μm) to parameter d_{63} (μm) (d_{max}/d_{63}) is shown in Figure 84. The d_{max} (μm) is predicted using ICMT maximum droplet size model. The droplet size ratio d_{max}/d_{63} also increases as g/Γ increases. The “standard pipe” configuration shows ratio (d_{max}/d_{63}) values around or below 1 due to the fact that ICMT model does not take droplet coalescence into account, leading to a under prediction of maximum droplet size.

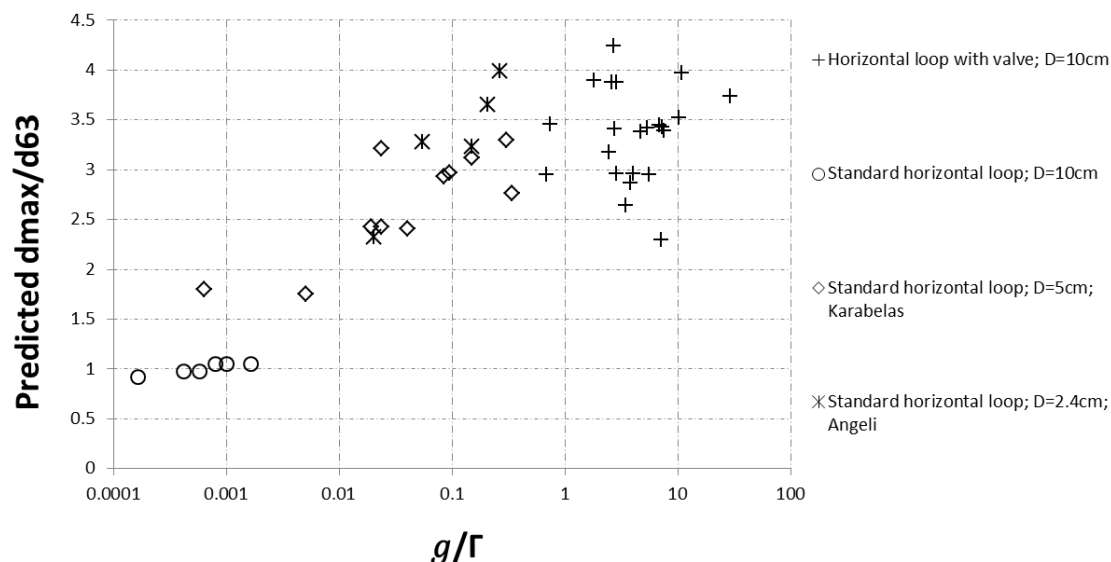


Figure 84. Effect of ratio of breakup rate to coalescence rate on the Rosin-Rammler parameter d_{max}/d_{63} -predicted d_{max} .

In summary, the value of $n(-)$ is mostly independent of both dissipation rate and water cut while the value of $d_{63}(\mu\text{m})$ seems to be mainly affected by the turbulent dissipation rate and only slightly influenced by the water cut. The droplet size ratio (d_{max}/d_{63}), calculated using either the measured or predicted d_{max} , seems to increase as turbulent dissipation increases while there is no clear effect of water cut.

However, clearer trends appear when plotting the parameters versus the ratio of breakup rate to coalescence rate (g/Γ). The parameters $n(-)$ and $d_{63}(\mu\text{m})$ seem to increase as (g/Γ) increases while the ratio d_{max}/d_{63} shows the opposite trend. Consequently, future models should take into account the effect of droplet breakup and coalescence in order to improve the accuracy of the parameters needed for the Rosin-Rammler equation. It is not the intent of the present work to develop such correlations although efforts were made to develop overall trends.

6.2.5 Local water concentration calculation using Rosin-Rammler equation

This last section is an effort to relate the determination of droplet size distribution to the main industrial goal which is to predict water wetting. The droplet size distribution is used to calculate local water concentration which is in turn compared to the inversion point, as explain in chapter 2.1.2. The objective here is to evaluate the impact of the relative inaccuracy of the Rosin-Rammler parameters $n(-)$ and (d_{max}/d_{63}) on the prediction of local water concentration.

An unique set of experimental data, reported from water-in-crude oil non-uniform dispersion in “standard pipe” configuration [58], is used. This set of data displays experimental values of water cut along the cross section of the pipe section.

Experimental local water concentrations are compared with predicted local water concentration calculated with the Rosin-Rammler equation, considering a range of $n(-)$ and (d_{max}/d_{63}) .

The Rosin-Rammler parameter value of $n(-)$ is set from 1.6 to 3.0 and the ratio value of d_{max}/d_{63} is chosen from 1.6 to 4.0. These ranges are obtained from the “standard pipe with valve” and the “doughnut cell” configuration experiments which share a similar range of the ratio of breakup rate to coalescence rate (g/Γ) with the water-in-crude oil dispersion experimental data selected for this comparison. In addition, $d_{max}(\mu\text{m})$ is calculated using ICMT maximum droplet size model.

The effect of Rosin-Rammler parameter $n(-)$ and the ratio of d_{max}/d_{63} on the local water concentration predictions are presented in Figure 85 and Figure 86, respectively. At a constant droplet size ratio ($d_{max}/d_{63} = 1.6$), the local water

concentration profile is barely affected by the change of parameter $n(-)$ (from 1.6 to 3). However, when the ratio (d_{max}/d_{63}) changes from 1.6 to 4 at constant $n(-) = 3$, the predicted profile displays a considerable shift and fails to predict the experimental local water concentration. In this case, the variation of parameter $n(-)$ value does not affect the local water concentration prediction accuracy as much as the variation of the ratio (d_{max}/d_{63}) does. This infers that a constant value of $n(-)$ can be safely chosen. However, the same cannot be said for the ratio d_{max}/d_{63} , which seems to relate more strongly on the effect of droplet breakup and coalescence.

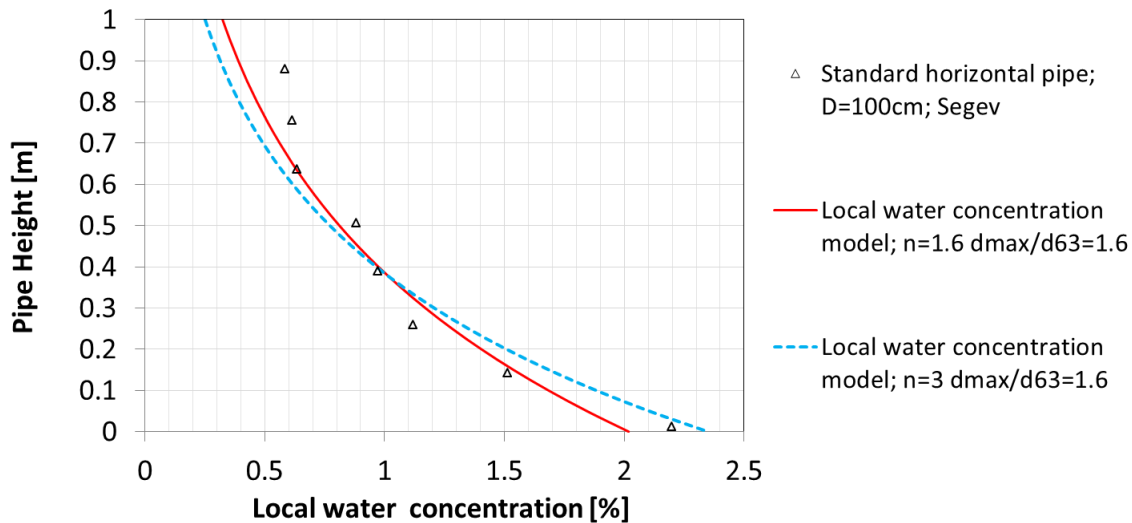


Figure 85. Effect of Rosin-Rammler parameter $n(-)$ on local water concentration prediction.

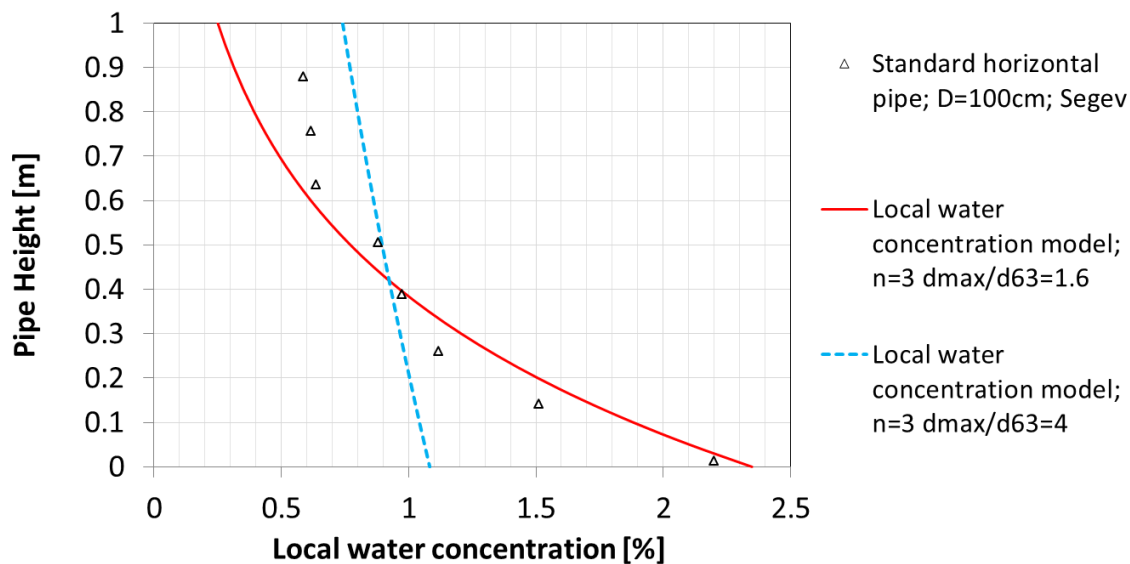


Figure 86. Effect of droplet size ratio (d_{max}/d_{63}) on local water concentration prediction.

Chapter 7 Conclusions and Recommendations

The primary objective of this work was to collect experimental data of maximum droplet size and droplet size distribution in water-in-oil dispersion for a wide range of flow conditions and fluid properties and to compare them with the current model predictions in order to identify gaps in the current understanding of the mechanisms and propose a way forward.

Three main hypotheses were formulated:

1. A single comprehensive model covering maximum droplet size predictions for both dilute and dense dispersion can be developed and validated over a wide range of flow conditions and fluid properties.
2. The assumption that droplet coalescence can be neglected is not valid in all cases and can explain discrepancies between maximum droplet size predictions and experimental measurements.
3. A mechanistic approach can be adopted to predict droplet size distributions based on flow conditions and fluid properties.

Experiments were completed at atmosphere pressure and ambient temperature in three different configurations: standard pipe with mixing valve, doughnut cell and standard pipe. An oil/water mixture comprised of DI water and Isopar V (oil density: 808 kg/m^3) was selected.

The range of the investigated parameters was 1% to 20% for the water volume fraction, 5 and 50 mN/m for the water-oil interfacial tension and 0.3 to 430 $Watt/kg$ for the turbulent dissipation rate.

7.1 Maximum droplet size

The experimental maximum droplet size data were compared with Hinze model (for dilute dispersion), Brauner model (for dilute dispersion) predictions. Both models showed relatively accurate predictions of maximum droplet size as long as the effect of droplet coalescence could be neglected. The maximum droplet size $d_{max}(\mu m)$ increased as water cut increased and decreased as turbulent dissipation rate increased. The data were also used to validate an improved version of the maximum droplet size model, ICMT model, which showed superior accuracy and precision against experimental data developed both in this study and in the literature. The ICMT model constitutes a valuable improvement of the actual modeling approach as it unifies predictions of maximum droplet sizes in both dilute and dense dispersion, validating hypothesis #1.

However, all three models consistently under predicted the maximum droplet size for “standard pipe” experiments where droplet coalescence should not have been neglected. The effect of droplet coalescence was clearly identified as the main reason for prediction errors. This was achieved by estimated the relative rate of droplet breakup and coalescence and investigating its influence on the experimental maximum droplet size. This confirmed hypothesis #2. Future maximum droplet size models could take coalescence into account in order to extend the domain of validity of model predictions.

7.2 Droplet size distribution conclusion

The experimental droplet size distribution data were fitted using the Rosin-Rammler equation and an effort was made to relate the fitted parameters, $n(-)$ and $d_{63}(\mu m)$, to the flow properties in order to develop physical correlations which could be

used for the prediction of droplet size distributions. The analysis of the results showed that the parameter value of $n(-)$ had no dependency on either turbulent dissipation rate or water cut. The value of parameter $d_{63}(\mu m)$ showed a slight dependency on the water cut but considerably decreased as turbulent dissipation rate increased. The ratio d_{max}/d_{63} was determined as a convenient parameter to use for the prediction of droplet distribution since d_{63} could then be directly calculated from the prediction of d_{max} . This ratio was found to increase with turbulent dissipation but no clear effect of water cut could be found. Overall, no clear correlation could be found between the parameters of the Rosin-Rammler equation and the flow characteristics although trends were definitely highlighted. It was found that choosing a value of $n(-)$ between 1.6 and 3 did not affect significantly the prediction of droplet size distribution. However, the d_{max}/d_{63} proved to be a lot more sensitive to operating conditions and the development of a predictive correlation remains elusive. However, both Rosin-Rammler parameters $n(-)$ and $d_{63}(\mu m)$ showed a clearer dependency on the relative ratio of droplet breakup rate and coalescence rate. Consequently, hypothesis #3 could be verified. The incorporation of this ration in a predictive correlation could constitute a significant improvement towards the development of predictive droplet size distribution tools.

7.3 Recommendation

Due to the low shutter speed of the camera, the current “standard pipe” configuration can only be used in conditions up to 2 *m/s* mixture velocity at 1.1 *Watt/kg* turbulent dissipation rate. A camera with higher shutter speed (1/10000 sec) is recommended to extend the measurement of droplet size to conditions ranging from 0

to 4 m/s mixture velocity which is the maximum velocity that can be attained in the “standard pipe” setup. In addition, the current “doughnut cell” setup can only capture droplet sizes up to 1 mm due to the limited field of view of PVM camera. A camera with large field of view and strong illumination source can be used to extend the measurement range to larger droplet sizes.

Droplet population balance equation (PBE) is recommended for the prediction of droplet size distribution. The formulations of PBE depend on the accurate prediction of droplet breakup and coalescence rates. Here, the coalescence rate prediction can be improved by using “Film drainage model”, Chapter 2.3.2.2.2, by obtaining the experimental initial film thickness $h_i(m)$ and the critical film thickness $h_f(m)$ for accurate coalescence efficiency calculation.

References:

- [1] K. E. Kee, S. Richter, M. Babic, S. Nestic, and others, "Flow Patterns and Water Wetting in Oil-Water Two Phase Flow—A Flow Loop Study," CORROSION/2014, paper no. 4086.
- [2] Y.-S. Choi, S. Nestic, and S. Ling, "Effect of H₂S on the CO₂ corrosion of carbon steel in acidic solutions," *Electrochimica Acta*, vol. 56, no. 4, pp. 1752–1760, 2011.
- [3] R. W. Revie and H. H. Uhlig, *Corrosion and corrosion control: an introduction to corrosion science and engineering*, Hoboken. New Jersey: John Wiley & Sons, Inc, 2008.
- [4] J. L. Trallero, *Oil-water flow patterns in horizontal pipes*. University of Tulsa Fluid Flow Projects, 1995.
- [5] M. J. H. Simmons and B. J. Azzopardi, "Drop size distributions in dispersed liquid–liquid pipe flow," *Int. J. Multiph. Flow*, vol. 27, no. 5, pp. 843–859, 2001.
- [6] W. a. S. Kumara, B. M. Halvorsen, and M. C. Melaaen, "Pressure drop, flow pattern and local water volume fraction measurements of oil–water flow in pipes," *Meas. Sci. Technol.*, vol. 20, no. 11, p. 114004, 2009.
- [7] J. Cai, C. Li, X. Tang, F. Ayello, S. Richter, and S. Nestic, "Experimental study of water wetting in oil–water two phase flow—Horizontal flow of model oil," *Chem. Eng. Sci.*, vol. 73, pp. 334–344, 2012.
- [8] A. J. Karabelas, "Droplet size spectra generated in turbulent pipe flow of dilute liquid/liquid dispersions," *AIChE J.*, vol. 24, no. 2, pp. 170–180, 1978.
- [9] P. Angeli and G. F. Hewitt, "Drop size distributions in horizontal oil-water dispersed flows," *Chem. Eng. Sci.*, vol. 55, no. 16, pp. 3133–3143, 2000.
- [10] E. L. Hanzevack and G. D. Demetriou, "Effect of velocity and pipeline configuration on dispersion in turbulent hydrocarbon-water flow using laser image processing," *Int. J. Multiph. Flow*, vol. 15, no. 6, pp. 985–996, 1989.
- [11] J. Kubie and G. C. Gardner, "Drop sizes and drop dispersion in straight horizontal tubes and in helical coils," *Chem. Eng. Sci.*, vol. 32, no. 2, pp. 195–202, 1977.
- [12] M. A. Vielma, S. Atmaca, C. Sarica, H.-Q. Zhang, and others, "Characterization of oil/water flows in horizontal pipes," *SPE Proj. Facil. Constr.*, vol. 3, no. 04, pp. 1–21, 2008.
- [13] C. A. Coualoglou and L. L. Tavlarides, "Description of interaction processes in agitated liquid-liquid dispersions," *Chem. Eng. Sci.*, vol. 32, no. 11, pp. 1289–1297, 1977.
- [14] L. Vafajoo, K. Ganjian, and M. Fattahi, "Influence of key parameters on crude oil desalting: An experimental and theoretical study," *J. Pet. Sci. Eng.*, vol. 90, pp. 107–111, 2012.
- [15] D. Barnea, "Transition from annular flow and from dispersed bubble flow—unified models for the whole range of pipe inclinations," *Int. J. Multiph. Flow*, vol. 12, no. 5, pp. 733–744, 1986.
- [16] N. Brauner and A. Ullmann, "Modeling of phase inversion phenomenon in two-phase pipe flows," *Int. J. Multiph. Flow*, vol. 28, no. 7, pp. 1177–1204, 2002.
- [17] N. Brauner, "The prediction of dispersed flows boundaries in liquid–liquid and gas–liquid systems," *Int. J. Multiph. Flow*, vol. 27, no. 5, pp. 885–910, 2001.
- [18] J. O. Hinze, "Fundamentals of the hydrodynamic mechanism of splitting in dispersion processes," *AIChE J.*, vol. 1, no. 3, pp. 289–295, 1955.
- [19] R. Skartlien, E. Sollum, and H. Schumann, "Droplet size distributions in turbulent emulsions: breakup criteria and surfactant effects from direct numerical simulations," *J. Chem. Phys.*, vol. 139, no. 17, p. 174901, 2013.
- [20] R. A. Bagnold, "An approach to the sediment transport problem," *Gen. Phys. Geol. Surv. Prof Pap.*, 1966.

- [21] A. J. Karabelas, "Vertical distribution of dilute suspensions in turbulent pipe flow," *AIChE J.*, vol. 23, no. 4, pp. 426–434, 1977.
- [22] P. H. Clay, "The mechanism of emulsion formation in turbulent flow," *Proc. Sect. Sci.*, vol. 43, pp. 852–965, 1940.
- [23] S. B. Collins and J. G. Knudsen, "Drop-size distributions produced by turbulent pipe flow of immiscible liquids," *AIChE J.*, vol. 16, no. 6, pp. 1072–1080, 1970.
- [24] C. A. Sleicher, "Maximum stable drop size in turbulent flow," *AIChE J.*, vol. 8, no. 4, pp. 471–477, 1962.
- [25] B. F. Pots, S. D. Kapusta, R. C. John, M. J. J. Thomas, I. J. Rippon, T. S. Whitham, M. Girgis, and others, "Improvements on de Waard-Milliams corrosion prediction and applications to corrosion management," CORROSION/2002, paper no. 2235.
- [26] C. D. Adams, J. D. Garber, F. H. Walters, and C. Singh, "Verification of computer modeled tubing life predictions by field data," CORROSION/1993, paper no. 82.
- [27] C. De Waard and U. Lotz, "Prediction of CO₂ Corrosion of Carbon Steel," CORROSION/1993, paper no. 69.
- [28] D. Barnea, O. Shoham, and Y. Taitel, "Flow pattern transition for vertical downward two phase flow," *Chem. Eng. Sci.*, vol. 37, no. 5, pp. 741–744, 1982.
- [29] S. B. Collins and J. G. Knudsen, "Drop-size distributions produced by turbulent pipe flow of immiscible liquids," *AIChE J.*, vol. 16, no. 6, pp. 1072–1080, 1970.
- [30] K. E. Kee, "A Study of Flow Patterns and Surface Wetting in Gas-Oil-Water Flow," Ph.D dissertation, Ohio University, 2014.
- [31] L. Schiller and A. Naumann, "A drag coefficient correlation," *Vdi Ztg.*, vol. 77, no. 318, p. 51, 1935.
- [32] R. Byron Bird, Warren E. Stewart, Edwin N. Lightfoot, *Transport Phenomena*, Second edition. Wiley & Sons.
- [33] Y. Liao and D. Lucas, "A literature review on mechanisms and models for the coalescence process of fluid particles," *Chem. Eng. Sci.*, vol. 65, no. 10, pp. 2851–2864, 2010.
- [34] T. J. Jones, E. L. Neustadter, K. P. Whittingham, and others, "Water-in-crude oil emulsion stability and emulsion destabilization by chemical demulsifiers," *J. Can. Pet. Technol.*, vol. 17, no. 02, 1978.
- [35] J. E. Strassner, "Effect of pH on interfacial films and stability of crude oil-water emulsions," *J. Pet. Technol.*, vol. 20, no. 03, pp. 303–312, 1968.
- [36] D. E. Tambe and M. M. Sharma, "Factors controlling the stability of colloid-stabilized emulsions: I. An experimental investigation," *J. Colloid Interface Sci.*, vol. 157, no. 1, pp. 244–253, 1993.
- [37] S. Maas and M. Kraume, "Determination of breakage rates using single drop experiments," *Chem. Eng. Sci.*, vol. 70, pp. 146–164, 2012.
- [38] A. Chesters, "The modelling of coalescence processes in fluid-liquid dispersions: a review of current understanding," *Chem. Eng. Res. Des.*, vol. 69, no. A4, pp. 259–270, 1991.
- [39] R. Shinnar and J. M. Church, "Statistical theories of turbulence in predicting particle size in agitated dispersions," *Ind. Eng. Chem.*, vol. 52, no. 3, pp. 253–256, 1960.
- [40] S. K. Das, "Development of a coalescence model due to turbulence for the population balance equation," *Chem. Eng. Sci.*, vol. 137, pp. 22–30, 2015.
- [41] P. RosIN, "The laws governing the fineness of powdered coal," *J Inst Fuel*, vol. 7, pp. 29–36, 1933.
- [42] G. I. Taylor, "The formation of emulsions in definable fields of flow," *Proc. R. Soc. Lond. Ser. Contain. Pap. Math. Phys. Character*, pp. 501–523, 1934.

- [43] A. N. Kolmogorov, "On the breakage of drops in a turbulent flow," in *Dokl. Akad. Navk. SSSR*, 1949, vol. 66, pp. 825–828.
- [44] E. L. Paul, V. Atiemo-Obeng, and S. M. Kresta, *Handbook of industrial mixing: science and practice*. John Wiley & Sons, 2004.
- [45] W. Wang, W. Cheng, J. Duan, J. Gong, B. Hu, and P. Angeli, "Effect of dispersed holdup on drop size distribution in oil–water dispersions: Experimental observations and population balance modeling," *Chem. Eng. Sci.*, vol. 105, pp. 22–31, 2014.
- [46] M. J. Prince and H. W. Blanch, "Bubble coalescence and break-up in air-sparged bubble columns," *AIChE J.*, vol. 36, no. 10, pp. 1485–1499, 1990.
- [47] J. Y. Park and L. M. Blair, "The effect of coalescence on drop size distribution in an agitated liquid-liquid dispersion," *Chem. Eng. Sci.*, vol. 30, no. 9, pp. 1057–1064, 1975.
- [48] H. Sovova, "Breakage and coalescence of drops in a batch stirred vessel—II comparison of model and experiments," *Chem. Eng. Sci.*, vol. 36, no. 9, pp. 1567–1573, 1981.
- [49] A. Hasseine, A.-H. Meniai, M. B. Lehocine, and H.-J. Bart, "Assessment of drop coalescence and breakup for stirred extraction columns," *Chem. Eng. Technol.*, vol. 28, no. 5, pp. 552–560, 2005.
- [50] A. M. Kamp, A. K. Chesters, C. Colin, and J. Fabre, "Bubble coalescence in turbulent flows: a mechanistic model for turbulence-induced coalescence applied to microgravity bubbly pipe flow," *Int. J. Multiph. Flow*, vol. 27, no. 8, pp. 1363–1396, 2001.
- [51] K. Blake and L. Paolinelli, "CFD Study on doughnut cell single phase flow," Unpublished.
- [52] K. Blake, "Experimental Characterization and Modeling of Wettability and Modeling in Two Phase Oil/Water flow in the Doughnut Cell Apparatus," Unpublished.
- [53] M. Khatibi, "Experimental study on droplet size of dispersed oil-water flow," M.S thesis, Norwegian University of Science and Technology, 2013.
- [54] C.-Y. J. Hwang and R. Pal, "Pressure Losses in Globe and Gate Valves during Two-Phase Oil/Water Emulsion Flow," *Ind. Eng. Chem. Res.*, vol. 37, no. 2, pp. 636–642, 1998.
- [55] S. K. MacLeod, "Moisture determination using Karl Fischer titrations," *Anal. Chem.*, vol. 63, no. 10, p. 557A–566A, 1991.
- [56] H. Zuidema and G. Waters, "Ring Method for Determination of Interfacial Tension," *Ind. Eng. Chem. Anal. Ed.*, vol. 13, no. 5, pp. 312–313, 1941.
- [57] Luciano Paolinelli, "Effect of water content on maximum droplet size in oil-water dispersed turbulent pipe flow with mixing valve," Unpublished.
- [58] A. Segev, "Mechanistic model for estimating water dispersion in crude oil flow," American Institute of Chemical Engineers, New York, NY, Annual AIChE Meeting, paper no. 124a, 1985.
- [59] A. Saber, T. S. Lundström, and J. G. I. Hellström, "Turbulent Modulation in Particulate Flow: A Review of Critical Variables," *Engineering*, vol. 07, no. 10, pp. 597–609, 2015.
- [60] M. Mandø and L. Rosendahl, "On the motion of non-spherical particles at high Reynolds number," *Powder Technol.*, vol. 202, no. 1, pp. 1–13, 2010.
- [61] S. Geiss, A. Dreizler, Z. Stojanovic, M. Chrigui, A. Sadiki, and J. Janicka, "Investigation of turbulence modification in a non-reactive two-phase flow," *Exp. Fluids*, vol. 36, no. 2, pp. 344–354, 2004.
- [62] S. Elghobashi, "On predicting particle-laden turbulent flows," *Appl. Sci. Res.*, vol. 52, no. 4, pp. 309–329, 1994.

Appendix I: Turbulent Modulation

It has been reported that the presence of dispersed water droplets can also influence the behavior of the continuous phase and affect parameters characteristics of turbulent flow, such as the turbulent dissipation rate. This phenomenon is referred as turbulent modulation [59] and is often not included in droplet size or dissipation rate prediction models due to its inherent complexity. An effort is made here to characterize the parameters known to influence turbulent modulation and define operating conditions when its effect on turbulent flow characteristics is significant. Turbulent modulation is typically defined as depending on four dimensionless parameters: droplet Reynolds number, Stokes number, length scale, and dispersed phase volume fraction.

1 Droplet Reynolds number

The Droplet Reynolds number is the ratio of fluid inertia to viscosity near the surface of the droplet [59].

$$Re_{drop} = \frac{du_d}{\nu_c} \quad (77)$$

where, $d(m)$ is the droplet diameter, $u_d(m/s)$ is the droplet velocity, $\nu_c(Pa \cdot s)$ is the continuous phase kinematic viscosity.

$Re_{drop}(-)$ is also used to describe the behavior of the continuous phase flow around the droplet [59]. For example, a high droplet Reynolds number is characteristic of the occurrence of vortex shedding around droplet. This translates into an enhancement of turbulence [59]. As the Droplet Reynolds number $Re_{drop}(-)$ increases, the wake near the droplet becomes unstable and the vortex shedding start to appear at $Re_{drop}(-) \approx 270$ [60]. it is found that the turbulence is attenuated at low Droplet Reynolds number

$Re_{drop}(-) < 200$ and enhanced at high droplet Reynolds number $Re_{drop}(-) \geq 400$ [61].

2 Stokes number

The Stokes number $St(-)$ describes the behavior of droplets suspended in the continuous phase flow [59]. The Stokes number is the ratio of the dispersed phase droplets response time to continuous phase flow response time [59]:

$$St = \frac{\tau_d}{\tau_c} \quad (78)$$

where, the droplet response time $\tau_d(s)$ is the time necessary for a droplet velocity to increase from zero to 63% of surrounding oil flow velocity, $\tau_c(s)$ is the time scale of the continuous phase flow which travels the same distance as the droplet does [59]. When $St \leq 1$, the droplet follows the streamline of continuous phase flow around the droplet [59]. When $St > 1$, the droplet separates from the streamline of continuous phase flow. The Stock number is calculated as [59]:

$$St = \frac{1}{9} \frac{\rho_d}{\rho_c} Re_{drop} \quad (79)$$

where, $\rho_d(kg/m^3)$ is the density of dispersed water phase, $\rho_c(kg/m^3)$ is the density of continuous oil phase, and $Re_{drop}(-)$ is the droplet Reynolds number. It is found that turbulence is slightly attenuated or unchanged at low Stock number $St < 60$ [59]. The turbulent can be enhanced at high Stock number $St > 60$ [59].

3 Length scales

The length scale ratio is defined as the ratio of droplet diameter $d(m)$ to the characteristic length scale of the most energetic eddy $l_e(m)$ in the turbulent flow [59].

$$\text{Length scale ratio} = \frac{d}{l_e} \quad (80)$$

$$l_e = 0.1D \quad (81)$$

where, $D(m)$ is the pipe diameter. Studies found that turbulence is attenuated when $\frac{d}{l_e} < 0.1$ and that turbulence is enhanced when $\frac{d}{l_e} > 0.3$ [60]. When $0.1 < \frac{d}{l_e} < 0.3$, the turbulence can be either attenuated or enhanced [59].

4 Dispersed phase volume fraction

The dispersed phase volume fraction (water cut $\varepsilon(-)$) is an important parameter influencing the occurrence of turbulent modulation. This influence is defined based on the concept of droplet-flow interactions. The droplet-flow interactions are divided in to three parts: one-way coupling, two-way coupling, and four way coupling.

- One-way coupling is defined as a situation when droplets are moving at the same velocity and the same direction as surrounding flow. They are only affected by the surrounding flow and no turbulent modulation occurs [62].
- Two-way coupling represents a situation when droplets and surrounding flow can influence each other. In this case, turbulent modulation occurs [62].
- Four-way coupling is a combination of two-way coupling and drop-drop interaction (collision). In this case, turbulent modulation and droplet coalescence occur [62].

When $\varepsilon < 10^{-6}$, droplet motion is characterized as one-way coupling and no turbulent modulation [59]. When $10^{-6} < \varepsilon < 10^{-3}$, droplet motion is characterized as two-way coupling; the presence of droplets affect turbulence and turbulent modulation occur [59].

When $\varepsilon > 10^{-3}$, droplet motion is in four-way coupling and droplets coalescence and turbulent modulation occur [59].

The four parameters, droplet Reynolds number, Stokes number, length scale, and dispersed phase volume fraction, can be used to determine the extent of turbulent modulation. They can roughly determine whether turbulent modulation occurs or not. If turbulent modulation occurs, they can also determine whether the turbulence is enhanced or attenuated by the presence of dispersed droplets. In the conditions selected for this study, it was found that turbulent modulation should lead to a lower turbulent dissipation rate than calculated in Chapter 2.4. However, there is no comprehensive model which can accurately quantify and predict the modulation of water-in-oil dispersed flow at this moment [58].

Appendix II: Rosin-Rammler Parameters Data

This chapter discusses all the Rosin-Rammler equation parameters based on experiments performed in three configurations: standard pipe with valve, doughnut cell, and standard horizontal pipe, as shown in Table 7.

Table 7. Experimental Rosin-Rammler distribution parameters.

Standard pipe with valve Phase 1				
Experiment #	n	d* [μm]	Turbulent dissipation rate [Watt/kg]	Water cut [%]
2	1.95	116	202.7748	0.54
4	2.05	106	205.045	2.18
5	1.97	96	206.5625	2.54
6	1.99	96	206.1604	2.44
7	1.89	106	207.4614	3.84
9	1.93	97	208.7619	4.14
10	2.16	130	216.1679	8.35
11	2.12	117	220.3308	9.22
12	2.51	115	217.4471	8.62
13	1.9	162	230.7308	13.46
14	1.97	125	233.7731	14.02
15	2.2	121	242.8954	15.65
Standard pipe with valve Phase 2				
Experiment #	n	d* [μm]	Turbulent dissipation rate [Watt/kg]	Water cut [%]
2	2.46	88	121.9868	0.74
3	1.91	83	121.9534	0.79
5	2.17	103	122.3389	2.57
6	2.23	101	122.5275	2.82
7	2.36	120	122.4344	5.51
8	2.54	117	121.6853	4.76
9	2.44	114	121.3225	4.46
10	1.99	154	123.35	10.30
11	2.32	136	122.8719	10.08
12	2.24	131	121.2193	9.19
Standard pipe with valve Phase 3				
Experiment #	n	d* [μm]	Turbulent dissipation rate [Watt/kg]	Water cut [%]
3	2.66	141	164.8604	5.00

Table 7. (Continued)				
5	2.68	203	172.5971	10.50
8	3.02	101	377.6782	5.50
15	2.96	94	430.8588	5.00
Doughnut cell				
Experiment #	n	d* [μm]	Turbulent dissipation rate [Watt/kg]	Water cut [%]
1	2.39	273	1.009283	5.00
2	2.25	229	1.971255	5.00
3	2.15	189	3.719607	5.00
4	2.27	154	6.280011	5.00
5	1.93	323	2.10583	10.00
6	2.09	207	3.973539	10.00
7	2.16	166	6.708738	10.00
Standard horizontal pipe				
Experiment #	n	d* [μm]	Turbulent dissipation rate [Watt/kg]	Water cut [%]
1	3.27	3.96	0.314345	1.00
2	3.8	3.17	0.469267	1.00
3	3.78	2.55	0.666226	1.00
4	3.51	2.13	1.050144	1.00
5	2.97	2.98	0.682608	3.00
6	3.19	2.3	1.075965	3.00

Appendix III: Error Analysis

This chapter discusses broadly the error analysis on the measurements of droplet size, turbulent dissipation rate and water cut.

1 Error analysis on droplet size

The error analysis on the droplet size covers the repeatability of measured maximum droplet size, the uncertainty linked to the methodology of droplet size determination, and the error related to droplet sampling size.

1.1 Repeatability

The overall uncertainty on the measured maximum droplet size is evaluated at $\pm 30\%$, as shown in Figure 87. Here, each data point represents for the median droplet size determined through three repeat measurements. The error bar shows the upper and lower bounds obtained from the experimental runs. The variation in droplet size measurement can be related to the error linked to the measurement methodology and to the sampling size. This is discussed in following sections.

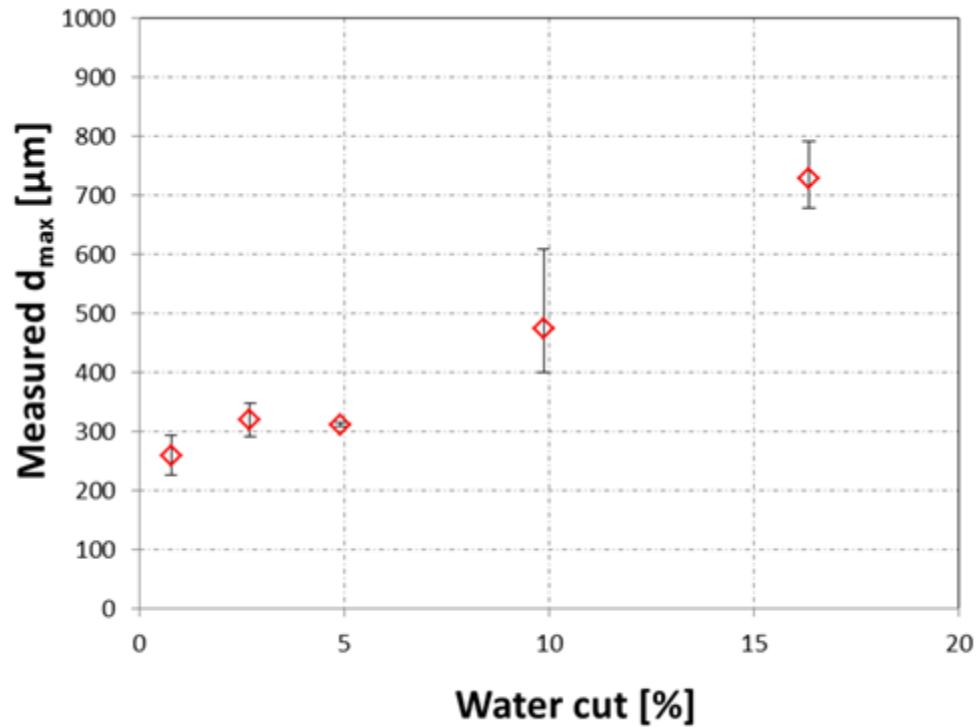


Figure 87. Measured maximum droplet size in relation to the water cut at 122 $Watt/kg$ average turbulent dissipation rate - Standard pipe with valve configuration.

1.2 Methodology of droplet size determination

Uncertainties exist due to the measurement methodology itself. The droplet size measurements hold an estimated $\pm 3\%$ error due to the thickness of the droplet edge. As shown in Figure 88 and Figure 89.

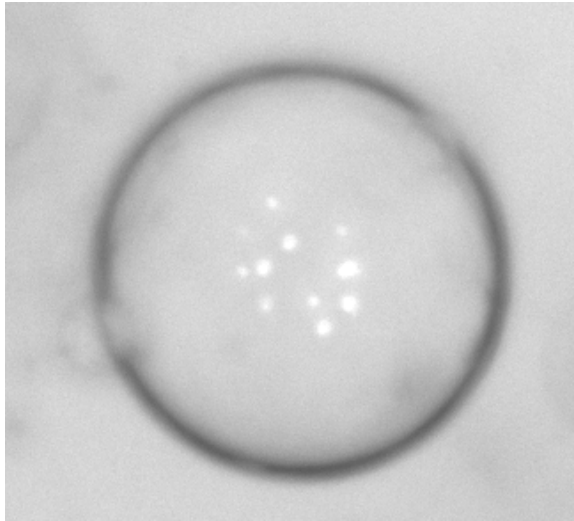


Figure 88. PVM droplet pictures



Figure 89. High speed camera droplet pictures

1.3 Droplet sampling size

The sampling size is the number of droplets measured in each experimental run. It is critical to ensure the sampling size is high enough to be representative of the whole

droplet population in the flow. The adequacy of the sampling size is evaluated by comparing the measured maximum droplet size $d_{max}(\mu m)$ and the Rosin-Rammler (R-R) predicted $d_{99,99}(\mu m)$, as shown in Table 8. If the sampling size is large enough, these two values should be close. Here, the $d_{max}(\mu m)$ is the largest droplet diameter out of 600 sampled droplets per experimental run in standard horizontal pipe configuration. The predicted $d_{99,99}(\mu m)$ is calculated using Rosin-Rammler equation and sampled droplet size from d_{10} to $d_{95}(\mu m)$. The $d_{99,99}(\mu m)$ can represent for the largest droplet size $d_{max}(\mu m)$ [8]. The result shows that the measured $d_{max}(\mu m)$ is always larger than predicted $d_{99,99}(\mu m)$ and proves that the sampling size is sufficient to capture the maximum droplet in the flow.

Table 8. Companion between measured and Rosin-Rammler predicted maximum droplet size-Standard horizontal pipe configuration.

Standard horizontal pipe					
Experiment #	Turbulent dissipation rate [Watt/kg]	Water cut [%]	Measured d_{max} [μm]	R-R predicted $d_{99,99}$ [μm]	%Error of R-R $d_{99,99}$ [%]
1	0.31	1	8650	7151	-17.3
2	0.47	1	5650	5271	-6.7
3	0.67	1	5110	4252	-16.8
4	1.05	1	4020	3694	-8.1
5	0.68	3	6380	5712	-10.5
6	1.08	3	4750	4215	-11.3

2 Error in turbulent dissipation rate and water cut

The turbulent dissipation rate and water cut are essential parameters for the droplet size predictions. The uncertainty related to the three experimental configurations is listed in Table 9. The reasoning behind these numbers is explained below.

Table 9. Measurement error of turbulent dissipation rate and water cut.

Experimental configuration	Error in turbulent dissipation rate [%]	Error in water cut [%]
Standard pipe with mixing valve	± 18.7	± 1.0
Doughnut cell	± 15.0	± 1.4
Standard pipe	± 15.0	± 7.1

2.1 Error in turbulent dissipation rate

The errors of turbulent dissipation rate are analyzed for three experimental configurations in this chapter.

2.1.1 Standard pipe with mixing valve

The calculation of turbulent dissipation rate in standard pipe with mixing valve configuration is shown as:

$$\bar{\epsilon} = f(\Delta P, \Delta L, U_c) = \frac{\Delta P U_c}{\Delta L} \quad (82)$$

here, the turbulent dissipation rate is calculated in terms of pressure drop, ΔP (pa) over a distance of ΔL (m) between the inlet and outlet of the valve. The error in continuous oil phase fluid velocity U_c (m/s), $E_{U_c}(-) = \pm 5.0\%$, is obtained from the error of oil pump's flow rate reading. The error in ΔP (Pa), $E_{\Delta P}(-) = \pm 10.0\%$, is based on the given measurement error of pressure gages. The calculation of distance, $\Delta L = \frac{V_{valve}}{A_{pipe}}$, uses the

valve volume $V_{valve}(m^3)$ and pipe cross section area $A_{pipe}(m^2)$. The error in $\Delta L(m)$, $E_{\Delta L}(-) = \pm 15.0\%$, is estimated based on the $\pm 15.0\%$ measurement uncertainty of the valve volume $V_{valve}(m^3)$.

The percent error propagation calculation is:

$$\begin{aligned} & \left(f(\Delta P, \Delta L, U_c) E_{\bar{e}_{valve}} \right)^2 \\ &= \left(\frac{\partial}{\partial \Delta P} f(\Delta P, \Delta L, U_c) \right)^2 (\Delta P E_{\Delta P})^2 \\ &+ \left(\frac{\partial}{\partial \Delta L} f(\Delta P, \Delta L, U_c) \right)^2 (\Delta L E_{\Delta L})^2 \\ &+ \left(\frac{\partial}{\partial U_c} f(\Delta P, \Delta L, U_c) \right)^2 (U_c E_{U_c})^2 \end{aligned} \quad (83)$$

The error of turbulent dissipation rate measurement is calculated: $E_{\bar{e}_{valve}} = \pm 18.7\%$

2.1.2 Doughnut cell

The turbulent dissipation rate calculation of doughnut cell configuration is shown as:

$$\bar{e} = f(\omega) = \frac{1}{12} \pi \rho_m f_t (R_o^3 - R_i^3) (R_o + R_i)^2 \omega^3 \quad (84)$$

where, $\omega(rad/s)$ is the top wall rotation speed, $R_o(m)$ is the outer diameter of the driving plate, $R_i(m)$ is the inner diameter of the driving plate, $V_c(m^3)$ is the volume of the continuous phase, $\rho_m(kg/m^3)$ is the density of the fluid mixture, and $\rho_c(kg/m^3)$ is the density of the continuous phase. The error in cell rotational speed $\omega(rad/s)$, $E_{\omega}(-) = \pm 5.0\%$, is the error of the driving motor .

The percent error propagation calculation is:

$$\left(f(\omega)E_{\bar{e}_{cell}}\right)^2 = \left(\frac{\partial}{\partial \omega}f(\omega)\right)^2 (\omega E_{\omega})^2 \quad (85)$$

The error of turbulent dissipation rate measurement is calculated: $E_{\bar{e}_{cell}} = \pm 15.0\%$

2.1.3 Standard pipe

The turbulent dissipation rate calculation of standard pipe configuration is shown as:

$$\bar{e} = f(U_c) = 2 \frac{f U_c^3 \rho_m}{D \rho_c} \quad (86)$$

here, the friction factor f in pipe flow is calculated with the Blasius equation: $f = \frac{0.046}{Re^{0.2}}$,

Re is the Reynolds number of the flow, $D(m)$ is the pipe internal diameter, $\rho_m(\text{kg}/\text{m}^3)$ is the water-in-oil mixture density, $\rho_c(\text{kg}/\text{m}^3)$ is the continuous phase (oil) density. The error in continuous phase fluid velocity $U_c(\text{m}/\text{s})$, $E_{U_c}(-) = \pm 5.0\%$, is obtained from the pump's flow rate error.

The percent error propagation calculation is:

$$\left(f(U_c)E_{\bar{e}_{pipe}}\right)^2 = \left(\frac{\partial}{\partial U_c}f(U_c)\right)^2 (U_c E_{U_c})^2 \quad (87)$$

The error of turbulent dissipation rate measurement is calculated: $E_{\bar{e}_{pipe}} = \pm 15.0$.

2.2 Error in water cut

2.2.1 Standard pipe with mixing valve

A Karl Fischer titration instrument is used to measure the water content of liquid samples from standard pipe with valve configuration. Error in water cut $\varepsilon(-)$, $E_{\varepsilon_{valve}}(-) = \pm 1.0\%$, is the given measurement error of Karl Fisher instrument [55].

2.2.2 Doughnut cell

The water cut calculation for doughnut cell configuration is:

$$\varepsilon = f(V_w, V_o) = \frac{V_w}{V_w + V_o} \quad (88)$$

The volumes of water $V_w(m^3)$ and oil $V_o(m^3)$ are measured prior to injection in the doughnut cell. The error in volume measurements of the graduated cylinder is given as:

$$E_{V_w} = E_{V_o} = \pm 1.0\%.$$

The percent error propagation calculation is:

$$\begin{aligned} & (f(V_w, V_o)E_{\varepsilon_{cell}})^2 \\ &= \left(\frac{\partial}{\partial V_w} f(V_w, V_o) \right)^2 (V_w E_{V_w})^2 \\ &+ \left(\frac{\partial}{\partial V_o} f(V_w, V_o) \right)^2 (V_o E_{V_o})^2 \end{aligned} \quad (89)$$

The error of water cut measurement is calculated: $E_{\varepsilon_{cell}}(-) = \pm 1.4\%$.

2.2.3 Standard pipe

The water cut calculation for standard pipe configuration is:

$$\varepsilon = f(U_d, U_c) = \frac{U_d}{U_d + U_c} \quad (90)$$

The error in continuous oil phase fluid velocity U_c (m/s), $E_{U_c}(-) = \pm 5.0\%$, is obtained from the error of oil pump flow rate. The error in dispersed water phase fluid velocity U_d (m/s), $E_{U_d}(-) = \pm 5.0\%$, is obtained from the error of water pump flow rate.

The percent error propagation calculation is:

$$\begin{aligned} & \left(f(U_d, U_c) E_{\varepsilon_{Pipe}} \right)^2 \\ &= \left(\frac{\partial}{\partial U_d} f(U_d, U_c) \right)^2 (U_d E_{U_d})^2 \\ &+ \left(\frac{\partial}{\partial U_c} f(U_d, U_c) \right)^2 (U_c E_{U_c})^2 \end{aligned} \quad (91)$$

The error of water cut measurement is calculated: $E_{\varepsilon_{Pipe}} = \pm 7.1\%$.

Appendix IV: Cumulative Frequency Droplet Size Distribution

In this chapter, the experimental results of droplet size distribution are shown as cumulative frequency distribution. The experimental results use the same droplet size data that are displayed for the cumulative volume distributions in Chapter 6.2.

1 Summary of results obtained in the standard pipe with mixing valve

The experimental results of droplet cumulative frequency distribution at different turbulent dissipation rates are plotted in Figure 90 for 5% water cut and Figure 91 for 10% water cut, respectively.

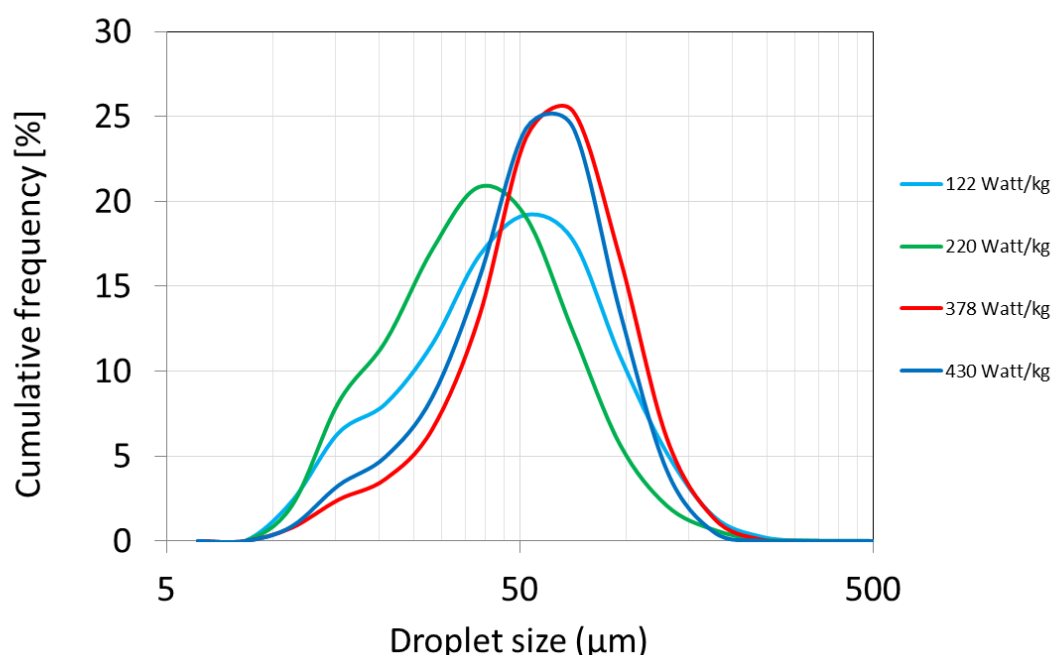


Figure 90. Effect of energy dissipation rate on the measured droplet size distribution at 5% average water cut – Standard horizontal pipe with mixing valve configuration.

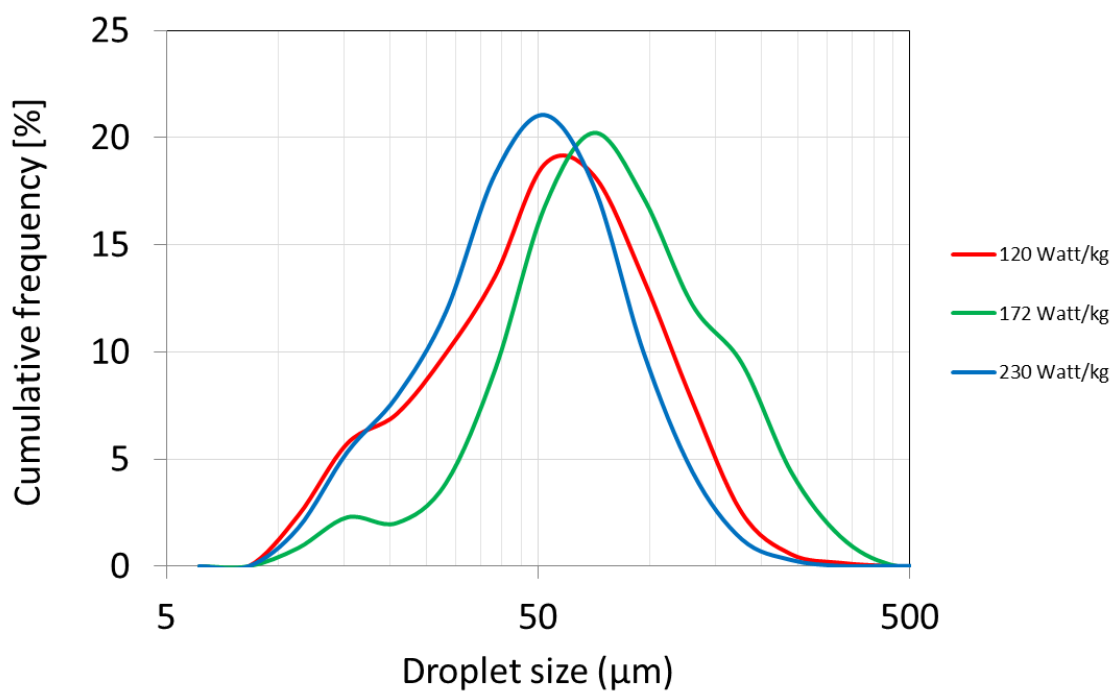


Figure 91. Effect of the energy dissipation rate on the measured droplet size distribution at 10% average water cut – Standard horizontal pipe with mixing valve configuration.

The next two graphs are plotted at different water cuts for turbulent dissipation rates of 122 *Watt/kg* (Figure 92) and for 220 *Watt/kg* (Figure 93) respectively.

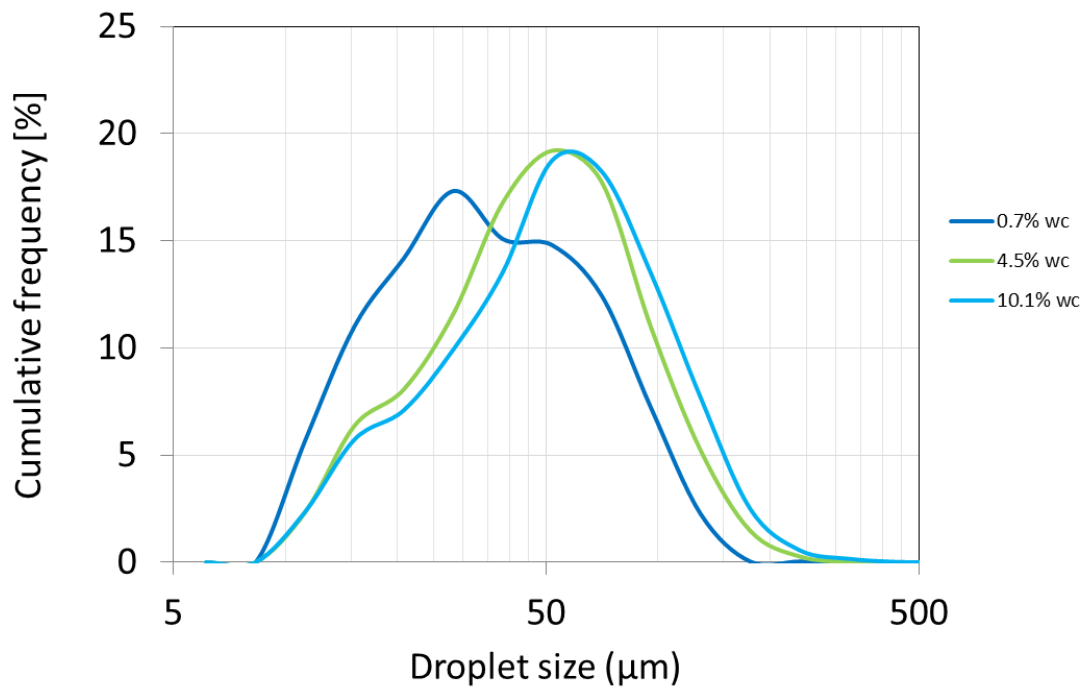


Figure 92. Effect of the water cut on the measured droplet size distribution at 122 Watt/kg turbulent dissipation rate – Standard horizontal pipe with mixing valve configuration.

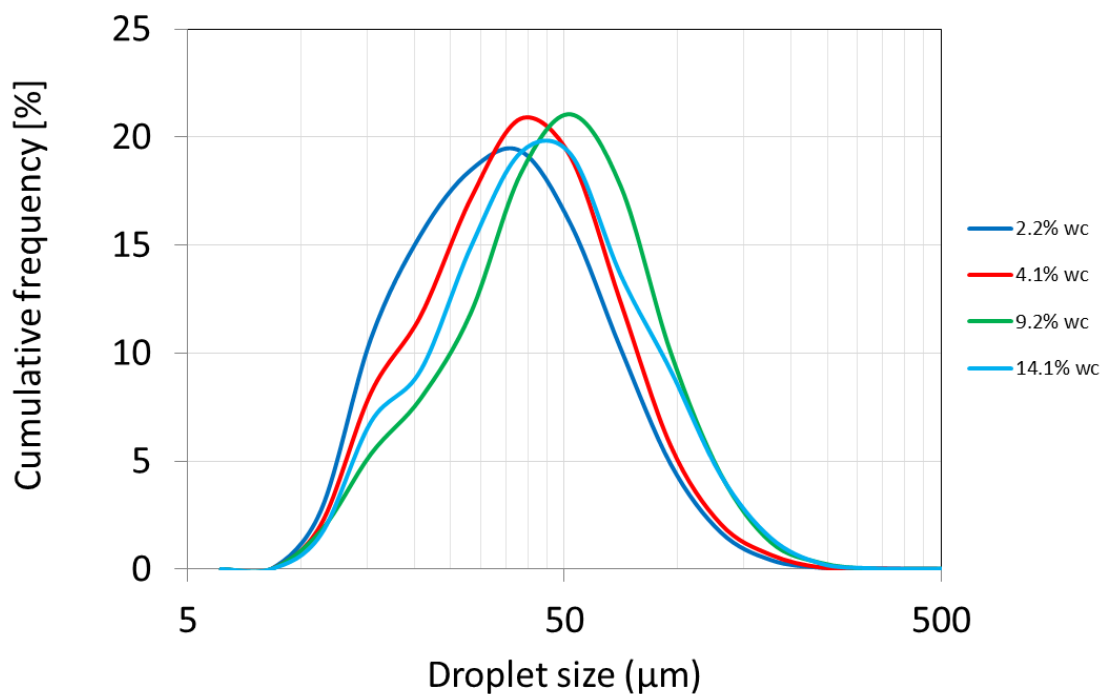


Figure 93. Effect of the water cut on the measured droplet size distribution at 220 *Watt/kg* turbulent dissipation rate – Standard horizontal pipe with mixing valve configuration.

2 Summary of results obtained with the Doughnut cell

Similarly to the previous section, the experimental cumulative frequency distributions obtained in the doughnut cell are plotted. The effect of turbulent dissipation rate is shown in Figure 94, for 5% water cut, and Figure 95, for 10% water cut, while the effect of water cut is shown in Figure 96, for 2 *Watt/kg*, and Figure 97, for 6 *Watt/kg* turbulent dissipation rate.

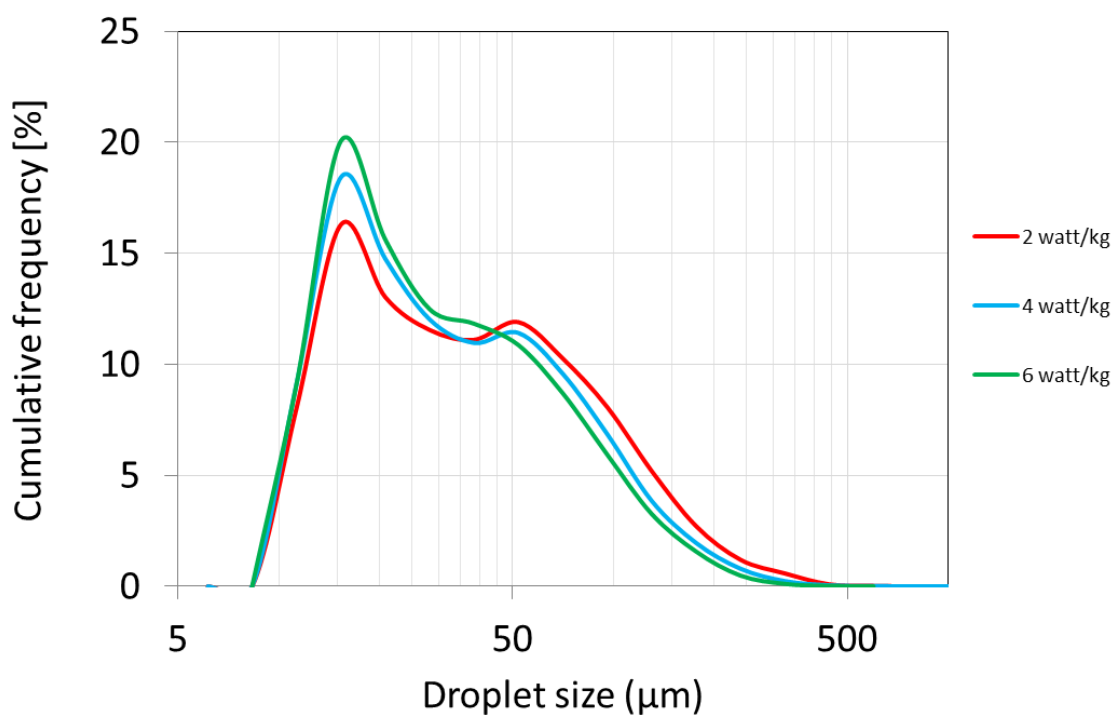


Figure 94. Effect of energy dissipation rate on the measured droplet size distribution at 5% average water cut – Doughnut cell configuration.

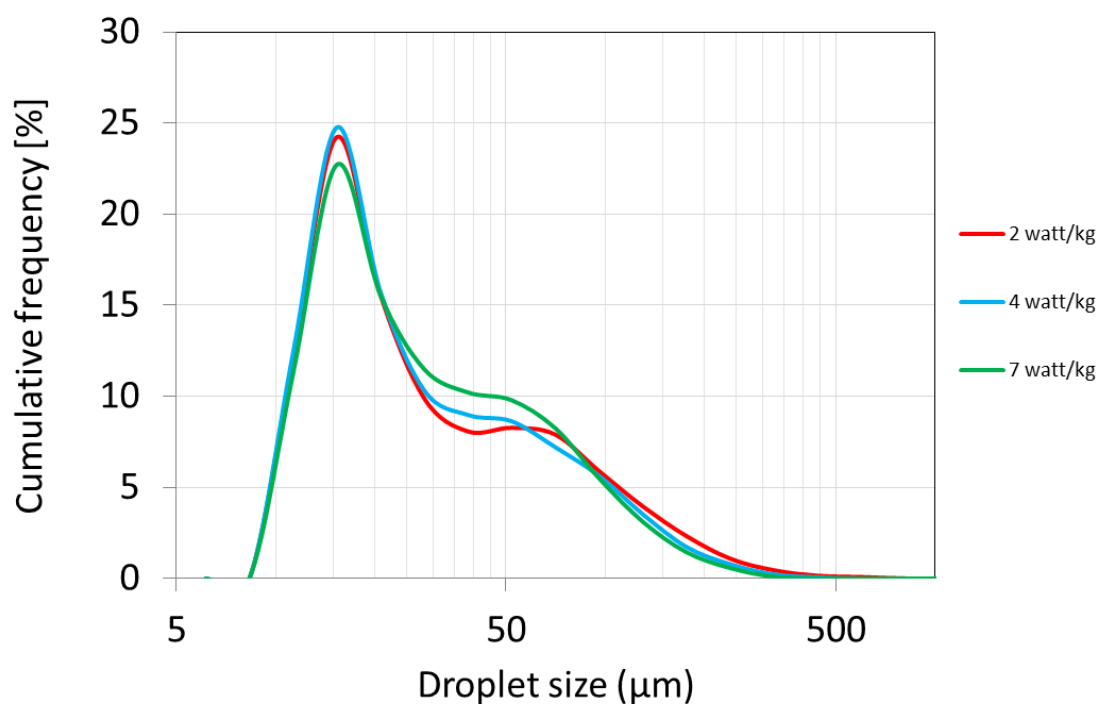


Figure 95. Effect of the energy dissipation rate on the measured droplet size distribution at 10% average water cut – Doughnut cell configuration.

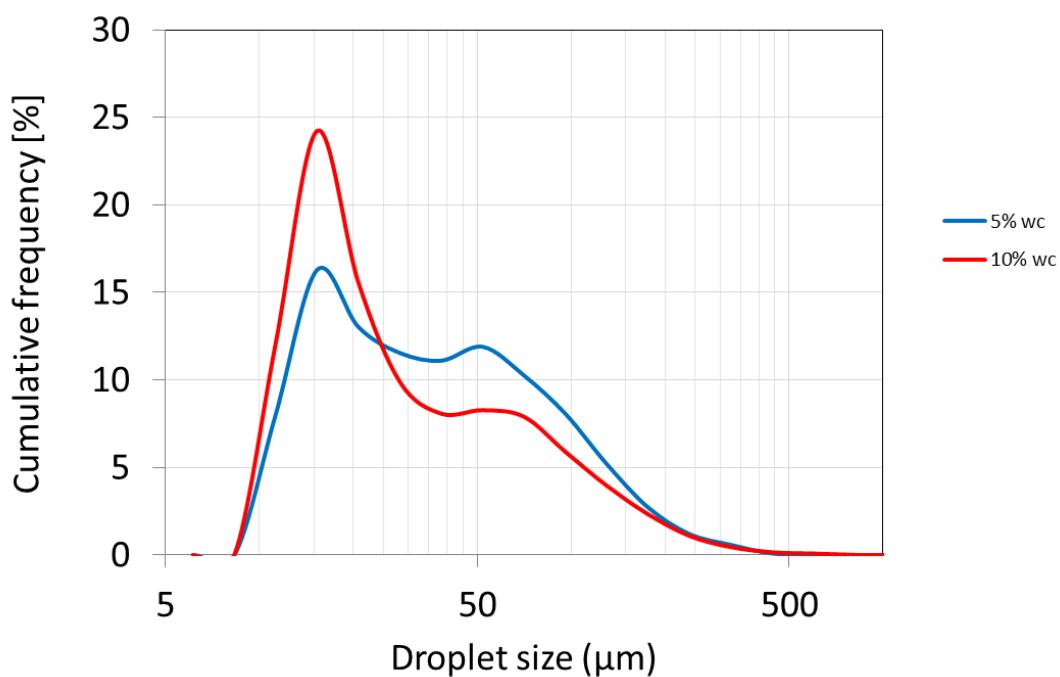


Figure 96. Effect of the water cut on the measured droplet size distribution at 2 *Watt/kg* turbulent dissipation rate – Doughnut cell configuration.

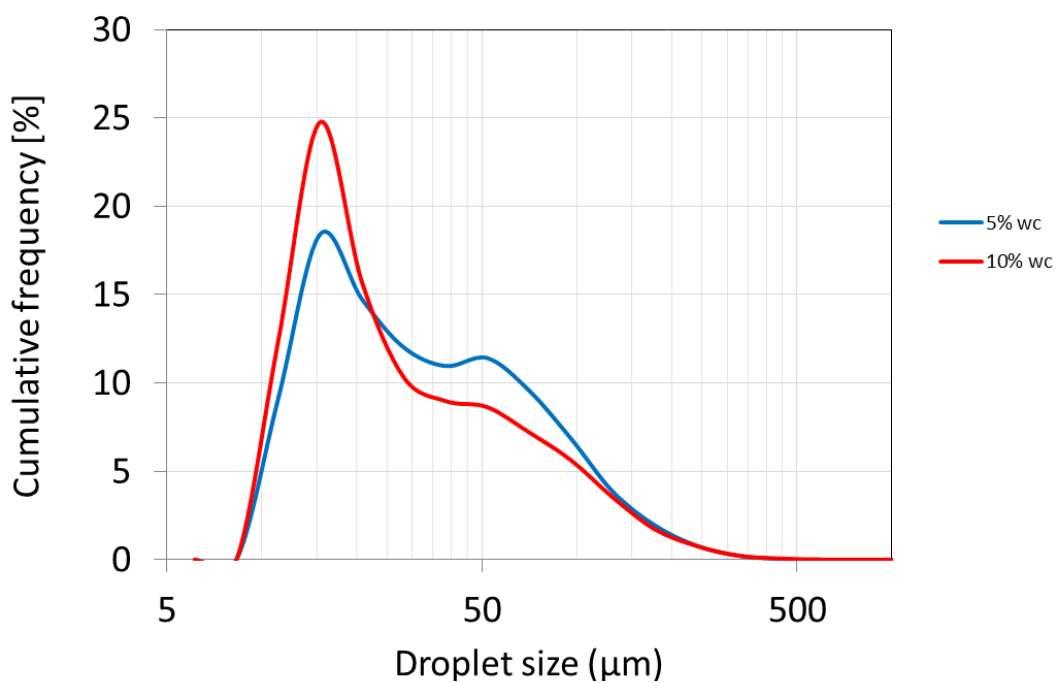


Figure 97. Effect of the water cut on the measured droplet size distribution at 6 *Watt/kg* turbulent dissipation rate – Doughnut cell configuration.

3 Summary of results obtained with the standard pipe experiments

Finally, the presentation of the experimental results is repeated for the standard pipe flow configuration. The effect of turbulent dissipation rate is shown in Figure 98, for 1% water cut, while the effect of water cut is shown in Figure 99 for 0.6 *Watt/kg* and Figure 100 for 1.1 *Watt/kg*.

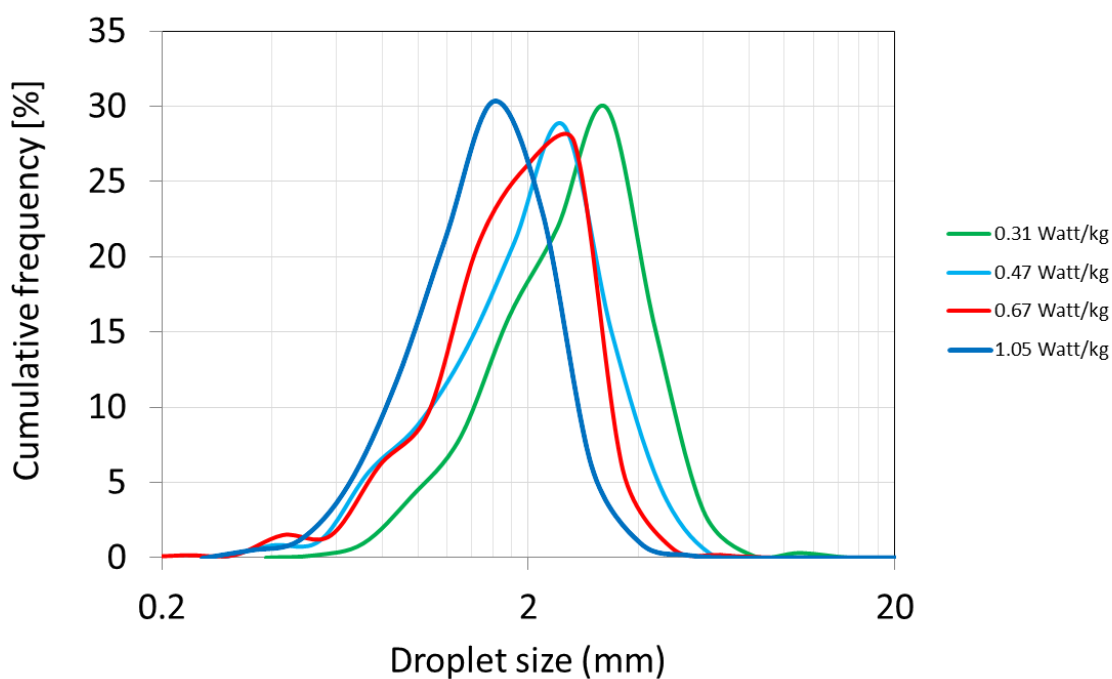


Figure 98. Effect of energy dissipation rate on the measured droplet size distribution at 1% average water cut – Horizontal standard pipe flow configuration.

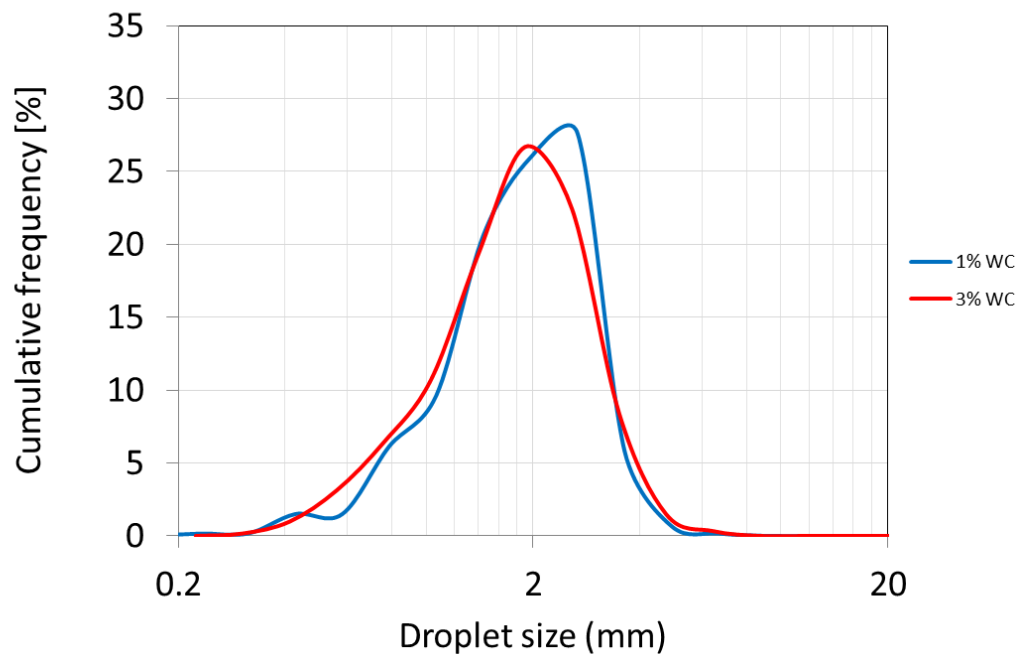


Figure 99. Effect of the water cut on the measured droplet size distribution at 0.6 $Watt/kg$ turbulent dissipation rate - Horizontal standard pipe flow configuration.

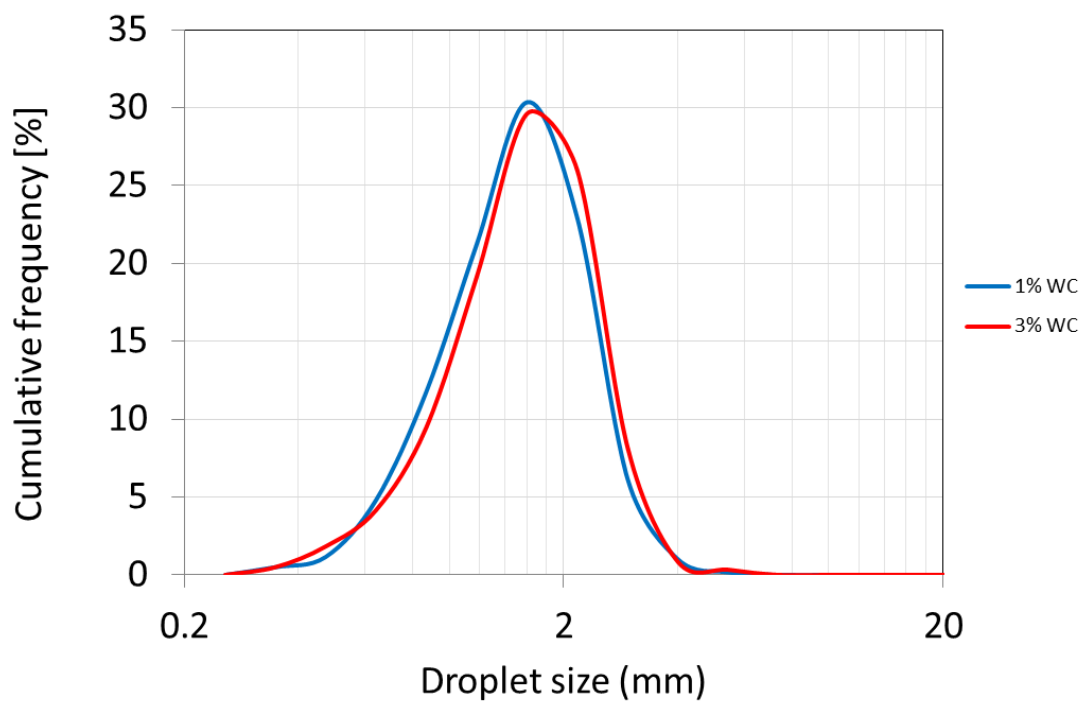


Figure 100. Effect of the water cut on the measured droplet size at 1.1 $Watt/kg$ turbulent dissipation rate - Horizontal standard pipe flow.